Exceptional Preservation and Bias in the Fossil Record

Andrew Donald Hawkins

Dissertation submitted to the faculty of the Virginia Polytechnic Institute and State University in partial fulfillment of the requirements for the degree of

Doctor of Philosophy

In

Geosciences

Shuhai Xiao, Committee Chair

Benjamin Gill

Brian Romans

Michal Kowalewski

September 21st 2017

Blacksburg, Va

Keywords: Doushantuo Formation, Winneshiek, Lagerstätte, lithification bias

UMI Page

Exceptional Preservation and Bias in the Fossil Record

Andrew D. Hawkins

ABSTRACT

The three projects described herein focus on two instances of exceptional preservation and on potential source of bias in the fossil record. The occurrence of exceptionally preserved fossil assemblages and the existence of systematic bias in the fossil record from a variety of sources represent opposing forces acting on the information quality of the fossil record. Exceptionally preserved assemblages capture features of anatomy and components of assemblages not normally recorded in the fossil record. Systematic biases affecting the fossil record do the opposite, skewing our perception of patterns of diversity, the relative dominance of clades and changes in ecosystems through time. Chapter one presents the results of an analog modeling analysis to assess whether and how a newly proposed potential mechanism, the preferential sampling of larger specimens during fossil sampling due to the greater likelihood of larger specimens being intersected by a fracture surface, contributes to the lithification bias. Chapters two and three focus on the exceptionally preserved vermiform fossils from the Winneshiek Lagerstätte in northeastern Iowa and microfossils from the Doushantuo Formation of South China, respectively. Chapter two aims at resolving the identity of the Winneshiek vermiform fossils and presents evidence that these structures represent phosphatized bromalites, an ichnologic category that includes coprolites and cololites. Chapter three presents a biostratigraphy study of exceptionally preserved microfossils at three sections of the Doushantuo Formation in South China. Acanthomorphic acritarchs represent

a promising tool for subdivision and correlation of the Doushantuo Formation of South China and Ediacaran strata around the world. However, the occurrence of acanthomorphic acritarchs within the Doushantuo Formation is controlled by the availability of early diagenetic chert nodules that host microfossils such as acanthomorphic acritarchs. One of these sections contains the rare occurrence of early diagenetic cherts in an upper slope section. This new biostratigraphic data adds to the growing body of integrated chemostratigraphic and biostratigraphic data from the Doushantuo Formation. By understanding both exceptional preservation and sources of bias in the fossil record it is possible to separate artifact and noise from the true signal of the history of life.

For my parents, Andy & Marilee Hawkins

Funding Sources

The following sources provided funding supporting the projects presented herein:

National Science Foundation

EAR-1528553

EAR-0921245

EAR-0922054

NASA Exobiology and Evolutionary Biology Program

NNX15AL27G

The Paleontological Society

The Virginia Tech Department of Geosciences.

Acknowledgements

Co-authors of the following chapters provided invaluable assistance in research design, sample collection and processing, data interpretation and revising manuscript drafts. Their contribution is gratefully acknowledged.

Chapter 2: Andrew Donald Hawkins [1], Michal Kowalewski [2], Shuhai Xiao [1]

Chapter 3: Andrew Donald Hawkins [1], Huaibao P. Liu 3, Derek E. G. Briggs 4, Drew Muscente1 Robert M. McKay 3, Brian J. Witzke 5, Shuhai Xiao 1

Chapter 4: Andrew Donald Hawkins [1], Shuhai Xiao [1,*], Ganqing Jiang [6], Xinqiang Wang [7,8], Xiaoying Shi [7,8]

[1]Department of Geosciences, Virginia Tech, Blacksburg, VA 24061, USA, andrewdh@vt.edu and xiao@vt.edu; [3]Iowa Geological Survey, IIHR-Hydroscience & Engineering, University of Iowa, Iowa City, IA 52242, USA; [4]Department of Geology and Geophysics, Yale University, New Haven, CT 06520, USA; [5]Department of Earth and Environmental Sciences, University of Iowa, Iowa City, IA 52242, USA; [6] Department of Geosciences, University of Nevada, Las Vegas, Nevada 89154, USA; [7] State Key Laboratory of Biogeology and Environmental Geology, Beijing 100083, China; [8] School of Earth Science and Resources, China University of Geosciences (Beijing), Beijing 100083, China

There are many people without whom this dissertation would not have been completed. My advisor Dr. Shuhai Xiao shared his vast knowledge on a myriad of topics related to different aspects of this research over the course of these projects and was even more generous with his patience, and I am exceedingly grateful for both. My committee members Benjamin Gill, Brian Romans and Michal Kowalewski provided useful discussions, comments and critiques

throughout this process, and I express my thanks to them as well. I also owe many thanks to my fellow members past and present of the Virginia Tech Paleobiology Group: Mike Meyer, Jessie Brocce, Jackie Wittmer, Sahale Casebolt, Drew Muscente, Natasha Bykova, Qing Tang, Caitlin Colleary and Chris Griffin provided comradery, excellent discussions and emotional support over the years. Thank you all. Finally, Matthew LeRoy, in addition to being a great friend, kindly let me be an unexpected roommate during the final months in which this dissertation was being completed. Thanks man.

Table of Contents

List of Figures

List of Tables

Chapter 1 Introduction

Introduction

Two sets of processes exert an influence on the quality and fidelity of the fossil record: processes that premote exceptional preservation and those that produce systematic biases. Exceptional preservation can occur through a variety of pathways including the precipitation and growth of minerals such as pyrite or francolite on tissues, resulting in the preservation of soft tissues and morphological information in the form of carbon films. Processes of exceptional preservation conserve morphological and paleoecological information that would normally be lost in the fossil record. As a result exceptionally preserved faunas have contributed substantially to our knowledge of ancient communities. In contrast, systematic biases capable of skewing or obscuring the patterns of diversity, relative abundance and presence or absence of different taxa also affect the fossil record. Such biases can stem from a variety of sources related to taphonomy to methodology. In this dissertation I investigate two instances of exceptional preservation, vermiform structures from the Winneshiek Lagerstätte and silicified microfossils from the Ediacaran Doushantuo Formation of South China, and how fossil collection methods may contribute to the lithification bias, a recently recognized bias that may affect estimates of within-community diversity through much of the Phanerozoic.

Research Goals

Chapter 1 focuses on the problem of whether fossil sampling by means of splitting rock, a common collection method for well-lithified sediments, can potentially induce a size selective bias that skews estimates of sample diversity and average specimen size. This potential bias, dubbed preferential intersection, is a possible contributing factor to the lithification bias, a recently

recognized phenomena of decreased diversity in fossil samples collected from lithified sediments as compared with samples that derive from unlithified sediments. The lithification bias has been demonstrated empirically in Cenozoic molluscan assemblages. However the processes responsible for this bias are still poorly understood. Understanding the underlying causes of this bias is important as it has been suggested to act as a megabias due to the variation in lithification found in the Phanerozoic sedimentary rock record. The goals of this work are three-fold. The first was to test the hypothesis that preferential intersection can bias estimates of diversity and average specimen size independent of other potential biases such as preferential dissolution of aragonitic specimens or breakage of small specimens during sampling. The second was to understand how varying the species abundance distribution and the species size distribution in a sample impacts the magnitude of the bias induced by preferential intersection. The third goal was to determine whether the potential biasing effects of preferential intersection are sufficient to fully explain the empirically observed lithification bias or whether other biases need to be invoked. This chapter has been submitted for publication to the journal Paleobiology.

Chapter 2 presents a taphonomic study of enigmatic three-dimensionally preserved structures from the Middle Ordovician Winneshiek Lagerstätte in northeastern Iowa. These structures, which have been dubbed vermiform fossils, are preserved in three dimensions via phosphatization. This style of preservation contrasts markedly with other types of exceptional preservation found in the Winneshiek Lagerstätte as the fauna primarily consists of arthropods preserved as carbonaceous compressions. Winneshiek vermiform fossils have previously been interpreted as bromalites, a group of trace fossils that include coprolites and cololites(internal molds of digestive organs). However, there has been no systematic investigation of the vermiform fossils to test the bromalite interpretation. The research goals of this project were to characterize

the chemical composition, external and internal morphologies and microstructure of the Winneshiek vermiform fossils, to construct a paragenetic sequence responsible for the phosphatization of the Winneshiek vermiform fossils and to evaluate hypothesized vermiform tracemakers. This chapter has been accepted for publication with revision by the journal Paliaos.

Chapter 3 focusses on documenting exceptionally preserved microfossils, including biostratigraphically useful acanthomorphic acritarchs, at three sections of the Ediacaran Doushantuo Formation in South China. These sections, located at Wangzishi, Huangjiaping and Siduping in Hubei and Hunan provinces, are outside the Yangtze Gorges area where extensive research on the Doushantuo Formation has been carried out. Two of the sections, the Wangzishi and Huangjiaping sections, were deposited within the intrashelf lagoon while the third, the Siduping section, was deposited in an upper slope setting. The exceptional microfossil record preserved in the Doushantuo Formation in the Yangtze Gorges area is due to the formation of early diagenetic cherts. While these early diagenetic cherts are absent from most sections outside the Yangtze Gorges area, their presence at the three studied sections provides an opportunity to extend the paleogeographic range of the Doushantuo Formation microfossil record. The research goals were to document the biostratigraphic and paleogeographic ranges of microfossils in the Ediacaran Doushantuo Formation. This chapter has been published in the journal Precambrian Research.

Research Methodology

Chapter 1: Lithification Bias

To test whether preferential intersection can impose a bias on estimates of species richness, assemblage evenness, and average specimen size, independent of other potential sources of bias, we used a simple analog model of fossil collection from lithified sediments. This model was implemented in MATLAB and consists of three parts: 1) A cubic volume analogous to a bulk

sample of fossiliferous rock that can be populated with specimens, 2) one or more horizontal planes within the cubic volume which are analogous to fracture planes, and 3) specimens within the volume. The model replicates fossil sampling by generating a cubic volume populated by specimens and then selecting horizontal planes at random vertical positions within the cubic volume. The model then counts all specimens within the volume which intersect at least one of the planes. The model repeats the process of populated volume generation and sampling until it the total number of counted specimens reaches a user defined quota.

In order to gauge whether preferential intersection biases estimates of diversity and size we compared mean values and 95% confidence intervals of species richness, evenness and average specimen size produced by the preferential intersection model with those produced by a random draw model. This random draw model simulated sample collection via sieving unconsolidated sediment. We also tested whether preferential intersection imposes a bias by performing t-tests on sets of species richness, assemblage evenness and average specimen size values generated by the preferential and random draw models. Comparisons between the results of the two models were performed for nine combinations of species abundance and species size distributions.

Chapter 2: Vermiform Fossils from the Middle Ordovician Winneshiek Lagerstätte

In order to document morphological and compositional features of Winneshiek bromalite fossils , the internal and surficial structures and microstructures of a morphologically diverse suite of vermiform fossils were examined using a combination of transmitted light, reflected light, and electron microscopy. Thirteen specimens were subjected to destructive analysis. All 13 were thick sectioned and 5 of them were also thin sectioned. Thin sections were examined using a BX51 light microscope. Compositional data and elemental maps were obtained from polished thick and thin

sections using a Hitachi TM3000 table top SEM with a bruker XFlash EDS system and a FEI Quanta 600F low vacuum environmental SEM.

Chapter 3: New Microfossils from the Ediacaran aged Doushantuo Formation of South China.

Chert samples were collected from three sections of the Ediacaran aged Doushantuo Formation. The samples were thin sectioned and examined using transmitted light microscopy for microfossils, particularly biostratigraphically important acanthomorphic acritarchs. Petrographic observations were made to determine whether fossiliferous cherts were formed in situ or transported from elsewhere. Biostratigraphic data from the upper slope Siduping section was integrated with the $\delta^{13}C_{carb}$ record in order to refine correlation with better studied sections in the Yangtze Gorges area. The integrated biostratigraphic and chemostratigraphic data were used to determine the stratigraphic and paleogeographic range of Ediacaran acanthomorphic acritarchs.

Chapter 2 The Lithification Bias, an analogue modeling approach

Abstract

Lithification, the process where unconsolidated sediments transition to fully indurated rocks, can potentially bias the species richness, evenness, and body size distribution of fossil assemblages. Specifically, fossil collections made from well-indurated rocks consistently exhibit lower species richness and evenness, and a specimen size distribution skewed towards larger specimens relative to collections made from unconsolidated sediments. While the bias itself has been demonstrated empirically, much less attention has been paid to the question of its cause. Proposed mechanisms include destruction of small specimens during early diagenesis and specimen destruction associated with mechanically breaking rock during

sampling. Here we investigate the potential effects of an alternative mechanism that could also result in a methodology related bias: the preferential intersection of larger specimens relative to smaller ones during bulk fossil sampling. We present the results of an analog modeling study of fossil collection via splitting fossiliferous rock and compare the results to a random draw model that approximates the effects of sieving. Based on the results we analyze how differences in fossil sampling methodology between well-indurated rocks and unconsolidated sediments can impart bias. Our results demonstrate that for at least some collections preferential intersection can impose a significant bias independent of other mechanisms, although it cannot fully duplicate the observed bias on its own.

Introduction

Multiple studies have demonstrated that bulk fossil collections made from well-indurated sedimentary rock are not interchangeable with their counterparts from unlithified sediments. Fossil samples from fully-lithified sediments are less species rich and exhibit lower measures of evenness compared with samples made from unlithified sediments (Hendy 2009; Sanders et al. 2015; Sessa et al. 2009). These samples also exhibit distinct specimen size distributions that are skewed towards larger specimen sizes. This size bias is thought to drive the effects on richness and evenness due to the underrepresentation or absence of smaller species. These differences are not a product of easier specimen collection in unconsolidated sediments because they remain even after correcting for differences in sample size (Hendy 2009; Sessa et al. 2009). This effect of lithification on sampled diversity has been termed the *lithification bias* and is sufficiently large that Hendy (2011) argued that it represents a megabias with the potential to effect the apparent trajectory of sample level diversity through the Phanerozoic. Kowalewski et al. (2006) reached a similar conclusion in their analysis of potential sources of bias that could contribute to the apparent post-

Paleozoic increase in sample level diversity. Concerns over the potential for lithification to bias measures of diversity were significant enough that Alroy et al. (2008) excluded collections from unlithified sediments in their sampling standardized analysis of Phanerozoic diversity.

While much attention has been paid to the question of *whether* lithification state biases measures of diversity, much less has been paid to the question of what mechanism or mechanisms are responsible for this effect. Even less effort has been focused on trying to isolate and test individual mechanisms [though see Nawrot (2012), Daley and Bush (2012), and Daley and Bush (2014) for important exceptions]. Most discussions of the lithification bias have attributed the bias to the dissolution of small aragonitic specimens during early diagenesis (Hendy 2009; Sanders et al. 2015). For example, Hendy (2009) suggested that changes in pH during quartz cementation of sandstones and siltstones resulted in the selective dissolution of small aragonitic specimens. This is a plausible explanation because shell size and mineralogy are two of the most important factors in determining the vulnerability of a shell to dissolution during early diagenesis (Martin 1999). However, well-indurated sediments differ from unlithified sediments in other ways besides their diagenetic history, and these may also impart a bias on the preserved diversity. In particular, fossil collection methodologies differ significantly between lithified and unlithified sediments. Unlithified sediments can be sieved, which allows for retrieving all specimens larger than the mesh size from a volume of sediment (Kowalewski and Hoffmeister 2003). In contrast, fossil collection from lithified sediments is made by either scanning naturally exposed surfaces or else mechanically breaking up bulk rock samples and scanning the surfaces of broken pieces. Kowalewski et al. (2006) recognized the methodological issues related to fossil sampling from fully lithified sediments when they suggested that bias related to lithification may be due to the breakage and destruction of small specimens when fracturing lithified rocks. Even without the

outright destruction of small specimens, sample collection from well-lithified sediments has the potential to result in a size related bias. This is because the specimens that can be recognized and recorded, and that therefore contribute to the sample, are limited to only those specimens that intersect the top or bottom of the bed or the mechanically generated fracture surface(s). Given that larger specimens are more likely than smaller specimens to intersect a fracture surface or the top or bottom of a bed, it is conceivable that this could also lead to size-related bias. This phenomena has previously been recognized in contexts ranging from paleobiology to igneous petrology but has not been previously considered as a potential mechanism for the lithification bias (McKinney 1986; Peterson 1996). We term this alternative mechanism *preferential intersection.*

Here we use a simple analog model of fossil collection from lithified sediments to test the hypothesis that preferential intersection can bias assemblage richness, evenness, and average specimen size. The model is implemented in Matlab, which allows us to isolate different factors that may contribute to the observed lithification bias and assess their individual contributions to the overall bias. We use this model to examine how the species abundance and the species size distributions contribute to the degree of bias a fossil collection exhibits and then compare this to the magnitude of the empirically observed bias. By determining how much bias can be generated, independent of any loss of aragonitic specimens, we place constraints on the degree of species loss due to aragonite dissolution, or other mechanisms, which must be invoked in order to explain the empirically demonstrated lithification bias. Finally, we consider factors that the model does not address and how these may also contribute to the lithification bias.

Background

The first suggestion that lithification state might exert an effect on sample level diversity came from the work of Kowalewski et al. (2006). These authors examined two questions related

to the post-Paleozoic increase in sample level diversity: What was its magnitude and was it an artifact, either partially or entirely, of one or more of a suite of potential biases. To do this they used a large collection of bulk samples that allowed them to standardize samples for collecting procedure (i.e., sieve size) and sample size. Since the suite of collections they examined were collected by a small number of workers, they were also able to avoid complications due to differences in taxonomic practices. The potential biases they considered included variation in the paleolatitude and paleoenvironmental setting of the collection sites, sample lithology, the loss of specimens due to dissolution of aragonitic shells, and preservation quality (i.e., moldic versus shell preservation). By examining subsets of their data that were not affected by certain factors, such as sets of samples that were collected from the same paleolatitudinal range or were uniformly dominated by aragonitic taxa, they were able to determine whether the magnitude of the diversity increase was significantly altered by other factors. Based on their analyses, Kowalewski et al. (2006) were able to reject biases related to latitude, lithology, paleoenvironment, preservational quality (i.e., mold/cast vs. carbonate shell material), and aragonite dissolution as being important factors in the observed increase in sample level diversity. Importantly, Kowalewski et al. (2006) were not able to reject the possibility that lithification state might be a confounding factor, and they noted that the transition in the sedimentary record from being predominantly fully lithified units to a mixture of lithified, poorly lithified, and unlithified units occurred over the same interval as the observed increase in diversity.

Sessa et al. (2009) and Hendy (2009) more explicitly tested the hypothesis that lithification state could exert an influence on the diversity of bulk samples by comparing samples from the same time interval that contained the same fossil assemblages but represented a range of lithification states. In two different settings, the lower Cenozoic of the Gulf Coast of the southern

United States and two Cenozoic basins in New Zealand, Sessa et al. (2009) and Hendy (2009) each compared the species richness, evenness, and average size of specimens of collections made from locally lithified and unlithified units. Both Sessa et al. (2009) and Hendy (2009) found that samples from fully lithified sediments exhibited lower species richness, were less even, and exhibited different specimen size distributions than samples from unlithified sediments. Intriguingly, Hendy (2009) found that poorly lithified sediments, which were less lithified than their fully lithified category but could not be fully disaggregated, exhibited virtually no difference in terms of diversity as compared to their unlithified counterparts. Both Sessa et al. (2009) and Hendy (2009) also examined the impact of lithification on the diversity patterns observed in their respective study systems at larger scales. Sessa et al. (2009) found that lithification state altered the apparent diversity dynamics of the recovery following the KT extinction event and Hendy (2009) observed that an overall increase in diversity corresponded to a change in lithification state over time.

Sessa et al. (2009) did not suggest a mechanism to explain their results but Hendy (2009) suggested that the diversity difference observed in their samples likely reflected the loss of small specimens with aragonitic mineralogies. This mechanism has been the most frequently invoked explanation for the impact of lithification state on sample level diversity (Sanders et al. 2015). The dissolution of specimens with aragonitic shell mineralogies during early diagenesis is a widely recognized taphonomic phenomenon driven by the fact that aragonite is less thermodynamically stable at Earth surface conditions compared to both low magnesium and high magnesium calcite. However, the question of just how much bias aragonite dissolution introduces to the record of sample-level diversity is unclear, and this question has provoked significant discussion in the paleobiological literature in its own right, independent of its relevance to understanding the biasing effects of lithification state (Bush and Bambach 2004; Cherns and Wright 2000, 2009; Foote et al.

2015; Kidwell 2005). While a significant role for aragonite dissolution appears obvious in some studies of lithification bias (i.e., Sanders et al. 2015), there are likely to be other contributing factors to the lithification bias stemming from methodological issues, and these must be evaluated and taken into account before a strategy for correcting for the effects of lithification state can be developed. Kowalewski et al. (2006) suggested that specimens smaller than 5 mm are often broken during splitting of well-indurated rock and that this methodological issue likely contributes to biasing effects of lithification.

The additional methodological issue investigated here, which we term preferential intersection, has previously been discussed under various names with related issues in both paleobiological and non-paleobiological contexts. McKinney (1986) examined the question of estimating the volumetric abundance of fossils in cross sections of fossiliferous rock. They demonstrated that, assuming specimens are both randomly distributed and randomly oriented within the matrix, the average number of specimens seen in cross section can be used to estimate the average number of specimens within a unit volume. Intersection poses a significant problem for estimating the size distribution of particles based on stereological cross sections, because particles in a volume are rarely intersected through their center, which can skew the apparent size distribution of intersected particles (Peterson 1996).

Several authors have previously attempted to investigate whether lithification can induce a bias independent of the effects aragonite dissolution. Nawrot (2012) compared the diversity found in beach rock cemented early in diagenesis to that of paleoecologically similar collections in unlithified sediments. The aim of Nawrot (2012)'s approach was to investigate whether bias existed in a system where cementation occurred sufficiently early so as to prevent significant loss of specimens due to aragonite dissolution. In contrast to other studies of the lithification bias,

Nawrot (2012) reported no discernable difference between his lithified and unlithified samples. This result can be explained by noting that Nawrot (2012) described their lithified samples as being more similar to Hendy (2009)'s poorly lithified category than his fully lithified category, and being susceptible to significant though not complete disaggregation. With this finding in mind, the results of Nawrot (2012) are not necessarily unexpected and thus do not negate the possibility of non-aragonite related mechanisms contributing to the lithification bias.

Daley and Bush (2012) and Daley and Bush (2014) used Portland cement to artificially generate highly fossiliferous "rocks", which were then sampled to evaluate non-aragonite related biasing mechanisms. Interestingly, Daley and Bush (2014) found that while in some trials a bias was generated, other samples were more diverse and more even than would be expected from random draws from the assemblage of shells which she used to populate the artificial rocks. Neither Daley and Bush (2012) nor Daley and Bush (2014) proposed a potential mechanism for their observed effect.

Methods

To explore the impact of preferential intersection on paleobiological sampling, we developed a simple model that captures the basic aspects of fossil sampling from lithified rock. Here we discuss the basic parts of the model and how it was used to investigate the biasing effects of preferential intersection. A more detailed description of the model is provided in Appendix II. The model in its simplest form consists of three parts: A cubic volume to be populated with specimens, one or more fracture planes, and the specimens themselves. Each of these were represented in MATLAB as sets of coordinates. Sets of coordinates for the more geometrically complex specimens were generated using Raup (1979)'s coiling model. The populated volume is analogous to a fossiliferous rock and is sampled by being bisected by one or more horizontal

planes, analogous to planar fractures, at random points along its vertical axis. Specimens that intersect one or more planes were considered exposed and were counted, contributing to the fossil sample.

Model inputs and sources of data

In order for the model to be able to populate cubic volumes with realistic multispecies assemblages we first created nine parent populations of shells from which specimens could be drawn at random. Each parent population contained 1,000,000 specimens to ensure an adequate sampling universe. In each parent population specimens were distributed among species according to one of three species abundance distributions. Each species was assigned a size value, status as a gastropod or bivalve and shell shape data. Two separate sets of shape data, one for shells assigned as gastropods and the other for shells assigned as bivalves, were used in order to avoid assigning unrealistic shapes. The nine parent populations represented different combinations of three species abundance distributions and three sources of species size data, which are described below. For simplicity, each species was defined by a distinct but uniform size and shape (i.e., there were inter-specific variations in size and shape, but there were no intra-specific variations). The model used shell height (i.e., distance from the dorsal to the ventral sides of specimens) as a measure of size.

Data on species abundances is commonly presented in the paleoecological literature, however these are usually limited to samples of only a few hundred or at best thousands of individuals. Therefore, in order to have a sampling universe sufficient to explore variation in diversity up to sample sizes of thousands of individuals, we chose to generate artificial data sets of size N = 1,000,000 based on realistic parameters. To do this, we used three species abundance distributions: two following the log series distribution (Fisher et al. 1943) and one following the lognormal distribution (Bulmer 1974). Parameter values for the species abundance distributions

were α=3 and α=6 for the two log series distributions and μ = 1.2281 and Σ = 1.240 for the lognormal distribution. A detailed description of how these species abundance distributions were generated is presented in the supplementary methods section in Appendix I. Copies of all MATLAB code used to generate them is included in Appendix II.

Three sources of size data (Kowalewski et al. (2006), Roy et al. (2000), and Sessa et al. (2009)) formed the basis for constructing the parent populations with varying size between model species. The supplementary data set of Kowalewski et al. (2006) provided lists of specimens identified to species level with associated measurements of shell height. The mean of individual species provided a basis for a data set of species sizes. Roy et al. (2000) provided numbers of species assigned to different size bins. Sessa et al. (2009) provided lists of species taken from both her own work and previously published sources. While Sessa et al. (2009) did not provide species size information, one of her sources of species abundance data, Garvie (1996), gave species-level size information including shell heights and width:height ratios and length:height ratios. Measurements were given for the largest specimen of a species. This information was used as a source of size information for the species lists of Sessa et al. (2009). Details of the treatment of size data, including a discussion of different binning methods used in the three data sets, is included in the supplementary methods section. In contrast to specimen size, where three data sets were used to explore the effect of species size, only a single data set on shell shape was used for all analyses. Details of how shape data was used are described in the appendix. Shape data used in the model was taken from two sources, the paleobiology database and Garvie (1996). Shape data were obtained for species lists of Sessa et al. (2009) in order to ensure that the range of within population shapes was realistic.

The Model

Once generated from the compiled data the nine parent populations could then be drawn from to populate model rock volumes. The volumes were populated by randomly drawing specimens, without replacement, from the parent distribution and then randomly assigning them locations in the rock volume (Figs. 2, 3B). The bivalve and gastropod shells created using the Raup model served as the basis for generating specimens of different species that varied in both size and shape. These baseline model shells each possess shell height, width, and length values of 1 mm. Therefore, in order to generate a specimen of a particular size, the baseline set of coordinates were linearly scaled so that the specimen had a shell height equal to the size bin value assigned to its species. For simplicity, each species was associated with only a single size value and ignored intraspecific size variation. The assignment of a single size category to all members of a species is obviously an over simplification as in reality specimens would exhibit size variation based on ontogenetic stage and other factors. Since individuals of the same species within an assemblage will differ in size the true difference in the likelihood of two equally abundant species being sampled via intersection can be more correctly thought of as being related to their difference in mean shell size (i.e., shell height). Therefore, the single sizes assigned to species in the present model can be thought of as corresponding to mean shell heights. This is accurate for the Kowalewski and Hoffmeister (2003) size data set given that these sizes were generated by taking the mean shell sizes of all entries for each species, however it represents a greater departure from reality for the other two size data sets. Never the less the comparison of the different size distributions is useful in assessing how much differences in the size distribution of an assemblage can influence how much of an effect preferential intersection can have on estimates of diversity. The question of whether incorporating within-species size variation and other complexities not

addressed here significantly alters the biasing impact of preferential intersection will be investigated in future modeling efforts.

Specimen shape was modified by the model in association with size modification. While the shell heights were scaled only by the size bin value, the shell lengths and widths were scaled additionally by the length or width aspect ratios, respectively. Again, for simplicity, each species was associated with only a single shape and intraspecific shape variation was ignored. Specimens were assigned random locations within the cubic volume one at a time in order of decreasing size. The model assessed whether each newly placed specimens intersected with any previously placed specimen and if intersection was detected, location assignment was repeated until no specimen intersection occurred. Details of how the model handled the assessment of specimen intersection are presented in the supplementary methods.

Once a volume was populated by specimens, one or more positions along the vertical axis between the top and bottom of the volume were selected at random (Fig. 3C). These points represent fracture horizons. All specimens that intersected one or more of these horizons were counted by the code, and their species identity and associated information recorded. The code recorded the species identity and size for each intersected specimen in a master list of sampled specimens. The code continued to generate and sample populated volumes until a user-supplied sample size quota was met. This quota represents the total sample size and is represented in the horizontal axis in Figures 4–6. In different model runs, the quotas were set at 10, 50, 100, 150, 200, 250, and 300 specimens, allowing us to examine the effects of different sample sizes on the magnitude of bias induced by preferential intersection.

Considering all intersected specimens as equally exposed is likely to also be an over simplification since differences certainly exist in how easily species can be identified when only

partially exposed. This may also represent an additional source of bias. This is analogous the "Chlamys effect" of Kowalewski et al. (2003) in which specimens which can be identified even as small fragments are numerically dominant. However this simplifying assumption is acceptable given that the purpose of the model is to evaluate whether preferential intersection is capable of imparting a bias on its own and not to replicate all the possible contributing factors to the lithification bias.

Once the quota was reached, the code calculated the species richness, evenness, and average specimen size of the sample. For evenness, the code calculated Peilou's J (Pielou 1966), again based on the master list. For average specimen size, the code simply took the average size of all specimens on the master list regardless of species identity. As a null to compare against the model of preferential intersection, we also employed a random draw model. This model simply draws a quota of specimens at random from the same parent distribution used to populate the model volumes. This model is analogous to fossil collection by sieving unconsolidated sediments and retrieving all specimens contained within a given volume of sediments. A random draw model has previously been used to model fossil collection via sieving in a study of biases associated with choice of mesh size (Kowalewski and Hoffmeister 2003). Like the preferential intersection model, the random draw model was repeated 150 times for each quota size in order to calculate the mean and 95% confidence interval of species richness, evenness, and average specimen size.

The nine parent populations described above provided a basis for assessing how the magnitude of bias induced by preferential intersection varied in response to changes in the species abundance distribution and the distribution of species among size classes. Each parent population was run through both the preferential intersection and random draw models. The resulting curves of mean values and confidence intervals for species richness, assemblage evenness, and average

specimen size allowed us to examine how the magnitude of the bias changed with sample size for each combination of species abundance distribution and species size data set. We also performed one-tailed t-tests on sets of 150 values produced by the preferential intersection and random draw models, at a sample size of 300 specimens, to determine whether the two models produced significantly different richness, evenness, and average specimen size. T-tests were performed using the 't.test' function in R.

Results

Figures 4–6 show mean values and 95% confidence envelopes of species richness, evenness, and average specimen size by the preferential intersection and random draw models. Pairs of results were generated by running each of the two models using one of the nine combinations of species abundance distribution and species size data (Table 1). Examination of the results demonstrates that, with rare exceptions, the preferential intersection model consistently gave lower richness, lower evenness, and greater average specimen size compared with the random draw model (Table 2). The magnitude of this difference varies depending on the specific combination of abundance and size distributions. Table 1 shows model results of species richness, evenness, and average specimen size for each combination of species abundance and size distributions. Table 2 shows the results of one tailed t-tests assessing whether outputs of the preferential intersection model were significantly greater or lower than those of the random draw model.

Table 1. Results of model runs (quota = 300).

Abundance distribution	Size distribution	Species richness		Sample evenness		Average specimen size (mm)	
		Random draw	Preferential interaction	Random draw	Preferential interaction	Random draw	Preferential interaction
Logseries Distribution, Alpha = 3	Roy et al. (2000)	15.5	13.7	0.76	0.60	23.7	39.8
	Kowalewski et al. (2006)	15.5	14.8	0.76	0.67	6.47	8.0
	Sessa et al. (2009)	15.7	17.7	0.76	0.77	5.87	8.95
Logseries Distribution, Alpha = 6	Roy et al. (2000)	30.1	25.0	0.84	0.75	40.9	55.6
	Kowalewski et al. (2006)	30.6	26.28	0.84	0.77	9.15	12.4
	Sessa et al. (2009)	30.2	23.3	0.84	0.63	12.5	31.3
Lognormal Distribution	Roy et al. (2000)	41.56	37.07	0.85	0.80	33.5	62.3
	Kowalewski et al. (2006)	41.96	37.87	0.85	0.80	7.09	8.88
	Sessa et al. (2009)	42.09	34.56	0.85	0.79	11.5	23.7

Table 1

Table 2. Results of significance tests (quota = 300). RD: random draw model. PI: preferential intersection model.

Abundance distribution	Size distribution	Species richness		Sample evenness		Average specimen size (mm)	
		Random draw	Preferential interaction	Random draw	Preferential interaction	Random draw	Preferential interaction
Logseries Distribution, Alpha = 3	Roy et al. (2000)	RD > PI, p = <2.2E-16		RD > PI, p = <2.2E-16		RD < PI, p = <2.2E-16	
	Kowalewski et al. (2006)	RD > PI, p = 6.18E-06		RD > PI, p = <2.2E-16		RD < PI, p = <2.2E-16	
	Sessa et al. (2009)	RD < PI, p = <2.2E-16		RD < PI, p = 3.76E-06		RD < PI, p = <2.2E-16	
Logseries Distribution, Alpha = 6	Roy et al. (2000)	RD > PI, p = <2.2E-16		RD > PI, p = <2.2E-16		RD < PI, p = <2.2E-16	
	Kowalewski et al. (2006)	RD > PI, p = <2.2E-16		RD > PI, p = <2.2E-16		RD < PI, p = <2.2E-16	
	Sessa et al. (2009)	RD > PI, p = <2.2E-16		RD > PI, p = <2.2E-16		RD < PI, p = <2.2E-16	
Lognormal Distribution	Roy et al. (2000)	RD > PI, p = <2.2E-16		RD > PI, p = <2.2E-16		RD < PI, p = <2.2E-16	
	Kowalewski et al. (2006)	RD > PI, p = <2.2E-16		RD > PI, p = <2.2E-16		RD < PI, p = <2.2E-16	
	Sessa et al. (2009)	RD > PI, p = <2.2E-16		RD > PI, p = <2.2E-16		RD < PI, p = <2.2E-16	

Table 2

Discussion

Preferential intersection as a source of bias on species richness, evenness and average specimen size

Model outputs shown in Tables 1–2 and Figures 4–6 illustrate that, with one important exception which will be discussed in more detail below, the preferential intersection model consistently yielded samples with lower species richness, lower evenness, and a greater average specimen size than counterparts produced by the random draw model. These results demonstrate that fossil sampling from well-lithified sediments via splitting can bias aspects of species diversity even without the loss of specimens due to aragonite dissolution, raising an important point about

discussions of the lithification bias. As first used by Sessa et al. (2009) and Hendy (2009), the term "lithification bias" refers to the empirically observed difference between fossil samples from lithified and unlithified sediments. However, there is a potential for confusion if the term 'lithification bias' is taken to imply that any bias must be the result of processes that occurred *during* the transition from unlithified to lithified sediments. Avoiding this conceptual confusion is important for considering variation between the results of different studies. Already different studies have come to different conclusions concerning the magnitude of the lithification bias [i.e., the different magnitudes observed by Sessa et al. (2009) and Hendy (2009)]. Sanders et al. (2015) presented convincing evidence of lithification bias in the Eocene of the Paris Basin that was driven largely by the dissolution of aragonitic taxa. Maintaining a clear distinction between the lithification bias and its causes is important for evaluating examples of this bias on a case by case basis.

The variability in the magnitude of the bias between model runs demonstrates that the exact magnitude of the difference in species richness is dependent on properties of the population being sampled. This is not particularly surprising. However, it demonstrates the need to consider how vulnerable a particular assemblage may be to the biasing effects of preferential intersection. The absolute values of the difference with the preferential intersection and random draw models varied between species abundance distributions that differed in richness and evenness. When absolute differences were converted to percent differences, the magnitude of the difference in species richness was 10–20% between the two models. The only outliers were model runs for the logseries with $\alpha = 3$ and the Kowalewski et al. (2006) size data set, which produced a percent difference in species richness of just 5%, and the logseries distribution with $\alpha = 6$ and the Sessa et al. (2009) size data, which produced a difference in species richness of 23%. Results for assemblage evenness

were similarly variable, with differences between the preferential intersection and random draw models ranging from 5–25%. Fossil collection from lithified sediments via splitting is therefore expected to yield samples with lower species richness and lower evenness than would have been recovered from a sample of the same size collected via sieving, with the magnitude of this difference most likely falling between 10–20% for species richness and 5–25% for assemblage evenness, independent of the effects of other biasing mechanisms.

The lone exception to the trend of lower species richness and evenness from the preferential intersection model was for model runs that used the logseries with $\alpha = 3$ and the Sessa et al. (2009) size data set, shown in Figure 4C and 4F. In this model run both species richness and assemblage evenness were greater for the preferential intersection model than for the random draw model. As shown in Table 2, this difference is statistically significant. This result can be understood by considering that, in the preferential intersection model, the likelihood of a specimen being sampled is tied to its size, specifically in this case shell width or the shell dimension in the vertical axis. In cases where larger specimens are concentrated among rarer species, or common species are smaller, sampling via splitting could through preferential intersection lead to the recovery of a greater number of rare species than would be expected at random. This result is consistent with the finding of Daley and Bush (2014) that splitting artificial rocks populated with specimens actually produced greater species richness than would be expected from randomly drawing from the same population. This reiterates the conclusion that the effect of preferential intersection on aspects of assemblage diversity depends on properties of the assemblage.

Preferential intersection as a component of the lithification bias

All model runs produced some degree of difference in species richness, evenness, and average specimen size between the random draw and preferential intersection models regardless

of which combination of size distribution and species abundance distribution was used. However, it does not follow from this that preferential intersection can fully explain the bias observed by Sessa et al. (2009) and Hendy (2009). Determining the extent to which preferential intersection can explain the observed lithification bias, either in part or in whole, requires comparing the model results with empirical studies. The largest difference between the random draw and preferential intersection models was generated when the logseries species abundance distribution was used with $\alpha = 6$. In these model runs, the species richness of random draw samples at a sample size of 100 was approximately 22 species, which is comparable to the richness values of 20 species reported by Hendy (2009) from unconsolidated sediments. The preferential intersection model yielded an average species richness of 16 species, 25% fewer species than the random draw model. By contrast, Hendy (2009) reported an average species richness of 10 species for lithified samples of this size. Sessa et al. (2009) reported an even greater difference between lithified and unlithified collections, with their average unlithified richness being approximately 20 species but their lithified collections yielding a richness of only 5 species. These comparisons indicate that preferential intersection can account for 20–25% of the observed lithification bias reported in the literature.

Since preferential intersection cannot explain the entire observed richness difference between lithified and unlithified sediments, other mechanisms must also be invoked to explain the remaining difference in diversity. The most obvious candidates are the two additional mechanisms for the lithification bias that have been proposed in the literature—namely, dissolution of small aragonitic specimens and mechanical destruction during splitting. Importantly, all three of these mechanisms are thought to affect similar taxa. The small, thin-shelled aragonitic taxa that are at the highest risk for dissolution are also the most likely to be missed due to preferential intersection

and the most likely to be vulnerable to mechanical breakage during collection. It follows that the effects of these biases are more likely to be redundant than additive. An assemblage that has lost its smallest taxa due to aragonite dissolution is likely to yield similar diversity values whether collected from well-lithified or unconsolidated sediments, because those specimens that were most vulnerable to the effects of preferential intersection have already been removed. At the same time, fossil assemblages may exhibit similar losses of small taxa due to any combination of the above mechanisms. Demonstrating that a fossil assemblage has not been significantly affected by one of these mechanisms does not imply that it is unaffected by the others. For example, demonstrating the presence of abundant small aragonitic taxa does not mean that preferential intersection does not exert a bias.

Impact of preferential intersection on older fossil assemblages

The analyses of preferential intersection performed here were based on size and aspect ratio data derived from assemblages of Cenozoic mollusks. Conclusions about the likely impact of preferential intersection on diversity measures of brachiopod-dominated assemblages of the Paleozoic, particularly the lower Paleozoic, and transitional assemblages in the Mesozoic, must await further studies since the ranges of size and shell dimensions (i.e., aspect ratios) used here may not be applicable to these assemblages. At this point we can only propose educated speculation on the likely impact of preferential intersection on Paleozoic and early Mesozoic assemblages, with the caveat that further modeling work targeting these assemblages is needed. Examinations of evenness through the Phanerozoic suggest that Paleozoic assemblages are predominately low-evenness, high-dominance assemblages (Bush and Bambach 2004; Powell and Kowalewski 2002). Wagner et al. (2006) also found that Paleozoic assemblages are best described by the logseries species abundance distribution. Thus, they most closely resemble samples in this study fitting the logseries distribution with $\alpha = 3$. In model runs, the effect of preferential

intersection was low, with a richness difference between the preferential intersection and random draw models of 4–12%. For these low diversity assemblages, this translates to absolute differences of only one or two species. Therefore, it is likely that the biasing effect of preferential intersection on species richness of brachiopod-dominated Paleozoic assemblages would be no greater than the lowest differences observed in this study. However, even if the impact of preferential intersection on brachiopod dominated Paleozoic assemblages were determined to be negligible, it would not necessarily follow that species richness of these assemblages are unaffected by other biasing mechanisms, only that preferential intersection can be ignored for these cases, and that any instance of lithification-related bias affecting species richness in brachiopod-dominated Paleozoic assemblages must be driven by other mechanisms.

Conclusion

Understanding how to correct for lithification biases requires identifying the process or processes that generate such biases. The work presented here demonstrates that preferential intersection, i.e., the higher probability of sampling larger specimens relative to smaller ones due to their greater likelihood of being intersected and thus being visible on split surfaces, can have a biasing effect on species richness, sample evenness, and average specimen size of fossil samples. Preferential intersection is therefore a potential contributing factor to the lithification bias. Analogue modeling results suggest that preferential intersection cannot fully explain observed differences between lithified and un-lithified fossil assemblages and therefore other mechanisms such as aragonite dissolution likely contribute to the lithification bias. Nevertheless, the biasing effect of preferential intersection should be taken into account when fossil collections are made by splitting well-lithified sedimentary rocks. This work demonstrates that the empirically observed lithification bias is complex and, at least in some cases, may be the result of multiple factors and should not be considered synonymous with the aragonite bias.

Figure Captions

Figure 2.1. Examples of a bivalve (left; a single valve) and a gastropod (right) generated using Matlab code that implemented Raup's coiling model. Axes are in millimeters.

Figure 2.2. An example of a populated volume. The number of specimens placed within each volume was defined by the user and was limited by the requirement that specimens cannot penetrate one another. Axes are in millimeters

Figure 2.3. The stages of model population and sampling. (A) An initial volume was defined based on user-defined size parameters. (B) This volume was then populated by specimens randomly drawn from a parent distribution. This was an iterative process that began with the largest specimen being assigned a random set of three dimensional coordinates within the volume that defined its location. New specimens were placed within the volume in order of decreasing size. Each newly placed specimen was assessed to determine whether it penetrated any previously placed specimens. If it did, then it was randomly assigned a new location until it did not penetrate any existing specimens. (C) One or more horizontal planes within the volume were randomly selected to represent fracture surfaces that intersected specimens. (D) Finally, the species identity and size of each intersected specimen were stored in a master list. If the user-defined sampling quota had not been reached, a new populated volume was generated and the procedure was repeated until the quota was met.

Figure 2.4. Results of model runs using all three size distributions and a logseries species abundance distribution with alpha = 3. Circles and brackets represent the mean values and 95% confidence intervals.

Figure 2.5. Results of model runs using all three size distributions and a logseries species abundance distribution with alpha = 6. Circles and brackets represent the mean values and 95% confidence intervals.

Figure 2.6. Results of model runs using all three size distributions and a lognormal species abundance distribution (mu = 1.2281, sigma = 1.2408). Circles and brackets represent the mean values and 95% confidence intervals.

Figure 2.7. The three size distributions used in the model. (A) Plotted in absolute size bins. (B) The same data plotted in relative size bins (i.e., fraction of the largest bin).

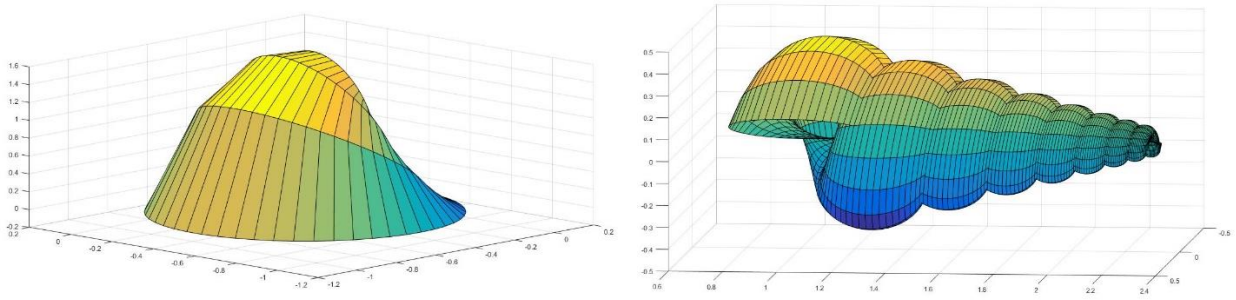

Figure 2.1

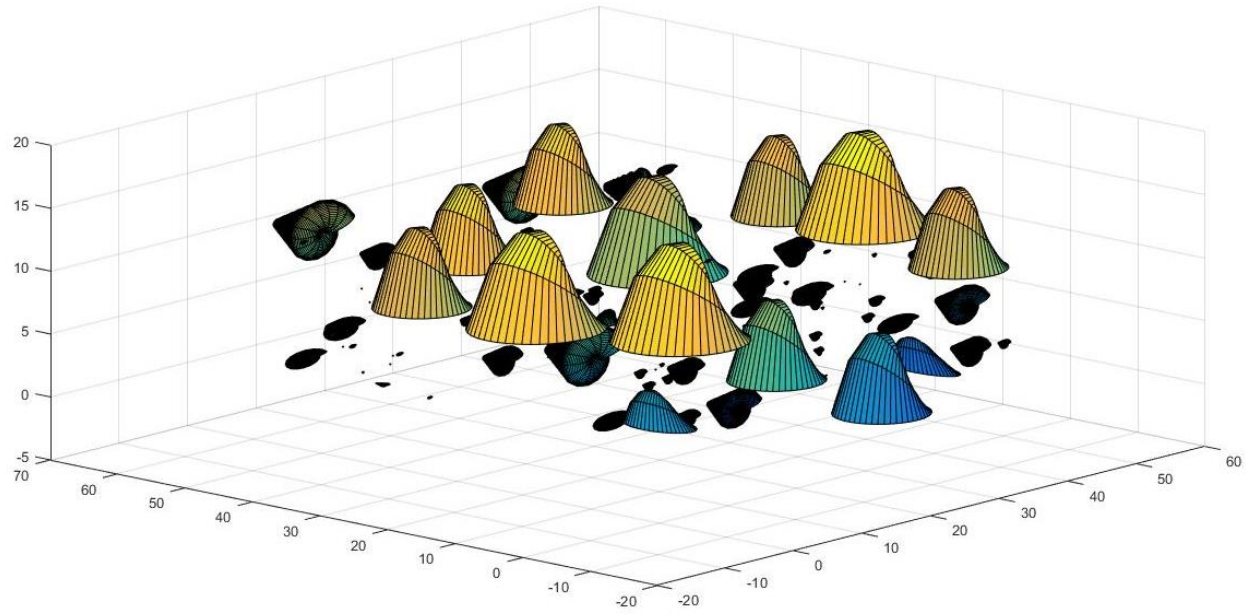

Figure 2.2

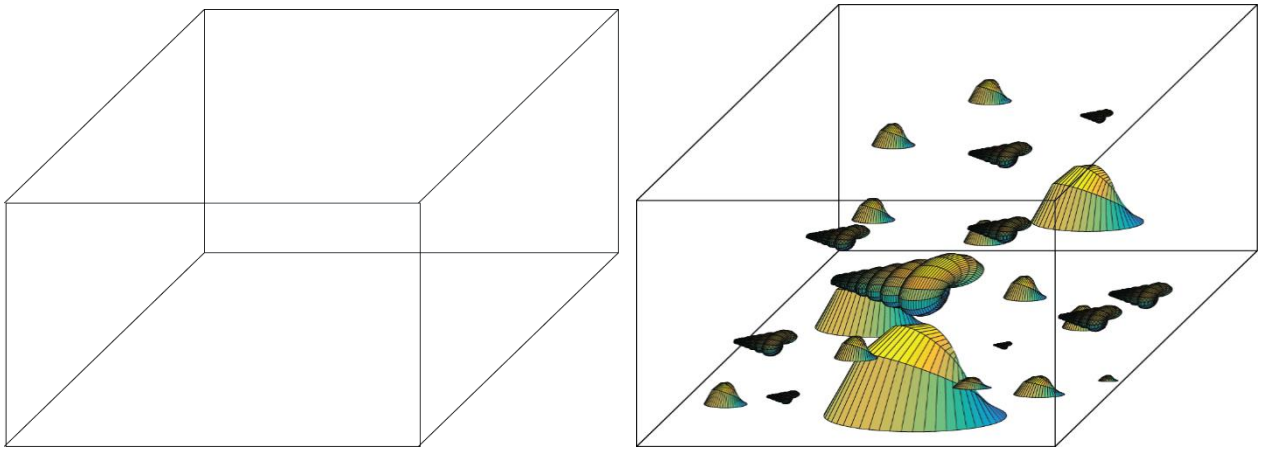

A. **B.**

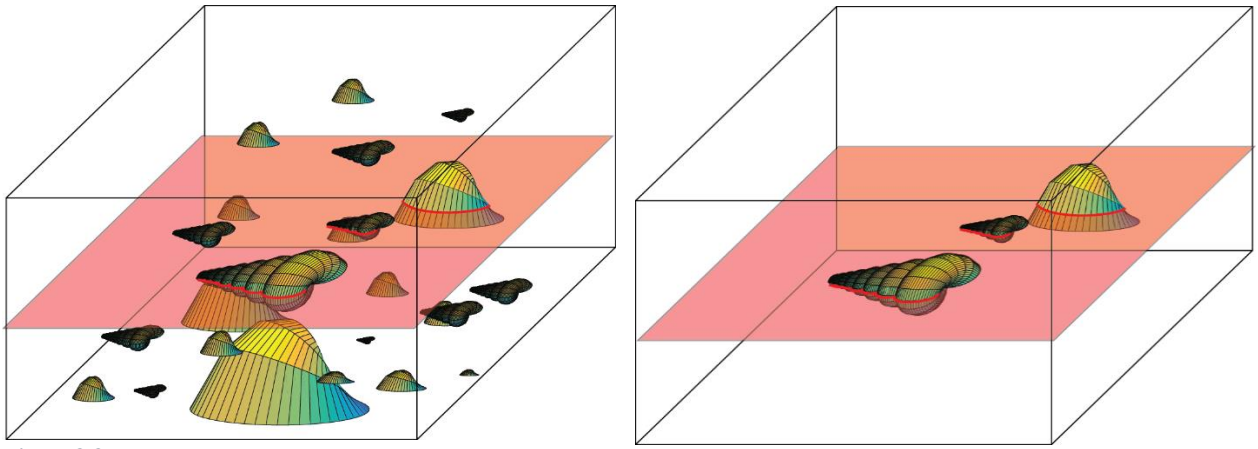

Figure 2.3

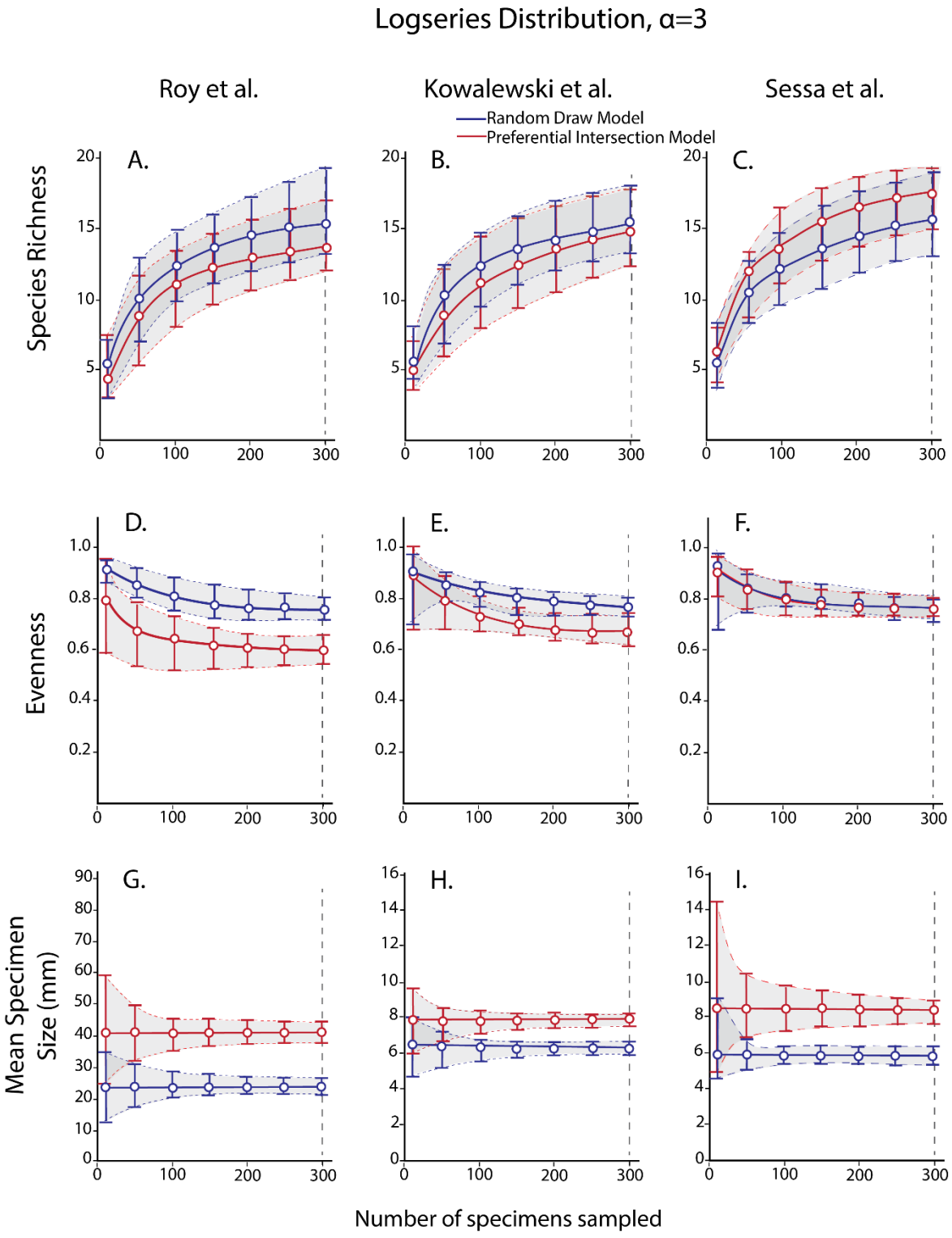
Logseries Distribution, α=3
Roy et al.
Kowalewski et al.
Sessa et al.
Random Draw Model
Preferential Intersection Model
A.
B.
C.
D.
E.
F.
G.
H.
I.
Species Richness
Evenness
Mean Specimen Size (mm)
Number of specimens sampled

Figure 2.4

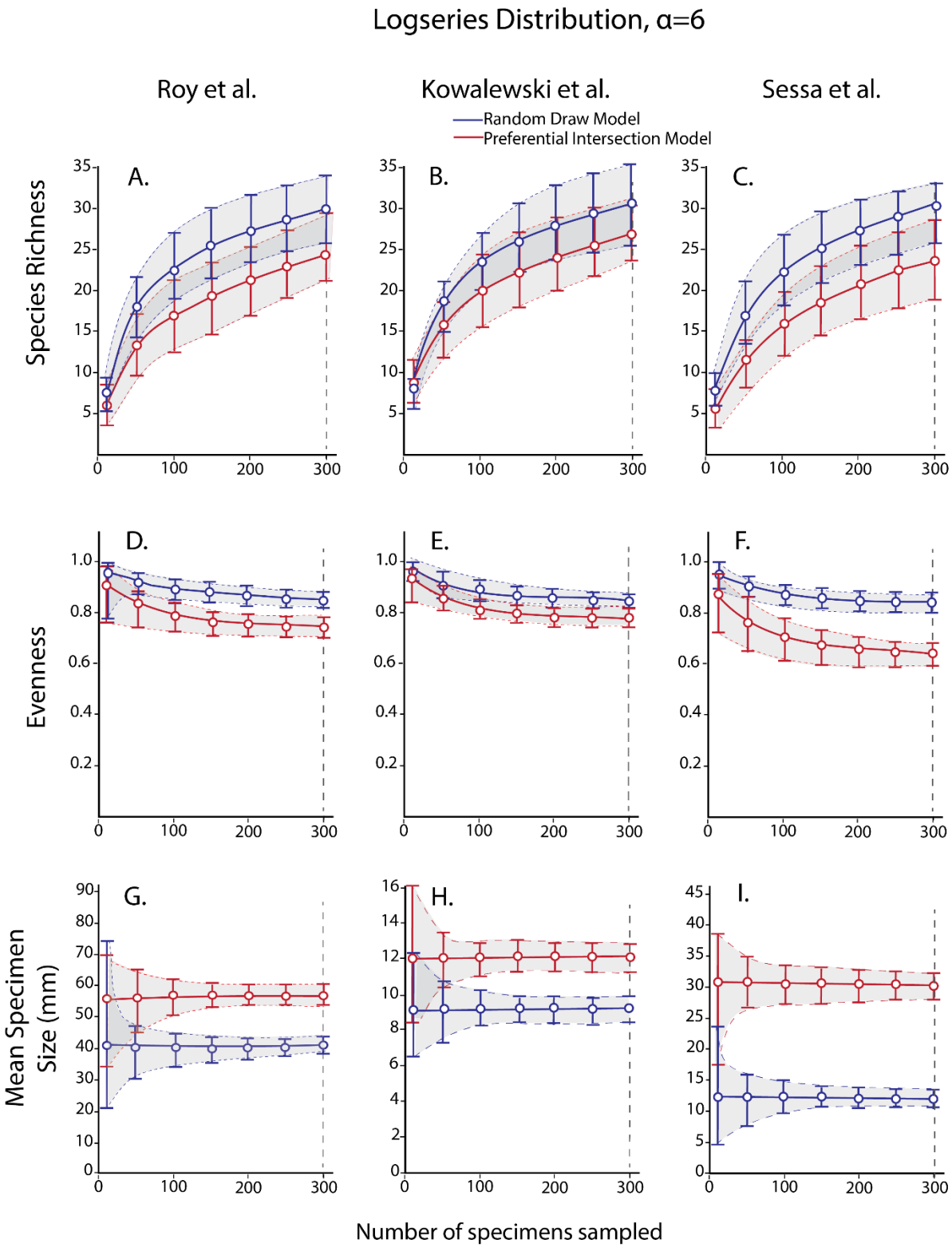
Logseries Distribution, α=6
Roy et al.
Kowalewski et al.
Sessa et al.
Random Draw Model
Preferential Intersection Model
A.
B.
C.
D.
E.
F.
G.
H.
I.
Species Richness
Evenness
Mean Specimen Size (mm)
Number of specimens sampled

Figure 2.5

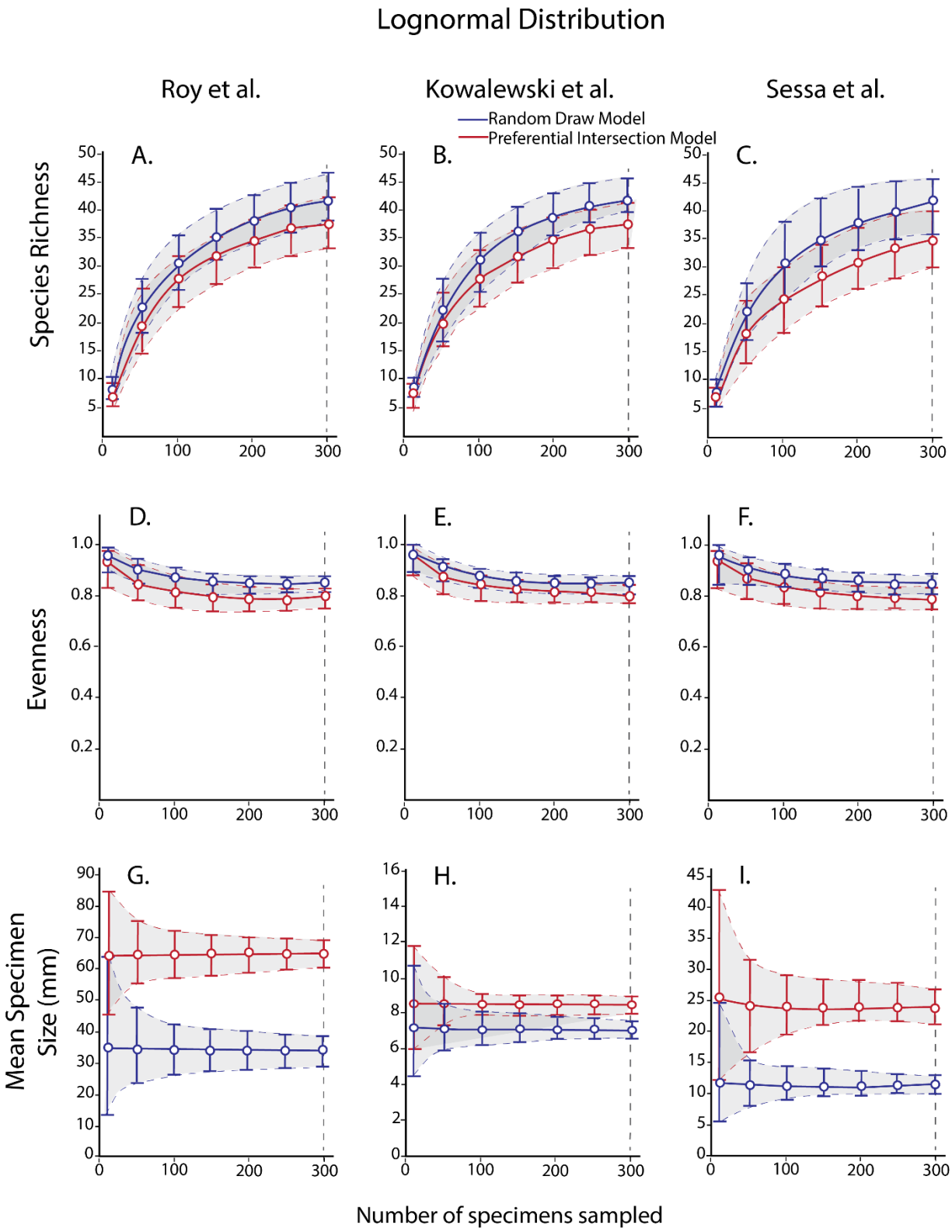
Lognormal Distribution
Roy et al.
Kowalewski et al.
Sessa et al.
Random Draw Model
Preferential Intersection Model
A.
B.
C.
D.
E.
F.
G.
H.
I.
Species Richness
Evenness
Mean Specimen Size (mm)
Number of specimens sampled

Figure 2.6

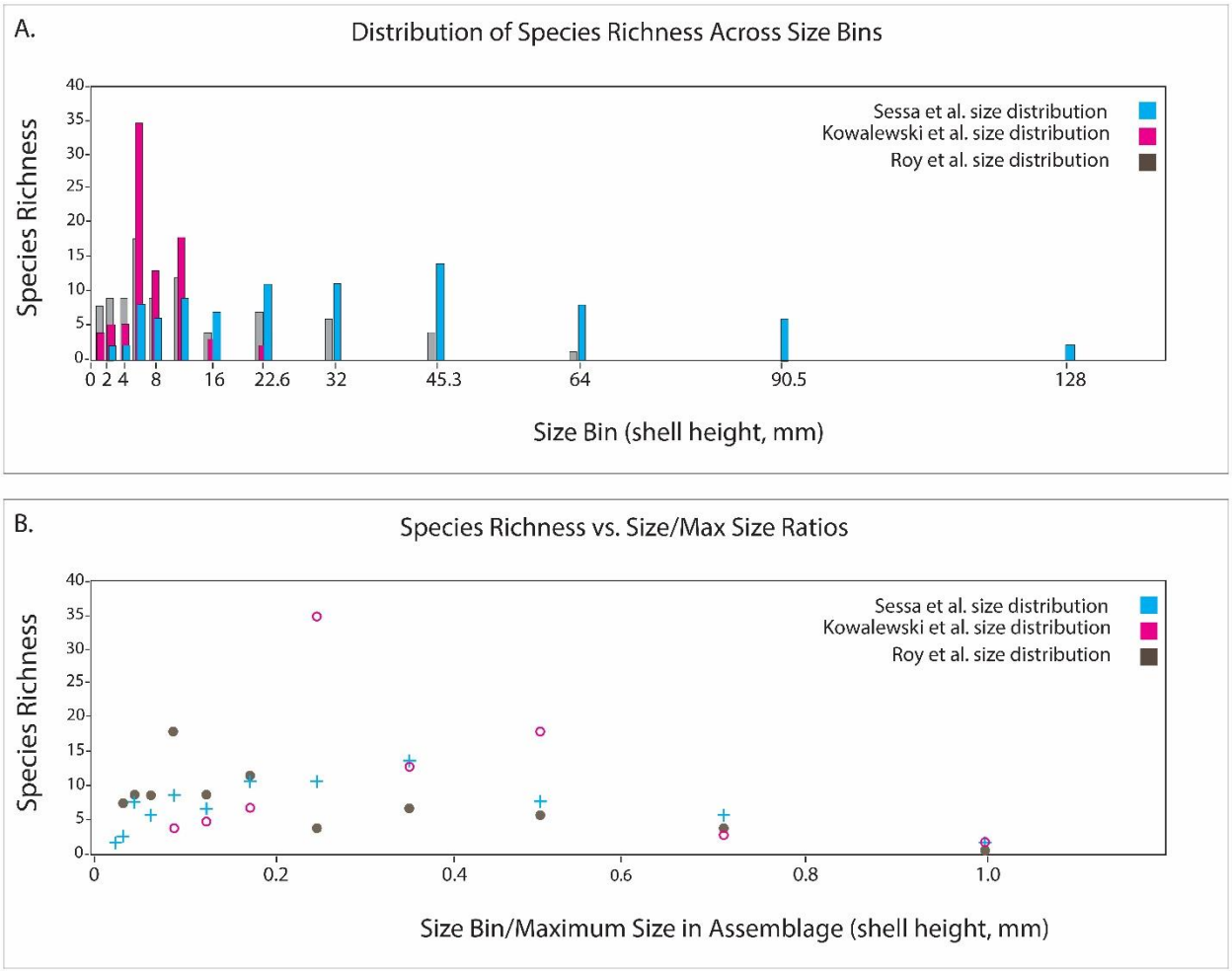
A.
Distribution of Species Richness Across Size Bins
Species Richness
Sessa et al. size distribution
Kowalewski et al. size distribution
Roy et al. size distribution
0 2 4 8 16 22.6 32 45.3 64 90.5 128
Size Bin (shell height, mm)
B.
Species Richness vs. Size/Max Size Ratios
Species Richness
Sessa et al. size distribution
Kowalewski et al. size distribution
Roy et al. size distribution
0 0.2 0.4 0.6 0.8 1.0
Size Bin/Maximum Size in Assemblage (shell height, mm)

Figure 2.7

Chapter 3 Vermiform fossils

Abstract

The Winneshiek Lagerstätte occurs within a Middle Ordovician meteorite impact structure beneath part of the city of Decorah, Iowa. The Lagerstätte has yielded an atypical fauna including phyllocarid crustaceans, eurypterids, conodonts, linguloid brachiopods, and jawless fish. Associated with these taxa are vermiform fossils: elongate, morphologically simple and variable, and often three-dimensionally preserved bromalites of uncertain organisms. The preservational state of these bromalites is significantly different from other components of the Winneshiek biota. Here we present a compositional and microstructural analysis of the specimens in order to elucidate their taphonomy and biological affinities. The analyzed specimens are often composed of calcium phosphate and consist of micrometer-sized microspherules. Winneshiek bromalites exhibit important similarities to examples documented from both older and younger sediments. They provide independent evidence of predation in the Winneshiek assemblage during the Great Ordovician Biodiversification Event (GOBE).

Introduction

The Winneshiek Lagerstätte in northeastern Iowa was discovered in 2005 (Liu et al. 2006) and provides a rare example of a Middle Ordovician Lagerstätte (Van Roy et al. 2015). Deposited and preserved within a previously unrecognized meteorite impact structure (Fig. 1), the stratigraphic unit hosting the Winneshiek Lagerstätte, the Winneshiek Shale, is a spatially restricted green-grey laminated shale that lacks common elements of normal marine Ordovician communities such as trilobites, graptolites, articulate brachiopods, or bryozoans. Instead, the

Winneshiek fauna is dominated by a variety of arthropods, including phyllocarid crustaceans and eurypterids, as well as conodonts, placoderm fishes, and linguloid brachiopods. The Winneshiek fauna is characterized by exceptional preservation, including arthropods preserved as carbonaceous compressions, and multiple species of conodonts preserved as bedding plane assemblages (Liu et al. 2017; Liu et al. 2006).

Associated with these familiar taxa are three-dimensionally preserved bromalites referred to as "vermiform fossils" by Liu et al. (2006). Bromalites are one of the most common components of the Winneshiek fauna representing 26% of specimens (Briggs et al. 2015). They are morphologically variable, but are characterized by a roughly cylindrical shape and a surface texture featuring concentric wrinkles or bands. Liu et al. (2006) argued that, whereas some of these structures may represent coprolites, others show a regularity of external morphology and internal structure that makes the coprolite interpretation unlikely. Subsequent authors have referred to the Winneshiek vermiform structures as bromalites (Briggs et al. 2015; Liu et al. 2017), a trace fossil category that includes cololites, the mineralized contents of digestive organs (Hunt 1992), as well as coprolites. Here we report a systematic investigation of these structures to determine their formation, mode of preservation, and likely trace maker.

We analyzed a set of bromalites from the Winneshiek Shale, examining the details of their external morphology, and used these observations to develop a list of morphological features occurring across multiple specimens. We utilized light and scanning electron microscopy to investigate polished slabs and thin sections of specimens in order to characterize their internal structure and mineralogical composition. The morphological and compositional features were then compared with those of other bromalite assemblages and modern fecal pellet assemblages described in the literature.

Geologic Setting and Background

The Winneshiek Shale

The Middle Ordovician Winneshiek Shale was first recognized within cores and well cuttings in the early 2000's, which revealed a green to grey shale underlying the Tonti Member of the St. Peters Formation (Liu et al. 2017). The occurrence of this unit is restricted to a circular area with a diameter of approximately 5.6 km around the city of Decorah, Iowa (McKay et al. 2011; Witzke et al. 2011). The shale unit is underlain by a previously unrecognized breccia, a unit containing clasts and sediments derived from underlying Cambrian and Lower Ordovician strata. Stratigraphic deformation and brecciation are also evident at the edge of the circular basin. Petrographic examination of quartz grains from core and well cuttings of the breccia unit has documented the presence of shock-deformation features diagnostic of meteorite impact origin. Taken together, these individual pieces of evidence suggested the existence of a previously unrecognized meteorite impact structure located beneath the city of Decorah (Fig. 1) (Liu et al. 2009; McKay et al. 2011; McKay et al. 2010). Aerial electromagnetic and gravity surveys operated by the U.S. Geological Survey clarified the spatial extent and geometry of this structure, which was named the Decorah impact structure (Kass et al. 2013a, b). The age of the impact event and of the Winneshiek Shale subsequently deposited within the crater is constrained as Middle Ordovician (the Darriwilian International Stage, or Whiterockian in U.S. Series terminology) by both the surrounding stratigraphic context and, especially, by conodonts in the Winneshiek Shale (Liu et al. 2017). The Decorah impact structure is one of several Middle Ordovician impact structures that have been discovered in recent years. These structures, along with low marine osmium isotope ratios that suggest the enhanced addition of meteorite-derived osmium to the

oceans, have been used to argue for an increased frequency of asteroid impacts related to a breakup of the l-chondrite belt during this time (Korochantseva et al. 2007; Schmitz et al. 2008).

The depositional setting of the Winneshiek Shale within the impact crater differed significantly from the surrounding and underlying strata (McKay et al. 2011; McKay et al. 2010). The Winneshiek Shale is organic rich, with total organic carbon contents up to 1.5% based on Rock-Eval analysis. Pyrite framboids are abundant. The green-grey shale is laminated with essentially no evidence of bioturbation. These observations suggest that the paleoenvironment that formed in the impact crater was that of a restricted basin with dysoxic or anoxic bottom waters (Liu et al. 2009; McKay et al. 2011).

Winneshiek Biota and Exceptional Preservation

The Winneshiek biota comprises a suite of taxa that supports its interpretation as hosted by a restricted embayment or estuary with low dissolved oxygen levels, marginal to the main Whiterockian seaway (Witzke et al. 2011). The biota is dominated by conodonts and arthropods, with abundant bromalites as well as inarticulate brachiopods, algae, and possible fishes. As noted above, common constituents of normal marine communities such as articulate brachiopods and trilobites are absent. The arthropods include the phyllocarid *Ceratiocaris winneshiekensis*, the oldest known representative of the Ceratiocarididae (Briggs et al. 2015), the oldest described eurypterid (Lamsdell et al. 2015b), a basal euchelicerate arthropod (Lamsdell et al. 2015a), and several species of ostracods (Briggs et al. 2015). Additionally, organic-walled microfossils have been extracted from the Winneshiek Shale using palynological techniques (Nowak et al. in press). Conodonts include new complete giant apparatuses as well as individual elements (Liu et al. 2017). Possible jawless fishes are represented by articulated head shields (Liu et al. 2006). Linguloid

brachiopods as well as a single gastropod specimen have also been found. The character of the Winneshiek biota differs from other shelly faunas, including the Upper Ordovician Lagerstätten at McBeth Point, Williams Lake, and Airport Cove in Manitoba, Canada (Young et al. 2013; Young et al. 2007) and the Stonington Peninsula in Michigan (Lamsdell et al. 2017), thought to also represent restricted marginal marine paleoenvironments. No fossils similar to the Winneshiek bromalites have been described from these sites.

Methods

Following the discovery of the Winneshiek Shale in cores and well cuttings, an artificial section was created along a small exposure by the Upper Iowa River using a back hoe. This area of the river is normally submerged and was cordoned off for excavation in the summer of 2010. More than 5,000 specimens of arthropods, conodonts, bromalites, and other components of the Winneshiek biota were collected. Most of the bromalites used in this study were collected during the 2010 excavation, although some specimens were obtained from slabs that were washed out of the river bed during flooding. All specimens examined in this study are reposited at the Paleontology Repository, Department of Earth & Environmental Sciences, University of Iowa (catalog numbers with a prefix of SUI).

A combination of transmitted light, reflected light, and electron microscopy was used to examine the internal and surficial microstructures of a morphologically diverse set of bromalites that were naturally exposed or thin-sectioned. Fifty-six specimens were observed under a reflected light microscope and their external morphologies were documented. Thirteen specimens were cut and polished for SEM examination, and five of them were prepared for standard 30-μm petrographic thin sections. One of the thin sections intersected an unexposed bromalite, so that a

total of 14 sectioned specimens were examined by SEM. Thin sections were examined using an Olympus BX-51 transmitted light microscope. Compositional data and elemental maps were obtained from polished slabs and thin sections on a Hitachi TM3000 table top SEM with a Bruker XFlash EDS system using an accelerating voltage of 15 kV and a working distance of 12 mm, and with a FEI Quanta 600F low vacuum environmental SEM using accelerating voltages of 5-20 kV and a working distance of 5–13 mm. The majority of images were taken in backscattered electron (BSE) mode as this revealed more internal structure of interest, but in some cases secondary electron (SE) imaging was used. The BSE mode generates greyscale images with contrast reflecting composition, topography, and packing density. The SE mode, in contrast, uses secondary electrons and the image contrast mainly reflects topography. We also analyzed the composition of two bromalites in thin section using a Cameca SX-50 electron microprobe. Microprobe point analysis provided quantitative information on elemental composition of vermiform specimens and the enclosing matrix.

Results

Composition

Most bromalites from the Winneshiek are more or less cylindrical in shape (Figs. 2–4). Elemental mapping of longitudinal thin sections indicated that specimens are composed of calcium phosphate (Fig. 2). Microprobe analysis confirmed that calcium and phosphorus are abundant and that fluorine is present in appreciable amounts (Table 1), suggesting that the specimens are composed of carbonate fluorapatite. These results indicate that phosphatization was the primary preservation pathway. Some specimens exhibit significant amounts of pyrite (Fig. 3J–K) and sphalerite (Fig. 3N). Calcite is also present in some specimens and is inferred to have replaced apatite secondarily based on the euhedral shapes of calcite rhombs and the fact that they appear to

cross-cut microspherules. A subset of specimens were not phosphatized but preserved as carbonaceous compressions (Fig. 3F). Partially phosphatized structures (Fig. 3L) provide a link between these carbonaceous specimens and the three-dimensionally phosphatized bromalites. An additional subset of vermiform specimens appears to represent featureless membranes infilled with quartz sand; they sometimes appear as patches of sand in the shale (Fig. 4K–N).

External Morphology

The most obvious morphological division among Winneshiek Shale vermiform fossils is between those preserved as carbonaceous compressions and those preserved three-dimensionally. While some ribbon-shaped carbonaceous compressions may also be bromalites, the main focus of this study is the three-dimensional forms, particularly the phosphatized specimens. The three-dimensionally preserved bromalites exhibit some degree of variation in shape, size, and surface texture (Fig. 4). Most of them are elongate, cylindrical, rod-like structures. A small number of specimens exhibit a distinct ovoid morphology that tapers at one end to a neck (Fig. 3A). Another morphological subset is characterized by folded and coiled segments (Fig. 3C–E) that contrast with the straight, rod-like appearance of most specimens.

We recognized five morphological end-members within the three-dimensionally preserved bromalites based on shape and surface texture: (1) densely corrugated and rod-like (Fig. 4A–C); (2) densely corrugated and compressed due to compaction prior to mineralization (Fig. 4D–E); (3) unsculpted and compressed (Fig. 4F–G); (4) unsculpted rod-like (Fig. 4H–J); and (5) patches of quartz sand (Fig. 4K–N), which may represent coprolites of animals that ingested sands but are not the focus of this study. Some specimens exhibit more than one of these end-member textures at different sections along their longitudinal axis (Fig. 5) and others show intermediate

morphologies, suggesting that the variation may be taphonomic in origin due to compaction, deformation, or decay. Variation in bromalites may also be related to differences in the gut contents at the time of death.

Internal Structure of Phosphatized Bromalites

The three-dimensionally phosphatized bromalites vary in their internal structure as revealed in thin section. They commonly show homogenous, densely packed microspherules 2–5 microns in diameter (Fig. 6). The majority of microspherules are transparent but a subset are dark in color to opaque (Fig. 6C–E). These microspherules are present throughout the entire volume of many specimens (Figs. 7–9). Other phosphatic specimens exhibit a less homogenous internal structure. For example, some show distinct concentric bands in transverse cross section (Fig. 3H), one exhibits a distinct transverse "segmentation" in longitudinal cross section (Fig. 3N), and another specimen contains conodont inclusions (Fig. 4O–Q).

Structure of Phosphatic Microspherules

A detailed investigation of polished and thin-sectioned specimens revealed the range of internal structure and composition exhibited by microspherules. Microspherules are a consistent feature of the bromalites (Figs. 6–10), but they differ in nature both within and between specimens. Three different types of microspherule were observed. (1) microspherules consisting entirely of large fluorapatite crystals with no discernable internal structure (Fig. 10G); (2) microspherules consisting of relatively thick concentric layers of carbonate fluorapatite microcrystals and amorphous organic carbon (Fig. 10H–L), with organic carbon sometimes forming C-shaped rather than O-shaped layers (Fig. 10H–K) or occupying the center of microspherules (Fig. 10L); (3)

microspherules consisting of thinner and fully concentric layers of carbonate fluorapatite nanocrystals (Fig. 10M–N).

Certain features of the microspherules appear to be primary, whereas others are likely secondary in origin. For example, the fully concentric layers (Fig. 10M–N) may be a primary structure, forming the *core* of the best preserved microspherules. The C-shaped concentric layers of organic carbon (Fig. 10H–J) are likely secondary, resulting from dissolution and re-precipitation of carbonate fluorapatite microcrystals. Microspherules without any internal structure (Fig. 10G) are probably cast by secondary crystalline fluorapatite. Some microspherules have an outer rim consisting of palisades of carbonate fluorapatite microcrystals that grow on the smooth surface of the microspherule, resulting in an irregular outer surface (Fig. 6E). This rim, here termed the *envelope*, probably results from secondary growth. The space between microspherules, enveloped or non-enveloped, here termed the *inter-microspherule space*, is filled with a matrix of nanocrystalline carbonate fluorapatite that is likely also secondary in origin.

Discussion

Evidence for a bromalite interpretation

Hunt (1992) first coined the term bromalite to encompass specimens representing digestive contents that had either been regurgitated (regurgitalites), expelled as fecal material (coprolites), or were mineralized *in situ* within the digestive organs following the death of an organism (cololites). Hunt (1992) provided a list of criteria by which bromalites could be identified. Several of the taphonomic and morphological features highlighted by Hunt (1992) are evident in the Winneshiek examples and support their interpretation as bromalites. These lines of evidence include: 1) preservational mode, 2) external morphology suggestive of molding by the digestive

or excretory organs, 3) inclusions of incompletely digested skeletal elements of prey items, and 4) evidence for a loss of cohesion or liquefaction as might be expected in poorly consolidated fecal material. While any one of these features may not be sufficient to demonstrate a bromalite origin, because they are also present in other biotic or abiotic structures such as concretions, but taken together provide strong evidence of a bromalite origin.

The high concentration of organic matter present in fecal material provides a substrate for intense microbial activity (Hollocher and Hollocher 2012), which can promote phosphatization if a sufficient external source of phosphate is available. Under normal oxic conditions in freshwater or marine settings, the abundance of bicarbonate ions inhibits precipitation of apatite (Allison 1988; Briggs et al. 1993). Under anoxic conditions, however, the metabolic activity of sulfate reducing and other microbes within fecal material lowers the pH due to release of CO_2 and H_2S as metabolic byproducts. If the pH falls sufficiently, then phosphate precipitation is favored (the "calcium-phosphate switch"; Briggs and Wilby 1996). Bacterial metabolic activity within fecal pellets can thus generate a microenvironment where phosphate mineralization is favored.

Morphology can serve as evidence for identifying bromalites because both coprolites and cololites frequently reflect the shape and internal structure of the digestive and excretory organs (Amstutz 1958; Hunt 1992). Some morphological features exhibited by the Winneshiek examples occur in bromalites elsewhere and/or modern fecal material. These include: 1) A shape that is straight and rod-like (Fig. 4A–C) (Kraeuter and Haven 1970; Peel 2015; Vannier et al. 2014), meandering (Fig. 4D, H–J) (Kraeuter and Haven 1970; Shen et al. 2014), coiled or folded (Fig. 3C–E) (McAllister 1985; Williams 1972); 2) a circular or sub-circular cross-section (Fig. 3G–H) (Hollocher and Hollocher 2012; Kraeuter and Haven 1970; Peel 2015); and 3) a sculpted surface texture consisting of regularly or irregularly spaced transverse corrugations (Fig. 4A–E) (Kraeuter

and Haven 1970; Peel 2015; Vannier et al. 2014) or alternatively a smooth, surface texture (Fig. 4I–J) (Kraeuter and Haven 1970).

None of the three dimensionally phosphatized Winneshiek bromalites examined under SEM or in thin section yielded identifiable inclusions that would serve as direct evidence of ingested material but this is likely a reflection of both the very small sample of specimens investigated in this way and the fact that such structures may be easily missed in cross-sectional observations. Some carbonaceous compression specimens or partly phosphatized specimens, however, reveal inclusions that likely represent partially digested prey items (Fig. 4O–Q). Most of the identifiable material preserved in this way consists of conodonts (Fig. 4O–Q), either as individual elements or assemblages (Liu et al. 2017), phyllocarids (Briggs et al. 2015, their fig. 3), other small arthropods such as ostracods, and linguloids.

Several bromalites from the Winneshiek display evidence of loss of cohesion or liquefaction, including examples that show regular vermiform morphologies over a portion of their length and abruptly transition to irregular morphologies usually with some reduction in three dimensionality (Fig. 5).

The several lines of evidence presented above confirm the interpretation of the Winneshiek vermiform fossils as bromalites and are consistent with a coprolite rather than cololite origin. Hunt (1992, p. 223) pointed out that ‘cololites can only be unequivocally recognized when they are found within the intestinal tract of a fossilized animal’. The bromalites preserved as carbonaceous compressions, however, preserve no evidence of surrounding morphology (an associated conodont apparatus or eurypterid exoskeleton) such as should be present if they represent cololites. Furthermore, although gut traces have been recognized in phyllocarids and other crustaceans of

the Winneshiek fauna (figs. 1.5, 2.7, and 4.1 of Briggs et al. 2015), they are significantly smaller than most of Winneshiek bromalites described here.

The diverse assemblage of Winneshiek vermiform structures joins a number of other lower Paleozoic bromalite assemblages [e.g., Aldridge et al. (2006); Gilmore (1992); Peel (2015); Shen et al. (2014)]. The significant variations in morphology, size, internal component, and external structure of the Winneshiek specimens are partly taphonomic, but may reflect different gut contents and different tracemakers (possible candidates including eurypterids, conodonts, and fishes).

Taphonomy

Three factors are important to the relative frequency of bromalite phosphatization: transport and accumulation of fecal material in appropriate depositional settings, an internal source of phosphate, and an organic composition that facilitates microbial metabolism and thus enables the generation of microenvironments conducive to mineralization (Hollocher and Hollocher 2012). Preservation of coprolites and cololites most frequently occurs within low-oxygen and low-energy aqueous settings (Hollocher and Hollocher 2012). Such low-energy and low-oxygen conditions are necessary to prevent rapid destruction of fecal material due to the actions of bioturbators and coprophagous scavengers. Low-oxygen conditions also favor microbial sulfate reduction, which drives pH changes that promote phosphatization (Briggs et al. 1993; Broce et al. 2014). The finely laminated, organic-rich character of the Winneshiek Shale combined with the rarity of benthic taxa (only occasional linguloid brachiopods are present; Liu et al. 2006) indicates that it was deposited under dysoxic to anoxic conditions with minimal bioturbation. Under these conditions fecal

material and carcasses settled on the bottom where they were shielded from the actions of scavengers or bioturbators.

The source of phosphate for the Winneshiek bromalites may be the same as that for the cololites associated with the arthropod *Leanchoilia* from the Cambrian Burgess Shale. Butterfield (2002) observed that these cololites from the Burgess Shale also contain phosphatic microspherules and interpreted them as intracellular structures such as enzyme granules, lipid storage vesicles, and mineral spherites. The phosphatic microspherules in Winneshiek bromalites do not seem to have an organic vesicle and the best-preserved ones are characterized by thin concentric layers (Fig. 10M–N), analogous to phosphatic granules generated by many living arthropods (Becker et al. 1974; Brown 1982) and other taxa (Burton 1972; Howard et al. 1981). In modern arthropods, such as decapod crustaceans, mineralized granules are commonly stored within the tissues lining the digestive organs (Simkiss and Taylor 1994). These structures serve as a storage site for calcium ions used in constructing cuticle (Becker et al. 1974; Corrêa et al. 2002) as well as a means of sequestering toxic metals (Mason and Nott 1981; Pullen and Rainbow 1991). The lining of digestive organs containing these granules is regularly shed and expelled in fecal matter and granules can be present in large quantities within fecal pellets (Corrêa et al. 2002; Simkiss and Taylor 1994). Thus, mineralized granules could have provided an important internal source of calcium phosphate that facilitated the phosphatization of Winneshiek bromalites as well as explaining their microspherule-dominated microstructure. The best-preserved microspherules (Fig. 10M–N), in particular, exhibit an internal structure composed of concentric layers of nanocrystalline phosphate, which resembles the internal structure of mineralized granules produced in the midgut of modern decapod crustaceans, e.g., figs. 5–6 in Becker et al. (1974) and figs. 4–6 in Loret and Devos (1992). Many microspherules are poorly preserved, with cavities

resulting from dissolution and filled with amorphous organic carbon (Fig. 10H–L), thus releasing phosphate for bromalite mineralization. Phosphate enrichment must also have been derived from other sources, including prey items such as arthropods and conodonts.

The presence of microbes in fecal material prior to phosphatization provides an alternative to the mineralized granule interpretation of the microspherules. In contrast to Butterfield (2002), Lamboy et al. (1994) and Pesquero et al. (2014) interpreted spherical structures in coprolites as molds of bacteria, suggesting a different link between microstructure and taphonomic processes. However, the best-preserved microspherules consist of fully concentric layers (Fig. 10M–N), suggesting outward accretionary growth, which is consistent with mineralized granules but inconsistent with hollow coccoidal bacteria. Furthermore, among the many thousands of Winneshiek microspherules observed in this study, none of them have a coherent organic wall and few of them show evidence of deflation and collapse; instead, the organic layers in Winneshiek microspherules are often C-shaped, uneven in thickness, and intragranular in form (Fig. 10H–L). This is in sharp contrast to permineralized coccoidal bacteria or organic-walled microfossils, which typically have a coherent cell wall with stable thickness and various degrees of deformation and deflation (e.g., see phosphatized organic-walled microfossils illustrated in fig. 5F of Zabini et al. 2012). Thus, we favor a phosphatic granule interpretation over a coccoidal bacterium interpretation for the Winneshiek microspherules.

Building upon petrographic observations and the phosphatic granule interpretation described above, Figure 11 illustrates a potential paragenetic and taphonomic sequence to account for the morphological variation of Winneshiek microspherules. In this model, the solid core with fully concentric layers (e.g., Fig. 10M–N) is regarded as the primary structure (Fig. 11A). Based on modern analogs, the core probably consisted of amorphous phosphate, which is highly soluble.

The dissolution of the primary core provides phosphate to drive the precipitation of carbonate fluorapatite, which is more stable. For example, nanocrystalline carbonate fluorapatite crystals can be nucleated on the surface of the core (Fig. 11B). This is followed by the outward growth of carbonate fluorapatite crystals to form an outer envelope (Fig. 11C), which is expected to have a relatively smooth inner surface (defined by the outer surface of the core) and an irregular outer surface (defined by crystal terminations). Following the initial dissolution of the core, the space between the envelope and the remaining core can be filled with the precipitation of carbonate fluorapatite (Fig. 11C–D), erasing the primary concentric structure. If dissolution of the core proceeds to completion, then the entire core can be cast by carbonate fluorapatite crystals (e.g., Fig. 10G). Often times, however, the core is partially conserved (Fig. 11E) or incompletely cast by carbonate fluorapatite crystals (Fig. 11F), leaving a C-shaped void or a central void to be filled with amorphous organic carbon. The precipitation of carbonate fluorapatite in the inter-microspherule space finally cements the microspherules (Fig. 11D–F), leading to a phosphatized bromalite.

The Tracemaker

Determining the identity of a bromalite tracemaker is difficult except in cases where specimens are found in direct association with body fossils (Hunt 1992). Exceptions are ichnotaxa such as the microcoprolites *Favreina* and *Palaxius*, which are sufficiently distinct in morphology to be recognized as the products of decapod crustaceans (Peckmann et al. 2007; Scoffin 1973). The range of morphologies exhibited by the Winneshiek bromalites—straight or meandering cylindrical structures with surface textures ranging from smooth to corrugated—resemble fecal pellets that can be produced by a wide variety of taxa (Kraeuter and Haven 1970).

Several features of the Winneshiek bromalites are consistent with an arthropod origin. Densely packed phosphatic granules similar in size and shape to the microspherules occur in the midgut of a variety of arthropod taxa (Hopkin 1990; Hopkin and Nott 1979; Simkiss and Taylor 1994). Three dimensionally phosphatized structures broadly similar to the Winneshiek bromalites have been found directly associated with arthropod body fossils from the Burgess Shale (Butterfield 2002) and Sirius Passet (Peel 2017). Thus, the eurypterid or other large arthropods of the Winneshiek Lagerstätte are plausible tracemakers of the Winneshiek bromalites.

A subset of the Winneshiek bromalites exhibit a concentrically layered internal structure (Fig. 3H). This feature is characteristic of the coprolites of animals with a valvular intestinal tract, a feature frequently found in chordates (Jain 1983; McAllister 1985; Williams 1972). The valvular intestine refers to a coiled epithelial flap that is present within the intestinal tract. This flap increases the surface area of the intestine and thus its absorptive efficiency. Feces passing through the coiled flap are left with an internal structure that resembles a rolled-up scroll, with layers of mucus between the concentric layers of fecal material (Gilmore 1992). Gilmore (1992) identified these types of coprolites in association with agnathans from the Silurian of Ireland. Importantly, it has been proposed that spiral coprolites from the Ordovician Soom Shale, which are broadly similar to some Winneshiek bromalites, may have been produced by conodonts (Aldridge et al. 2006).

Among the three candidate trace makers identified above, agnathan fishes are the rarest fossils in the Winneshiek Shale (Liu et al. 2006). Conodonts and eurypterids, which are more abundant, are more plausible tracemakers of the Winneshiek bromalites. Conodont apparatuses and elements from the Winneshiek Shale demonstrate that some conodont taxa reached large sizes, with apparatuses spanning more than a centimeter (Liu et al. 2017). Conodont animals have been

proposed as trace makers of bromalites from the Soom Shale where large conodonts also occur (Aldridge et al. 2006). Eurypterids (Lamsdell et al. 2015b) have also been proposed as potential bromalite trace makers in the Soom Shale (Aldridge et al. 2006). An ultimate test of these hypotheses rests on the discovery of body fossils associated with Winneshiek bromalites. Regardless of the identities of the tracemakers, the presence of conodont elements within some Winneshiek bromalites is unequivocal evidence for predation during the Great Ordovician Biodiversification Event (GOBE) and, if conodont animals were also the tracemakers, these animals could be both predator and prey.

Conclusion

Three dimensionally preserved bromalites from the Middle Ordovician Winneshiek Lagerstätte in northeastern Iowa are a significant component of the assemblage, being the fourth most abundant category of specimens. Our examination of the composition, external and internal morphologies, and microstructures of these fossils confirms their bromalitic nature. Circumstantial evidence (e.g., lack of body fossil preservation in association with bromalites preserved as carbonaceous compressions) also suggests that the Winneshiek bromalites are more likely to be coprolites than cololites. The majority of Winneshiek bromalites were phosphatized, a common mode of preservation for bromalites, with a smaller number preserved as carbonaceous compressions. The identity of the tracemaker remains uncertain due to the absence of body fossils in direct association. A suite of arthropods, most likely eurypterids, as well as conodonts and fishes are potential tracemakers. The presence of conodont inclusions in some bromalites provides evidence for predation in the Winneshiek assemblage.

Figure Captions

Figure 3.1. Locality maps. (A) Iowa map showing the location of the Decorah impact structure. (B) Map of Decorah, Iowa, showing the outline of the impact structure.

Figure 3.2. Reflected light images (A, B), BSE images (C, D), and elemental maps (E–H) of longitudinally sectioned vermiform structures. Dashed lines in (A) and (B) mark approximate location of sectional views shown in (C, E, G) and (D, F, H), respectively. (A) SUI 145137; (B) SUI 145138. Scale bars equal 2 mm.

Figure 3.3. Reflected light images (A–M) and BSE image (N) of bromalites. (A) Specimen exhibiting a tapered neck feature, SUI 145144 (WL61). (B) Possible additional specimen with a tapered neck structure, SUI 145145 (WS18-264). (C–D) Specimens exhibiting a coiled morphology. (C) SUI 145146 (WS11-434); (D) 145147 (WL140). (E) Specimen with irregularly folded structures, SUI 145148 (WS16-541). (F) Specimen preserved as a carbonaceous compression, SUI 145149 (WL55). (G–H) Specimens in transverse cross-section. (G) SUI 145150 (WL90); (H) SUI 145151 (WS10-242). (I) Specimen showing apparent branching structure that could be a taphonomic artifact, SUI 145152 (WL53). (J–K) Partially pyritized bromalites. (J) SUI 145153 (WS13-503); (K) SUI 145154 (WS14-104). (L) Bromalite that is partially phosphatized (white arrow) and partially preserved as a carbonaceous compression (black arrow), SUI 145173. (M) Rod-shaped bromalite, SUI 145140. (N) BSE image of a partial longitudinal cross-section of (M), showing transverse ‘segmentation’ structures. The specimen is replicated by phosphate (darker color; white arrow) and sphalerite (brighter color; black arrow).

Figure 3.4. Reflected light images of bromalites. (A–C) Densely corrugated rod-like specimens. (A) SUI 145155 (WL8); (B) SUI 145156 (WS14-417); (C) SUI 145157 (WS14-559). (D–E) Densely corrugated and compressed specimens. (D) SUI 145158 (WS14-549); (E) SUI 145159 (WS14-519). (F–G) Unsculpted and compressed specimens. (F) SUI 145160 (WL115); (G) SUI 145161 (WL119). (H–J) Unsculpted rod-like specimens. (H) SUI 145162 (WS9-148); (I) SUI 145163 (WS14-548); (J) SUI 145164 (WL31). (K–N) Specimens defined by concentration of quartz sand. (K) SUI 145165 (WL99); (L) SUI 145166 (WL182); (M) SUI 145167 (WS10-200); (N) SUI 14568 (WS14-229). (O–Q) Specimen exhibiting morphological variation along its length and containing conodont elements. Black and red rectangles in (O) marks magnified views shown in (P, counterpart) and (Q), respectively. Part of the specimen is somewhat three dimensionally preserved and shows transverse wrinkles or striations (arrow in P) characteristic of phosphatized specimens analyzed in this study, and part of the specimen is preserved as carbonaceous compression with conodont inclusions (arrows in Q). SUI 145169(WL95). Black scale bars equal 5 mm, white scale bars equal 1 mm.

Figure 3.5. Reflected light images of bromalites exhibiting evidence of deformation or liquefaction. (A) SUI 145170 (WS14-310); (B) SUI 145171 (WS11-472); (C) 145172 (WL28). All scale bars equal 1 cm.

Figure 3.6. Transmitted light photomicrographs of microspherules in thin section. (A) Transverse cross section of a vermiform fossil. (B–E) Successive magnifications showing details of microspherules. Magnified areas are marked with labeled rectangles. Arrows highlight microspherules where the outer edge of the envelope is irregular. This specimen is also illustrated in Fig. 7 and Fig. 9A (top specimen). SUI 145141.

Figure 3.7. Reflected light image (A) and BSE images (B–D) of specimen with densely packed microspherules. White dashed line in (A) indicates approximately where the specimen was cut for thin section preparation. Rectangles in (B) and (C) mark areas magnified in (C) and (D), respectively. The specimen is also illustrated in Fig. 6 and Fig. 9A (top specimen). SUI 145141.

Figure 3.8. Reflected light image (A) and BSE images (B–D) of specimen with densely packed microspherules. White dashed line in lower right of (A) indicates where the specimen was cut for thin section preparation. Rectangles in (B) and (C) mark areas magnified in (C) and (D), respectively. SUI 145142.

Figure 3.9. Transmitted light microscopic image (A) and BSE (B–D) images of specimen with densely packed microspherules. (A) Two specimens: top specimen is also illustrated in Figs. 6–7, and bottom specimen (rectangle) is shown here in successive magnifications. Rectangles in (A), (B), and (C) mark areas magnified in (B), (C), and (D), respectively. SUI 145143.

Figure 3.10. SEM images of microspherules in specimen SUI 145143 (also illustrated in Fig. 9, bottom specimen). (A) Transverse section of a bromalite exposed during thin section preparation. Labeled boxes in (A) mark areas magnified in (B–F). Labeled boxes in (B–F) mark individual microspherules shown in (G–N). Scale bars in (G–N) equal 2 µm. Microspherules in (K–L) were imaged in secondary electron mode, while all other SEM pictures were taken in BSE mode.

Figure 3.11. Schematic drawing showing paragenetic sequence of secondary mineral precipitation. Illustration assumes biological granule precursor of microspheres. (A) Precursor granules with concentric layers. (B) Initial nucleation of micro- and nanocrystalline fluorapatite on precursor granules. (C) Nucleation and growth of outer envelope. (D–E) Nucleation and growth of micro- and nanocrystalline fluorapatite in inter-microspherule space, and dissolution of precursor core. (F) Complete disappearance of precursor core, and complete infilling of inter-microspherule space.

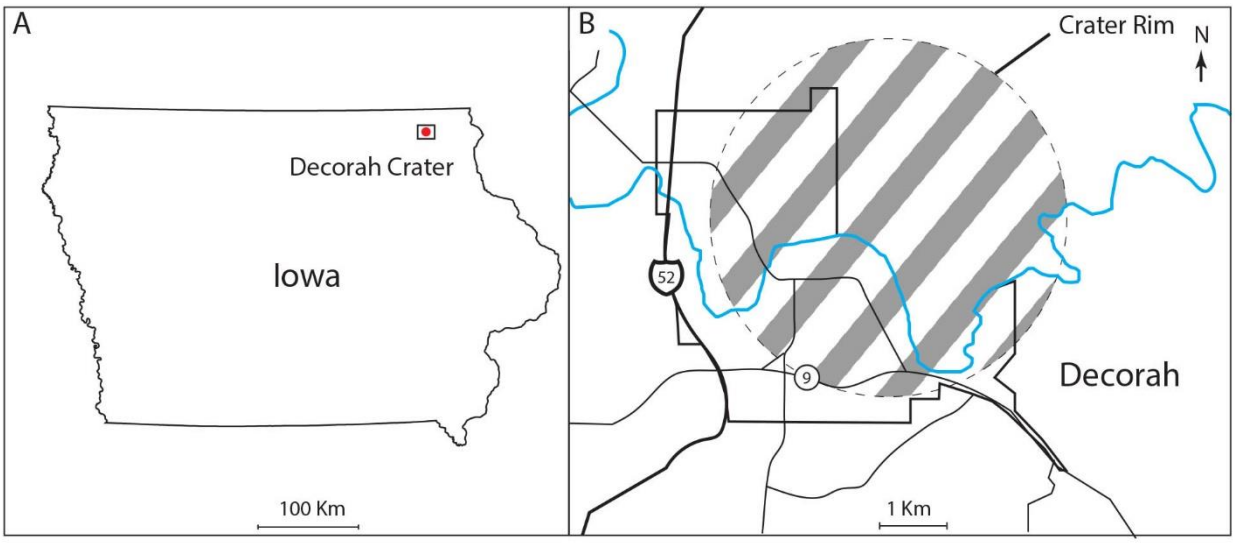

Figure 3.1

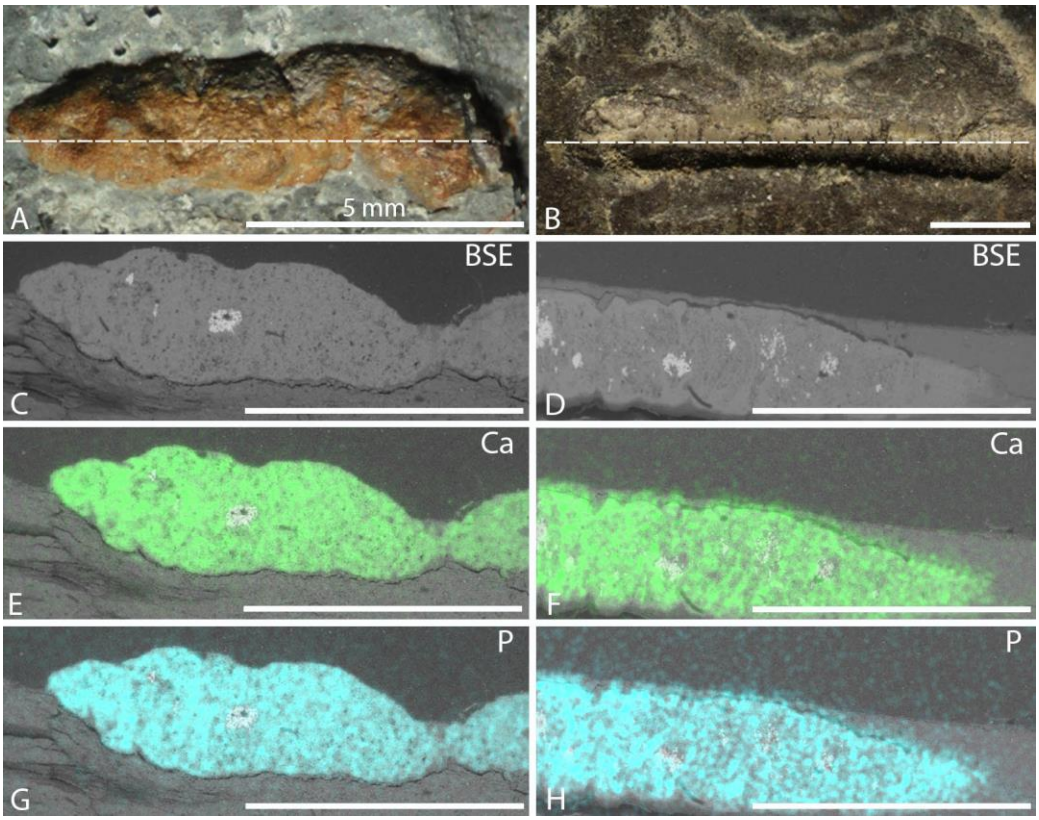

Figure 3.2

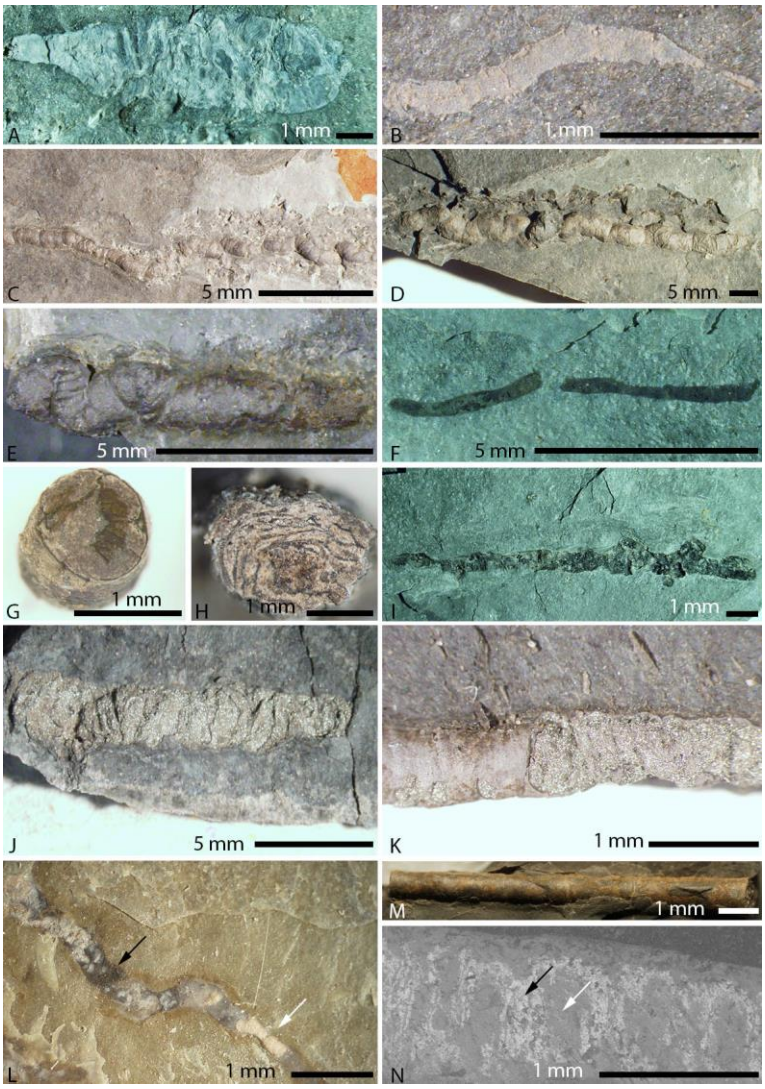
A
1 mm
B
1 mm
C
5 mm
D
5 mm
E
5 mm
F
5 mm
G
1 mm
H
1 mm
I
1 mm
J
5 mm
K
1 mm
M
1 mm
L
1 mm
N
1 mm

Figure 3.3

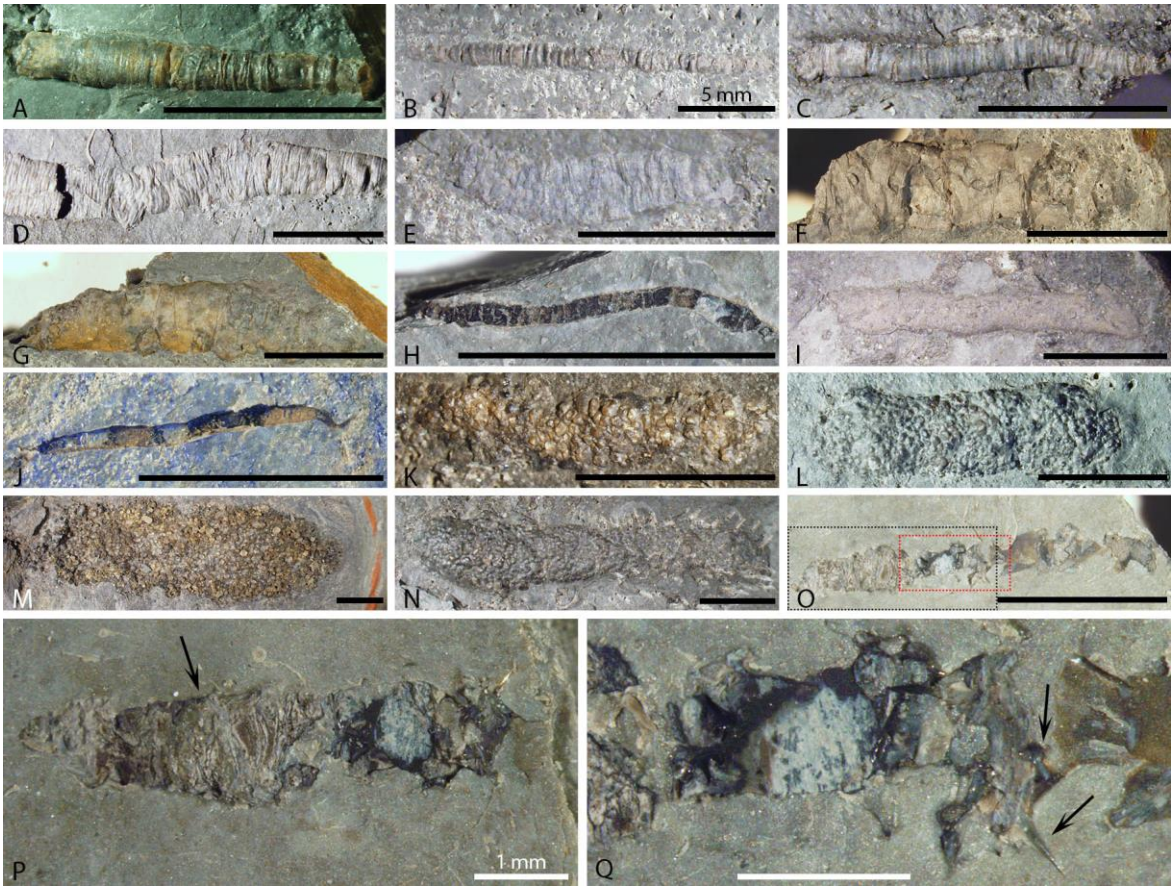

Figure 3.4

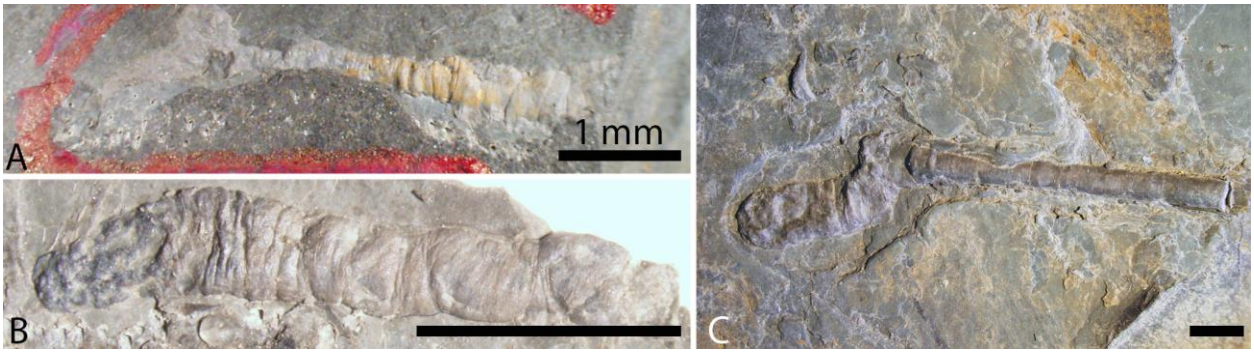

Figure 3.5

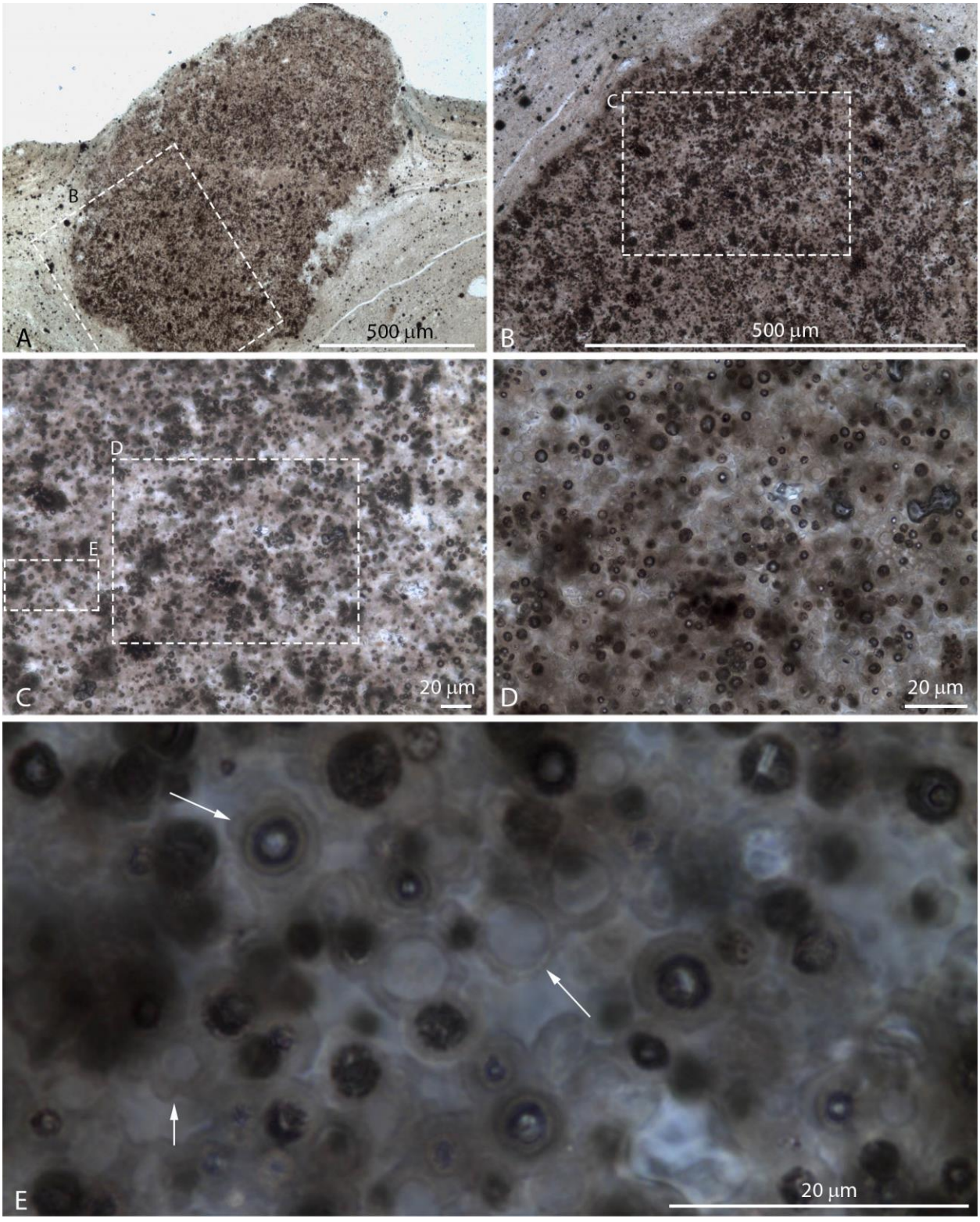

Figure 3.6

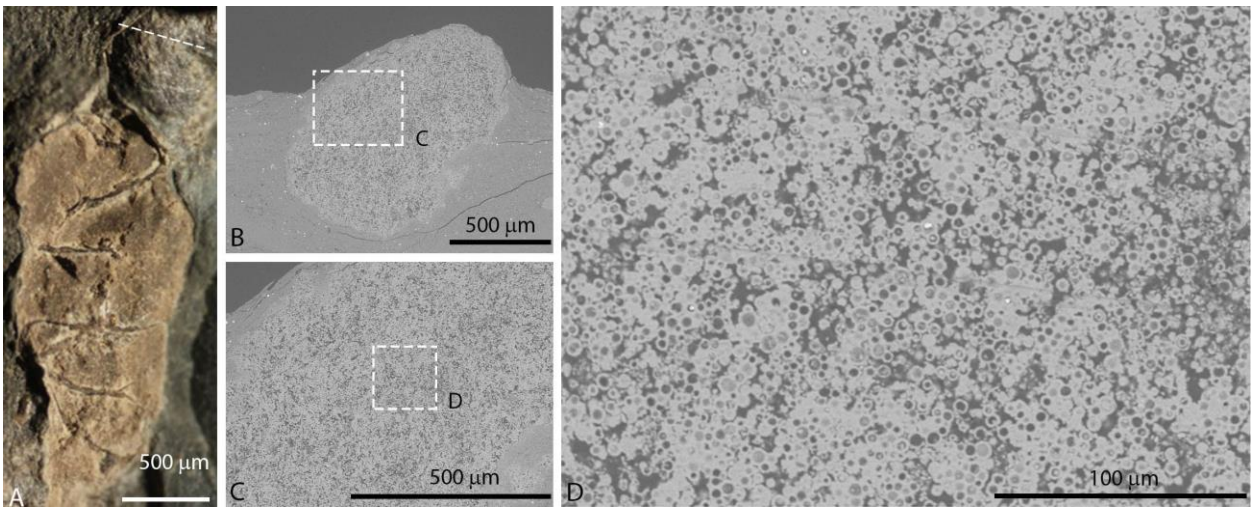

Figure 3.7

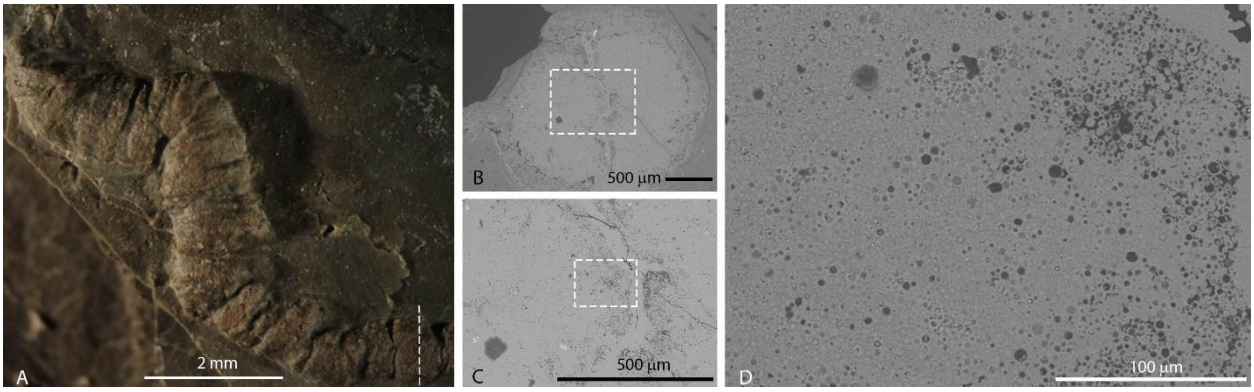

Figure 3.8

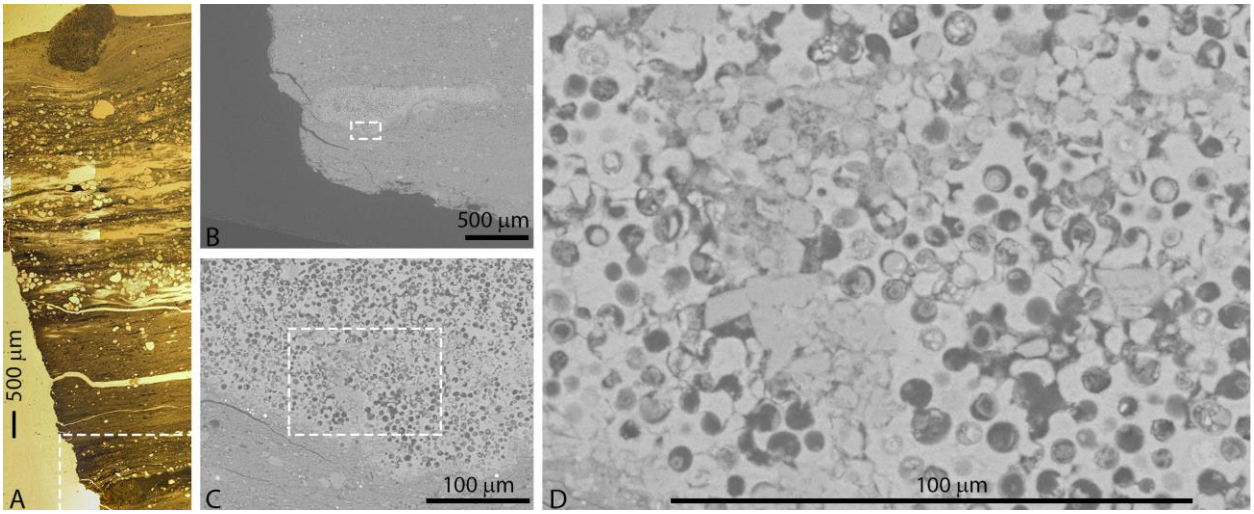

Figure 3.9

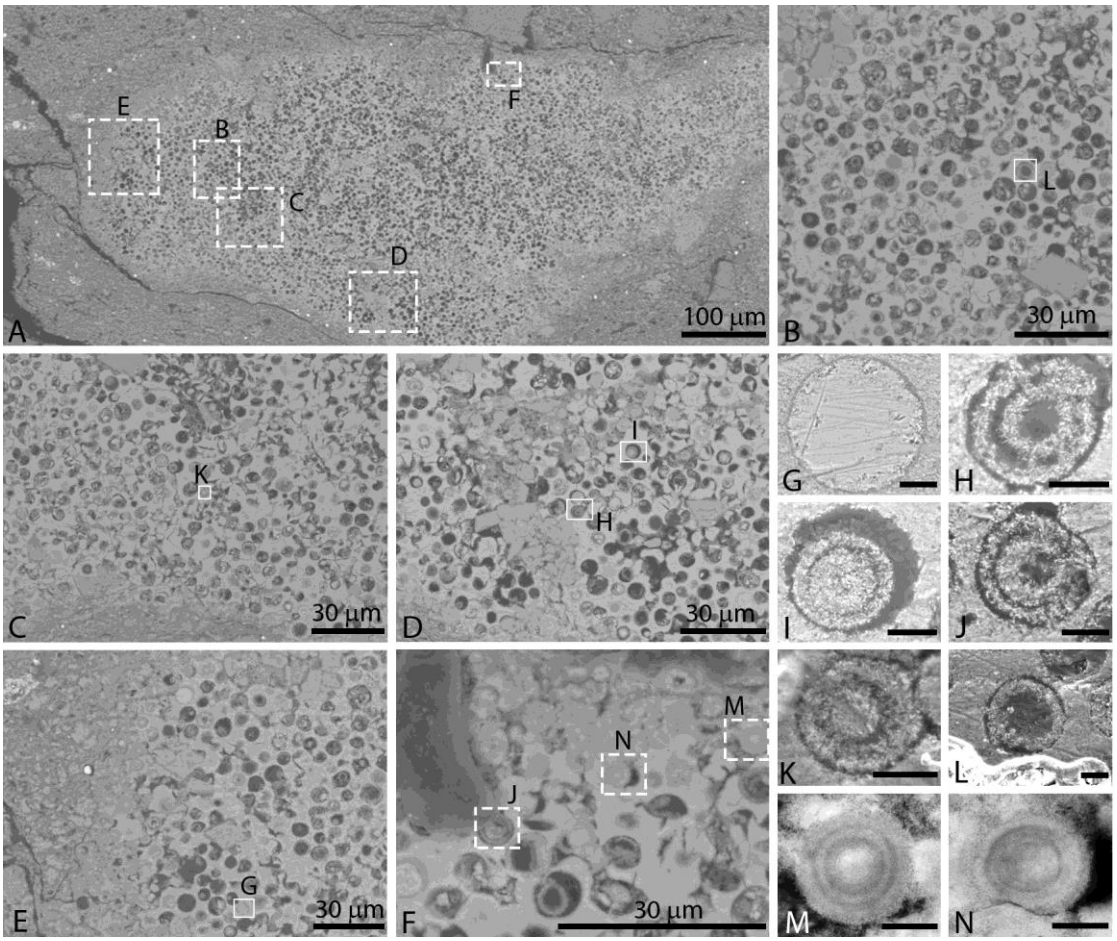
A
E
B
C
D
F
100 µm
B
L
30 µm
C
K
30 µm
D
I
H
30 µm
G
H
I
J
E
G
30 µm
F
M
N
J
30 µm
K
L
M
N

Figure 3.10

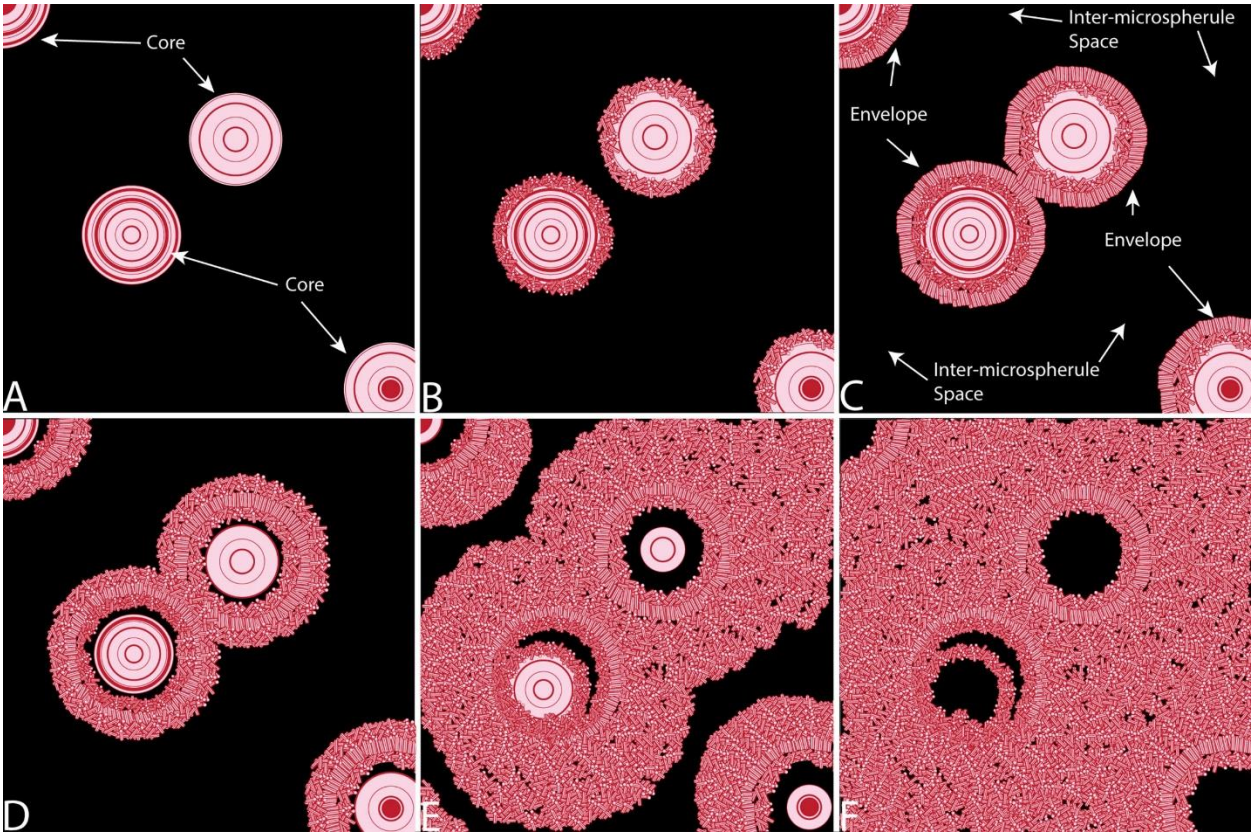
Core
Core
A
B
Inter-microspherule Space
Envelope
Envelope
Inter-microspherule Space
C
D
E
F

Figure 3.11

Chapter 4 New biostratigraphic and chemostratigraphic data from the Ediacaran Doushantuo Formation in intra-shelf and upper slope facies of the Yangtze platform: Implications for biozonation of acanthomorphic acritarchs in South China

Abstract

Carbon isotopic and microfossil records of the Doushantuo Formation in South China provide a valuable window onto major perturbations of the Ediacaran carbon cycle and the evolution of morphologically complex acanthomorphic acritarchs. Both records exhibit significant geographic heterogeneity related to environmental, taphonomic, and diagenetic variations. Absolute $\delta^{13}C_{carb}$ values vary by as much as 10‰ between sections of the Doushantuo Formation. The geographic and stratigraphic distribution of microfossils in the Doushantuo Formation is controlled by the occurrence of early diagenetic cherts and phosphorites that preserve microfossils. Early diagenetic cherts of the Doushantuo Formation have been investigated extensively at intra-shelf sections in the Huangling anticline but have been poorly documented elsewhere in South China. Here we present new petrographic and micropaleontological data from three Doushantuo sections to the south of the Huangling anticline, including the Wangzishi and Huangjiaping sections representing intra-shelf settings, as well as the Siduping section representing an upper slope setting. We also present $\delta^{13}C_{carb}$ data from Wangzishi. Petrographic observations indicate that some chert nodules were formed in situ, whereas others were reworked and probably transported from the outer shelf along with olistostromes. Integrated lithostratigraphic and chemostratigraphic correlations suggest that the fossiliferous intervals at the three studied sections belong to the lower Doushantuo Formation. The new micropaleontological data extend the geographic range of Ediacaran acanthomorphs and suggest that elements of the

Tanarium conoideum–Hocosphaeridium scaberfacium–Hocosphaeridium anozos **biozone recognized in the upper Doushantuo Formation in the Huangling anticline, specifically *Hocosphaeridium anozos* and *Urasphaera nupta,* are present in the lower Doushantuo Formation at the Siduping section. The data suggest that the first appearance of *Hocosphaeridium anozos* may be in the $\delta^{13}C_{carb}$ chemostratigraphic feature EP1 and it is necessary to revise the acritarch biozonation developed in the Yangtze Gorges area. This study highlights the importance of integrating $\delta^{13}C_{carb}$ chemostratigraphic and acritarch biostratigraphic data from multiple facies to develop Ediacaran acanthomorph biozonation in South China and beyond.**

Introduction

The Doushantuo Formation is exposed in outcrops scattered across hundreds of kilometers in South China and has yielded one of the richest paleobiological and geochemical records for the lower-middle Ediacaran System in the world (Jiang et al. 2011). Two components of the Doushantuo record in particular have received significant attention: carbon isotope data from carbonates and exceptionally preserved microfossils from early diagenetic cherts and phosphorites. The carbon isotope record of the Doushantuo Formation shows three negative $\delta^{13}C_{carb}$ excursions, the most pronounced of which has been suggested to correlate with the globally recognized Shuram excursion (McFadden et al. 2008; Zhou and Xiao 2007; Zhu et al. 2013), one of the largest negative $\delta^{13}C_{carb}$ excursion in Earth history (Grotzinger et al. 2011). Along with early diagenetic phosphorites (Xiao et al. 2014a), early diagenetic cherts are one of two types of Doushantuo lithologies that have yielded exceptionally preserved microfossils (Muscente et al. 2015). Thus, integrated carbon isotopic and micropaleontological data from the Doushantuo Formation and other Ediacaran successions are essential to improve the stratigraphic correlation and subdivision of the Ediacaran System (Xiao et al. 2016).

A notable feature of both the $\delta^{13}C_{carb}$ and silicified microfossil records of the Doushantuo Formation is their significant geographic variability. Although $\delta^{13}C_{carb}$ chemostratigraphic patterns are similar among different sections of the Doushantuo Formation, their absolute values sometimes vary by as much as 10‰ across the Yangtze Block (Jiang et al. 2007; Wang et al. 2017a; Wang et al. 2016). Similarly, the occurrence of early diagenetic and fossiliferous cherts is also geographically restricted (Muscente et al. 2015) and taphonomically variable (Zhou et al. 2007). Thus, it is critical to explore as many Doushantuo sections as possible in order to document the geographic heterogeneity of the $\delta^{13}C_{carb}$ and silicified microfossil records.

Previous studies of Doushantuo $\delta^{13}C_{carb}$ and silicified microfossils have been largely limited to sections in the Yangtze Gorges area around the southern part of the Huangling anticline in the Yangtze Gorges area (Fig. 1). These sections were deposited in an intra-shelf lagoon (Jiang et al. 2011), and while they may be endowed with favorable taphonomic conditions, bio- and chemostratigraphic models developed in the Yangtze Gorges area need to be tested at other sections beyond the Huangling anticline and in outer shelf to slope environments. At present, this task is challenging because $\delta^{13}C_{carb}$ and microfossil data from outer shelf and slope sections are limited, and integrated bio- and chemostratigraphic studies in these sections are few. For example, with a few exceptions (e.g., Ouyang et al. 2017; Yin 1999), fossiliferous chert nodules of the Doushantuo Formation are known almost exclusively in intra-shelf sections around the Huangling anticline (Liu et al. 2014b; Liu et al. 2013), and slope and basinal sections have not been thoroughly explored for silicified microfossils. Similarly, investigation of $\delta^{13}C_{carb}$ chemostratigraphy has primarily been focused on intra-shelf sections (Ader et al. 2009; Cui et al. 2015; Jiang et al. 2011; McFadden et al. 2008; Zhu et al. 2013), with several exceptions (Jiang et al. 2007; Wang et al. 2017a; Wang et al. 2016). Importantly, integrated bio- and chemostratigraphic analyses of the

Doushantuo Formation have so far been limited to the Yangtze Gorges area (e.g., Liu et al. 2014b; Liu et al. 2013; McFadden et al. 2008; McFadden et al. 2009), severely hampering our capability to develop a fuller understanding of both records and to evaluate chemostratigraphic and biostratigraphic markers for regional and global stratigraphic correlation.

Here we present new petrographic, carbon isotopic, and micropaleontological data from three sections outside the Huangling anticline to address some of the geographic gaps in the records of silicified microfossils and $\delta^{13}C_{carb}$ in the Doushantuo Formation. The three sections include the intra-shelf Wangzishi and Huangjiaping sections to the south of the Huangling anticline, as well as the upper-slope Siduping section (Fig. 1B). Petrographic observations indicate that early diagenetic cherts at these sections are taphonomically similar to those around the Huangling anticline (Xiao et al. 2010), although some cherts at the Siduping section were reworked and probably transported from elsewhere. The occurrence of silicified microfossils at these sections, and particularly the occurrence of acanthomorphic acritarchs in early diagenetic cherts at the Siduping section, extend the silicification taphonomic window to the upper slope setting in the Yangtze Block (Ouyang et al. 2017). Integrated with new and previously published $\delta^{13}C_{carb}$ data from the Wangzishi and Siduping sections, we are able to improve our understanding of the $\delta^{13}C_{carb}$ and exceptionally preserved microfossil records within the Doushantuo Formation across the Yangtze platform, thus contributing to Ediacaran stratigraphic correlation in South China and beyond.

Background

Lithostratigraphy and facies variation of the Doushantuo Formation

The Doushantuo Formation was deposited in a passive continental margin setting on the Yangtze Block between 635 and 551 million years ago (Condon et al. 2005). It overlies the uppermost Cryogenian glacial diamictite of the Nantuo Formation, and is overlain by the upper Ediacaran Dengying Formation in the northwestern portion of the Yangtze Block and by the Liuchapo Formation in the southeast (Jiang et al. 2011). In its type area in the Yangtze Gorges, the Doushantuo Formation can be divided into four lithologic members (McFadden et al. 2008; McFadden et al. 2009; Zhao et al. 1988). Member I consists of an approximately 4-meter-thick cap carbonate. Member II is 80–120 meters in thickness and consists of interbedded black shales, dolostones, and muddy dolostones. Chert nodules occur abundantly in this member and contain exceptionally preserved microfossils, including acanthomorphic acritarchs (Liu et al. 2014a; Liu et al. 2013; McFadden et al. 2009; Xiao 2004). Member III is 40–60 meters in thickness and consists of medium bedded dolostone and sometimes interbedded limestone and silty dolostone. This member also contains fossiliferous chert nodules and banded cherts (McFadden et al. 2009; Yin et al. 2009; Zhou et al. 2007). At the well-studied Jiulongwan section, Member IV consists of ~10 meters of organic-rich black shale with large carbonate concretions. At some sections in the western part of the Huangling anticline, Member III is overlain by two black shales separated by a dolostone; Zhou et al. (2017) correlate these three units with Member IV, whereas An et al. (2015) correlate only the lower black shale with Member IV. These alternative correlations highlight the fact that the Doushantuo Formation exhibits significant lithofacies variation and that lithostratigraphic correlation is not straightforward (Xiao et al. 2012).

To account for the lithofacies variation, Jiang et al. (2011) proposed that mixed carbonate and fine-grained siliciclastic sediments of the Doushantuo Formation in the Huangling anticline

were deposited in a restricted intra-shelf lagoon, whereas slumped sediments and predominantly fine-grained siliciclastic sediments were deposited in slope and basinal environments to the southeast (Fig. 1B). The lowermost Doushantuo Formation, as represented by Member I and the lowermost Member II, shows relatively little lithofacies variation, suggesting deposition from an open shelf during postglacial transgression. Later in the depositional history of the Doushantuo Formation, however, this open shelf configuration evolved into a rimmed platform, with the development of a shelf margin shoal complex (Jiang et al. 2011). The shelf rim runs in an approximately northeast-southwest direction (modern day) from northwestern Hunan to northeastern-central Guizhou. A restricted intra-shelf lagoon was located to the northwest of this rim, with the slope and basinal settings to the southeast on the ocean side of the platform margin.

The three sections sampled in this study—the Wangzishi, Haungjiaping, and Siduping sections (Fig. 1B) were deposited in two widely separated regions of the Yangtze Block. The Wangzishi and Huangjiaping sections are located to the south of the Huangling anticline and were deposited in the intra-shelf lagoon. The stratigraphy in this area is broadly similar to other sections on the southern end of the Huangling anticline (e.g., the Jiulongwan section) and the four member lithostratigraphic division developed on the southern end of the Huangling anticline can also be applied in this area. Significant portions of the Doushantuo Formation are covered at both the Wangzishi and Huangjiaping sections and the exposed Doushantuo Formation is primarily limited to Member II. As a result, our measured sections at both localities are focused on Member II (Figs. 2–3). The Siduping section was deposited in an upper slope setting (Wang et al. 2016). The occurrence of olistostromes at multiple horizons (Fig. 4) indicates that Siduping sediments were supplied in part via downslope transport from the carbonate factory near the shelf-slope break.

Syndepositional folds and slump blocks in these olistostrome beds demonstrate sediment mobilization and downslope transport before lithification (Vernhet et al. 2006; Wang et al. 2016).

Acanthomorph biozonation of the Doushantuo Formation

Two acritarch biozones have been recognized in the Doushantuo Formation around the Huangling anticline (Liu et al. 2014b; Liu et al. 2013; McFadden et al. 2009; Xiao et al. 2014b). The lower biozone (i.e., the *Tianzhushania spinosa* biozone) is dominated by *Tianzhushania spinosa* and has been recognized in Member II (Liu et al. 2013; McFadden et al. 2009). The base of the upper biozone (i.e., the *Tanarium conoideum–Hocosphaeridium scaberfacium–Hocosphaeridium anozos* biozone) is defined by the first occurrence of *Hocosphaeridium anozos* (Xiao et al. 2014b). In the Yangtze Gorges area, these two biozones are separated from each other by a barren interval characterized by the negative $\delta^{13}C_{carb}$ excursion EN2 (Liu et al. 2013). It has been argued that the stratigraphic ranges of *Tianzhushania spinosa* and *Hocosphaeridium anozos* do not overlap, with the former only in the lower biozone and the latter only in the upper (Liu et al. 2013). However, early diagenetic phosphorites from the Weng'an area contain elements of both the upper and lower biozones including *Tianzhushania spinosa* and *Hocosphaeridium anozos* (Xiao et al. 2014b), suggesting that the stratigraphic ranges of these two taxa may overlap and that there may exist a transitional assemblage between the lower and upper biozones recognized in the Yangtze Gorges area. This suggestion is difficult to evaluate in the Yangtze Gorges area where the boundary between these two biozones falls within a barren interval devoid of early diagenetic cherts. Thus, it is imperative to investigate other Ediacaran sections beyond the Yangtze Gorges area to complement biostratigraphic data from the Huangling anticline.

$\delta^{13}C_{carb}$ chemostratigraphy of the Doushantuo Formation

Three negative $\delta^{13}C_{carb}$ excursions and two intervening positive excursions have been consistently recognized in the Doushantuo Formation around the Huangling anticline (Jiang et al. 2011; McFadden et al. 2008; Wang et al. 2017c; Zhou and Xiao 2007; Zhu et al. 2013; Zhu et al. 2007). The lowermost negative excursion, termed EN1, occurs within the cap carbonate, which contains microfabrics with extremely negative $\delta^{13}C_{carb}$ values characteristic of methane signatures at the Jiulongwan and Wangzishi sections (Jiang et al. 2003; Wang et al. 2008; Wang et al. 2017b). EN1 is followed by a positive excursion termed EP1 in Member II. The second negative excursion, EN2, occurs near the Member II/III boundary in the Yangtze Gorges area. Succeeding EN2 is a positive excursion (EP2) in the lower Member III. The third and largest negative excursion, EN3, occurs within upper Member III and possibly Member IV, and has been suggested as being correlative with the Shuram excursion (McFadden et al. 2008). Although additional excursions have been identified at some sections (Tahata et al. 2013; Zhu et al. 2013), these are not consistent chemostratigraphic features in the Yangtze Gorges area and may represent diagenetic noises (Xiao et al. 2012).

Methods

The three sections at Wangzishi (30°32'34.00"N, 111°9'16.20"E), Huangjiaping (30°32'13.26"N, 111°10'2.88"E), and Siduping (28°54'48.90"N, 110°27'2.10"E) were measured and sampled for chert nodules during several field trips in 2007, 2008, 2011, and 2013. As the main goal of this study was to obtain biostratigraphic data from the upper slope setting, the Siduping section was targeted for high-resolution sampling, and supplementary samples were collected at the Wangzishi and Huangjiaping sections representing the intra-shelf setting outside the Huangling anticline. Chert nodules were collected for micropaleontological analysis and

carbonate samples for $\delta^{13}C_{carb}$ analysis. All samples were cut perpendicular to the bedding surface to prepare thin sections for petrographic and micropaleontological analyses. A total of 243 thin sections were prepared and examined, including 191 from Siduping, 27 from Wangzishi, and 25 from Huangjiaping. Thin sections were examined for microfossils and petrographic features using an Olympus BX51 microscope. Microfossils were identified, photographed, and positioned using both Olympus BX51 and England Finder coordinates (Supplementary Table S1). Size measurements were made on photographs using imageJ.

Powders of carbonate samples from the Wangzishi section were prepared for $\delta^{13}C_{carb}$ and $\delta^{18}O_{carb}$ analysis. Approximately 100 µg of powder was allowed to react with orthophosphoric acid for 150–200 s at 72 °C in a Kiel IV carbonate device connected to a MAT 253 mass spectrometer. The analytical precision was better than ± 0.05‰ for $\delta^{13}C$ and ± 0.1‰ for $\delta^{18}O$. Results are reported as per mil deviation from Vienna Pee Dee Belemnite (VPDB) (Supplementary Table S2). $\delta^{13}C_{carb}$, $\delta^{18}O_{carb}$, and $\delta^{13}C_{org}$ data of the Siduping section were previously reported in Wang et al. (2016).

Results

Petrographic observations of chert nodules

Chert nodules from the Wangzishi and Huangjiaping sections are petrographically similar to those from the Doushantuo Formation in the Yangtze Gorges area (Shen et al. 2011; Wen et al. 2016; Xiao et al. 2010). By inference, they are genetically similar, having been formed in-situ within the sediments during early diagenesis.

However, early diagenetic cherts from the Siduping section, ranging in size from ~1 mm to centimeters, consist of round or oval nodules that were formed in-situ (Fig. 5A–E) as well as

angular, subangular, and subrounded clasts that were reworked (Fig. 5F–K). In-situ chert nodules exhibit the same distinctive features observed in early diagenetic chert nodules of the Doushantuo Formation on the Huangling anticline (Xiao et al. 2010). They are composed of a silica cortex surrounded by a pyrite rim (Fig. 5C–E) and in some cases a rind of secondary calcite. They are often oblate in shape, with the long axis following sedimentary laminae (Fig. 5D). Laminae within the silica cortex are concordant and sometimes are connected laterally with sedimentary laminae in the surrounding sediment matrix (Fig. 5D). Additionally, sedimentary laminae warp above and below in-situ chert nodules (Fig. 5D). These petrographic observations indicate that in-situ chert nodules were lithified before sediment compaction and have not been reworked afterwards.

In contrast, reworked chert clasts tend to occur in olistostrome beds (Fig. 4, 5F–G), suggesting that they, like the olistostromes (Vernhet et al. 2006), were also transported via gravity flows from shelf margin and upper slope environments. Laminae within these chert clasts are discordant with sedimentary laminae in surrounding sediments (Fig. 5H–I). They are often angular in shape (Fig. 5H–I), randomly oriented (Fig. 5H–I), abraded (Fig. 5J), and sometimes embedded within reworked carbonate clasts (Fig. 5J–K). These observations suggest that the reworked chert clasts were lithified at the time of transportation. Thus, the microfossils preserved in reworked chert clasts, and in olistostrome beds in general, must have come from older strata deposited in shelf margin or upper slope environments. However, given that the reworked chert clasts contain characteristic Doushantuo acanthomorphs, they must have reworked from the Doushantuo Formation. Also, because some olistostromes show evidence of syndepositional soft-sediment deformation (Fig. 5G) (Vernhet et al. 2006), the remobilization of the olistostromes and chert clasts may have occurred prior to complete lithification of the matrix sediment. Thus, the reworked chert clasts could have come from contemporaneous or slightly older strata.

Microfossils

Stratigraphic occurrences for microfossils from the Wangzishi, Huangjiaping, and Siduping sections are shown in Figures 2–4 and Supplementary Table S1. Only a single species of acanthomorphic acritarchs, *Tianzhushania spinosa* (Fig. 6A–B), was recovered from the Wangzishi section, and no acanthomorphs were recovered from the Huangjiaping section. Several species of filamentous and coccoidal microfossils were recovered from the Wangzishi and Huangjiaping sections, including *Siphonophycus robustum*, *S. kestron*, *Myxococcoides sp*., and *Archaeophycus yunnanensis* (Fig. 6C–D).

As shown in Fig. 4, microfossils were found in both in-situ chert nodules (e.g., Fig. 7C, 7E) and reworked chert clasts (Figs. 8–9) at the Siduping section. Acanthomorph species at the Siduping section include *Appendisphaera crebra* (Fig. 9E–F), *Appendisphaera*? *hemisphaerica* (Fig. 9C–D), *Asterocapsoides sinensis* (Fig. 8F), *Ericiasphaera* sp. (Fig. 8A–B), *Hocosphaeridium anozos* (Fig. 7E–F; in in-situ chert nodules), *Mengeosphaera minima* (Fig. 7C; in in-situ chert nodules), and *Urasphaera nupta* (Fig. 8C–D). Despite the moderate diversity and abundance of acanthomorphs, the Siduping section is dominated by filamentous, coccoidal, and leiospheric microfossils, including *Siphonophycus robustum*, *S. kestron*, *S. typicum*, *Salome hubeiensis*, *Myxococcoides* sp., and *Leiosphaeridia* spp. A few specimens of multicellular algae have also been found, including a possible specimen of *Wengania* sp. (Fig. 7D). There are also a number of taxonomically unidentified specimens. Worth mentioning is an unidentified acritarch (Fig. 7A) characterized by an exceptionally large vesicle (~1,100 μm in diameter) surrounded by a thick multilaminate layer, which is reminiscent of *Tianzhushania spinosa* except for the lack of discernable processes.

Overall, the Siduping microfossils are more strongly carbonized than those in the Yangtze Gorges area, probably due to greater burial depth and higher maturity of carbonaceous material. As such, delicate structures such as extremely thin processes are poorly preserved or completely obliterated (e.g., Fig. 9B, F), making it extremely difficult to document such delicate structures in light microscopy. All Siduping microfossils were recovered from a stratigraphic interval 40–90 meters above the Nantuo-Doushantuo boundary, an interval characterized by exclusively positive $\delta^{13}C_{carb}$ values and correlated with Member II and chemostratigraphic feature EP1 in the Yangtze Gorges area (Wang et al. 2016).

$\delta^{13}C_{carb}$ data from the Wangzishi section

New $\delta^{13}C_{carb}$ data from the Doushantuo Formation at the Wangzishi section are presented in Fig. 2. Although the $\delta^{13}C_{carb}$ data from the Wangzishi section are limited to an approximately 40 meter carbonate interval in the lower Doushantuo Formation, they are useful in chemostratigraphic correlation. The $\delta^{13}C_{carb}$ values are exclusively positive, mostly between 4‰ and 8‰. Considering this carbonate unit is in the lower Doushantuo Formation and *Tianzhushania spinosa* occurs about 15 m above, the most parsimonious correlation is that the positive $\delta^{13}C_{carb}$ values at Wangzishi represent EP1 seen at Siduping (Wang et al. 2016) and in the Yangtze Gorges area (Zhou and Xiao 2007).

Discussion

Distribution of early diagenetic cherts in the Doushantuo Formation

Xiao et al. (2010) proposed that microbial sulfate reduction and the availability of reactive iron played an important role in the formation of a pyrite rim in fossiliferous chert nodules in the

Doushantuo Formation. Muscente et al. (2015) further suggested that ferruginous conditions may have been conducive in chert nodule formation in the Doushantuo Formation. If correct, this model would predict that early diagenetic chert nodules were preferentially formed in sediments bathed in ferruginous waters and in stratigraphic intervals recording ferruginous conditions, but are largely absent in lithofacies recording oxic and euxinic redox conditions.

Paleo-redox analyses indicate that, although oceanic redox conditions during the deposition of the Doushantuo Formation were characterized by temporal fluctuations (Sahoo et al. 2016; Wang et al. 2017a) and spatial heterogeneities (Li et al. 2017; Li et al. 2015), overall both the intra-shelf and the open ocean in South China were redox-stratified during the early Ediacaran Period, including a surface oxic water overlying a ferruginous deep water with a euxinic wedge (Li et al. 2010; Wang et al. 2012). Thus, the model of Muscente et al. (2015) would predict the presence of early diagenetic and fossiliferous chert nodules in upper slope facies such as the Siduping section and their absence in basinal facies that intersected the euxinic wedge. This prediction is met by the discovery of early diagenetic and fossiliferous chert nodules at Siduping and at other upper slope sections (Ouyang et al. 2017). Obviously, as in most Doushantuo sections, chert nodules at the Siduping section occur in discreet horizons, indicating that even in the most favorable settings for early diagenetic chert formation, sufficient conditions were met only episodically. Either redox conditions fluctuated episodically, or in addition to ferruginous redox conditions, other factors (such as low sedimentation rates and local supply of organic matter needed for the initial nucleation of chert nodules) may have controlled the formation of early diagenetic chert nodules.

The Siduping section is distinct from other Doushantuo sections in the occurrence of reworked chert nodules that are themselves fossiliferous and early diagenetic in origin. Our study

shows that these reworked chert nodules at Siduping were likely formed in shallower facies during early diagenesis and then transported with olistostromes to Siduping. Obviously, such reworked chert nodules do not follow the Muscente et al. (2015) model about the distribution of early diagenetic chert nodules in the Doushantuo Formation, and they complicate our efforts to establish early-middle Ediacaran acanthomorph biozones in South China.

Acanthomorph biozones of the Doushantuo Formation

The interpretation of the microfossil record of the Doushantuo Formation at the Siduping section is somewhat complicated by the fact that a significant proportion of fossiliferous chert nodules at this section were reworked and probably transported from elsewhere. The prospect of time averaging due to downslope transport is most likely to obscure the acanthomorph biostratigraphic record at Siduping. However, petrographic observation suggests that the reworked chert clasts were likely derived from contemporaneous or slightly older strata. This inference is also supported by $\delta^{13}C_{carb}$, $\delta^{18}O_{carb}$, and $\delta^{13}C_{org}$ data, which show virtually no differences between carbonate clasts and matrix in olistostrome beds, or between olistostrome beds and adjacent beds (Wang et al. 2016). Thus, although there must be some degrees of time averaging, the biostratigraphic sequence should not have been altered beyond recognition. Furthermore, because reworking can only move clasts from older to younger strata, the observed fossil occurrences at Siduping cannot be older than their true (or pre-reworking) stratigraphic occurrences.

The small number of acanthomorphic acritarchs recovered from the Siduping section precludes a rigorous quantitative description of the character of the acritarch assemblage. However, we can draw several conclusions from the data available. Acanthomorphic acritarchs recovered from the Siduping section include Doushantuo taxa from the Yangtze Gorges and

Weng'an areas (Liu et al. 2014b; Xiao et al. 2014b). Importantly, the presence of *Hocosphaeridium anozos* in in-situ chert nodules in the lower Doushantuo Formation at Siduping is significant, because this species is one of the eponymous taxa of the *Tanarium conoideum–Hocosphaeridium scaberfacium–Hocosphaeridium anozos* biozone recognized in Member III and EP2 in the Yangtze Gorges area (Liu et al. 2013). Indeed, the first appearance of this species has been proposed to define the base of the *Tanarium conoideum–Hocosphaeridium scaberfacium–Hocosphaeridium anozos* biozone in the Yangtze Gorges area (Liu et al. 2014b; Xiao et al. 2014b). However, this species has also been found in the upper Doushantuo Formation at Weng'an, where it overlaps with *Tianzhushania spinosa* (Xiao et al. 2014b). Together, these biostratigraphic data suggest that the stratigraphic ranges of *Tianzhushania spinosa* and *Hocosphaeridium anozos* do overlap, although the first appearance datum of the former clearly predates that of the latter. Furthermore, because at Siduping *Hocosphaeridium anozos* is present in strata correlated to Member II and EP1 (Wang et al. 2016), the traditional view that the *Tianzhushania spinosa* biozone is restricted to Member II and the *Tanarium conoideum–Hocosphaeridium scaberfacium–Hocosphaeridium anozos* biozone to Member III needs to be revised. This view was based on data from the Yangtze Gorges area where there is a barren interval around the Member II/III boundary and the exact boundary between the two biozones cannot be clarified (Liu et al. 2014b; Liu et al. 2013; McFadden et al. 2009; Yin et al. 2009). The new data from Siduping suggests that the *Tanarium conoideum–Hocosphaeridium scaberfacium–Hocosphaeridium anozos* biozone may start somewhere in Member II. Alternatively, if it is desirable to keep this acanthomorph biozone in Member III, then it should be redefined and a transitional biozone should be formally established to accommodate strata where *Tianzhushania spinosa* and *Hocosphaeridium anozos* co-exist, as

proposed by Xiao et al. (2012) and Xiao et al. (2014b) based on Doushantuo acanthomorph data from Weng'an.

The inference that elements in the *Tanarium conoideum–Hocosphaeridium scaberfacium–Hocosphaeridium anozos* biozone may range stratigraphically downward relative to their occurrence in the Yangtze Gorges area (Liu et al. 2014b; Liu et al. 2013) is further supported by the discovery of *Urasphaera nupta*, *Appendisphaera*? *hemispherica*, *Appendisphaera crebra*, and *Mengeosphaera minima* in the lower Doushantuo Formation at Siduping. Of these species, *Urasphaera nupta* is morphological distinct and easily recognizable. All these species have been known from the *Tanarium conoideum–Hocosphaeridium scaberfacium–Hocosphaeridium anozos* biozone in the Yangtze Gorges area (Liu et al. 2014b; Liu et al. 2013), but they may extended to Member II.

The absence of *Tianzhushania spinosa* from the Siduping assemblage is probably a matter of taphonomic or sampling failure. Because of the poor preservation due to strong carbonization, delicate structures such as the extremely thin cylindrical processes of *Tianzhushania spinosa* may have been degraded. Indeed, the taxonomically unidentified acritarch illustrated in Fig. 7A–B may be such a degraded specimen of *Tianzhushania spinosa*, given its large vesicle surrounded by a thick multilaminate layer that is characteristic of *Tianzhushania spinosa*. In addition, the sampling intensity is rather low compared with the Yangtze Gorges sections, which have been studied for decades by many research groups.

We thus predict that, unless *Tianzhushania spinosa* was ecologically restricted to the intra-shelf, it should be present in the lower Doushantuo Formation at Siduping. This prediction is based on the lithostratigraphic and $\delta^{13}C_{carb}$ chemostratigraphic correlation of the Siduping and Jiulongwan section (Wang et al. 2016), and is also supported by new $\delta^{13}C_{carb}$ and stratigraphic

occurrence of *Tianzhushania spinosa* at the Wangzishi section (Fig. 2, 6A). Collectively, these data strongly suggest that the fossiliferous interval at Siduping is equivalent to Member II and chemostratigraphically correlated to EP1 in intra-shelf sections. Thus, *Tianzhushania spinosa* is expected to be present in the lower Doushantuo Formation at Siduping, a prediction that needs to be verified with better preserved specimens in future investigations.

Microfossil and $\delta^{13}C_{carb}$ records from the Wangzishi section suggest that the sampled interval of the section correlates with the EP1 interval of the lower Doushantuo Formation in the Yangtze Gorges area. The range of $\delta^{13}C_{carb}$ values, between 4‰ and 8‰, is consistent with $\delta^{13}C_{carb}$ values observed within this interval elsewhere. The lack of biostratigraphically informative acritarchs in samples from the Huangjiaping section precludes a confident correlation for this section; however, based on lithostratigraphy it is likely that the sampled portion of this section also correlates with member II in the lower Doushantuo Formation in the Yangtze Gorges area. This inference is affirmed by Yin (1999), who has recovered *Tianzhushania spinosa* from the lower Doushantuo Formation at the Changyang section, which is only ~2 km to the south of Huangjiaping.

Conclusion

Micropaleontological and petrographic data from the Wangzishi, Huangjiaping, and Siduping sections combined with new $\delta^{13}C_{carb}$ data from the Wangzishi section and previously published $\delta^{13}C_{carb}$ data from the Siduping section provide new insights into the chemostratigraphic and biostratigraphic correlation of the Ediacaran Doushantuo Formation beyond the Huangling anticline in South China. Fossiliferous chert nodules at the Wangzishi and Huangjiaping sections that were deposited in intra-shelf settings were formed in situ and are petrographically similar to

those in other intra-shelf sections in the Huangling anticline. At the upper-slope Siduping section, both early diagenetic chert nodules formed in situ and reworked chert clasts transported via gravity flows are present, although the latter were likely remobilized from contemporaneous or slightly older strata. Acanthomorphic acritarchs were found in chert nodules at both Wangzishi and Siduping sections. *Tianzhushania spinosa* from the Wangzishi section occurs in the lower Doushantuo Formation (equivalent to Member II) above a carbonate unit characterized by $\delta^{13}C_{carb}$ values that are correlated with the $\delta^{13}C_{carb}$ feature EP1. *Hocosphaeridium anozos*, which currently defines the base of the *Tanarium conoideum–Hocosphaeridium scaberfacium–Hocosphaeridium anozos* biozone in Member III in the Yangtze Gorges area, occurs in strata equivalent to Member II and EP1 at the Shiduping section. The new occurrence of *Hocosphaeridium anozos* at Siduping suggests that the *Tanarium conoideum–Hocosphaeridium scaberfacium–Hocosphaeridium anozos* biozone may not be restricted to Member III as previously thought. Thus, this biozone may extend to Member II. Alternatively, if it is desirable to keep this acanthomorph biozone in Member III, it should be redefined and a transitional biozone should be established to accommodate strata where the stratigraphic ranges of *Tianzhushania spinosa* and *Hocosphaeridium anozos* overlap.

Acknowledgements

The research was supported by the National Science Foundation (EAR-1528553) and NASA Exobiology and Evolutionary Biology Program (NNX15AL27G). We thank Dr. Brian Romans and Dr. Benjamin Gill for useful discussion, Xiaoming Chen and Ke Pang for carbon isotope analysis.

Figure Captions

Figure 4.1. Maps showing the location of studied sections and other important sections. (A) Sketch map showing the location of the Yangtze Block. (B) Magnification of green box in (A), showing a simplified facies map of the Yangtze Block (Jiang et al. 2011). (C) Magnification of green box in (B), showing a geological map of the Huangling anticline. The Yangtze Gorges area is located in the southern tip of the Huangling anticline. Stars mark section localities.

Figure 4.2. Stratigraphic distribution of microfossils and $\delta^{13}C_{carb}$ profile at the Wangzishi section. Lithostratigraphic and chemostratigraphic correlation with the Jiulongwan section is marked on the figure (e.g., Member I and II; EP1).

Figure 4.3. Stratigraphic distribution of microfossils at the Huangjiaping section. Lithostratigraphic correlation with the Jiulongwan section is marked on the figure (e.g., Member I and II).

Figure 4.4. Stratigraphic distribution of microfossils and $\delta^{13}C_{carb}$ profile at the Siduping section. Stratigraphic column and $\delta^{13}C_{carb}$ profile are modified from Wang et al. (2016). Lithostratigraphic and chemostratigraphic correlation with the Jiulongwan section is marked on the figure (e.g., Member I–IV; EN1–3; EP1-2).

Figure 4.5. Field photographs (A–C, G–H, J–K) and thin section petrographic photomicrographs (D–F, I) of in-situ chert nodules (A–E) and reworked clasts (F–K) from the Siduping section. Red arrows highlight in-situ chert nodules, yellow arrows pyrite rim around chert nodules, white arrows reworked carbonate clasts, and blue arrows reworked chert clasts. Stratigraphic up direction on top. (A) In-situ chert bands and nodules. Rock hammer for scale. Photo 2007-0868. (B) In-situ chert nodules. Pen (15 cm) for scale. Photo 2008-2506. (C) Magnified view of rectangle in (B), showing pyrite rim. Chert nodule about 3 mm in maximum diameter. (D) Sedimentary laminae are laterally continuous into in-situ chert nodules (bottom arrow) and warp above and below chert nodules (top arrows). Thin section S41.75-1. (E) Magnification of white box in (D), showing part of pyrite rim around chert nodule. (F) Mixture of randomly oriented chert and carbonate clasts. Thin section S37.4. (G) Carbonate clasts showing soft-sediment deformation. Pen for scale. Photo 2008-2502. (H) Angular chert clasts oriented at an angle with bedding plane. Rock hammer for scale. Photo 2007-8703. (I) Randomly oriented angular chert clasts whose internal laminae are discordant with matrix sedimentary laminae. Thin section S76.4-4-2. (J–K) Chert bands within reworked carbonate clasts, showing abrasion and truncation of chert bands. Pen for scale. Photos 2008-2496 and 2008-2504.

Figure 4.6. Acanthomorphic acritarchs and other microfossils from Wangzishi and Huangjiaping. (A) *Tianzhushania spinosa*, thin section 13WZS-DST2-5C, Olympus BX 51 coordinates 110.3×19.8, England Finder coordinates J10-1. Thin section numbers and coordinates of all illustrated microfossils are given in figure captions. (B) Magnification of rectangle area in (A), showing poorly preserved processes and multilaminate layer. (C)

Archaeophycus yunnanensis, 13WZS-DST2-5C, 113.9×20.6, H13-2. (D) *Archaeophycus yunnanensis*, 13HJP-DST2-5C, 108.9×11.9, Q9-3.

Figure 4.7. Acanthomorphic acritarchs from Siduping. (A) Large and poorly preserved acritarch, possibly *Tianzhushania spinosa*, 13SDP-DST2-13, 131.7×14, M31-4. (B) Magnification of rectangle area in (A), showing multilaminate layer characteristic of *Tianzhushania spinosa*. (C) *Mengeosphaera minima*, 13SDP-DST2-32, 123.1×10.2, S23-1. (D) *Wengania* sp., S21.1, 133.3×13.9, M33-1. (E) *Hocosphaeridium anozos*, S41.6-2, 143.5×21.2, G43-1. (F) Magnification of rectangle area in (E), showing distally hooked process.

Figure 4.8. Acanthomorphic acritarchs from Siduping. (A) *Ericiasphaera sp.*, 13SDP-DST2-43, 135.5×23.3, E35-1. (B) Magnification of area indicated by arrow in (A), showing long solid processes. (C) *Urasphaera nupta*, 13SDP-DST2-43, 135.7×23.5, E35-2. (D) Magnification of rectangle area in (C), showing basal expansion of one process (black arrow) and apical expansion of another (white arrow). (E) Magnification of rectangle area in (D), showing anchor-like apical expansion of the same process but at slightly different focal level. (F) *Asterocapsoides sinensis*, with arrows pointing to obtuse conical processes on outer vesicle wall, 13SDP-DST2-43, 114.6×11.6, R14-2.

Figure 4.9. Acanthomorphic acritarchs from Siduping. (A) A poorly preserved acanthomorph, possibly *Appendisphaera magnifica*, S76.4-4-2, 137.5×17.5, L37-4. (B) Magnification of rectangle area in (A), showing ghost preservation of presumably hollow processes. (C–D)

Appendisphaera? *hemisphaerica*, S76.4-4-2, 134.2×18.9, J34-1. Two different focal levels showing transverse cross section of hemispherical base (center of D) and longitudinal cross section of apical spine of processes (periphery of C). (E) *Appendisphaera crebra*, S76.4-4-2, 138.2×17.4, L38-1. (F) Magnification of rectangle area in (E), showing poor preservation of processes.

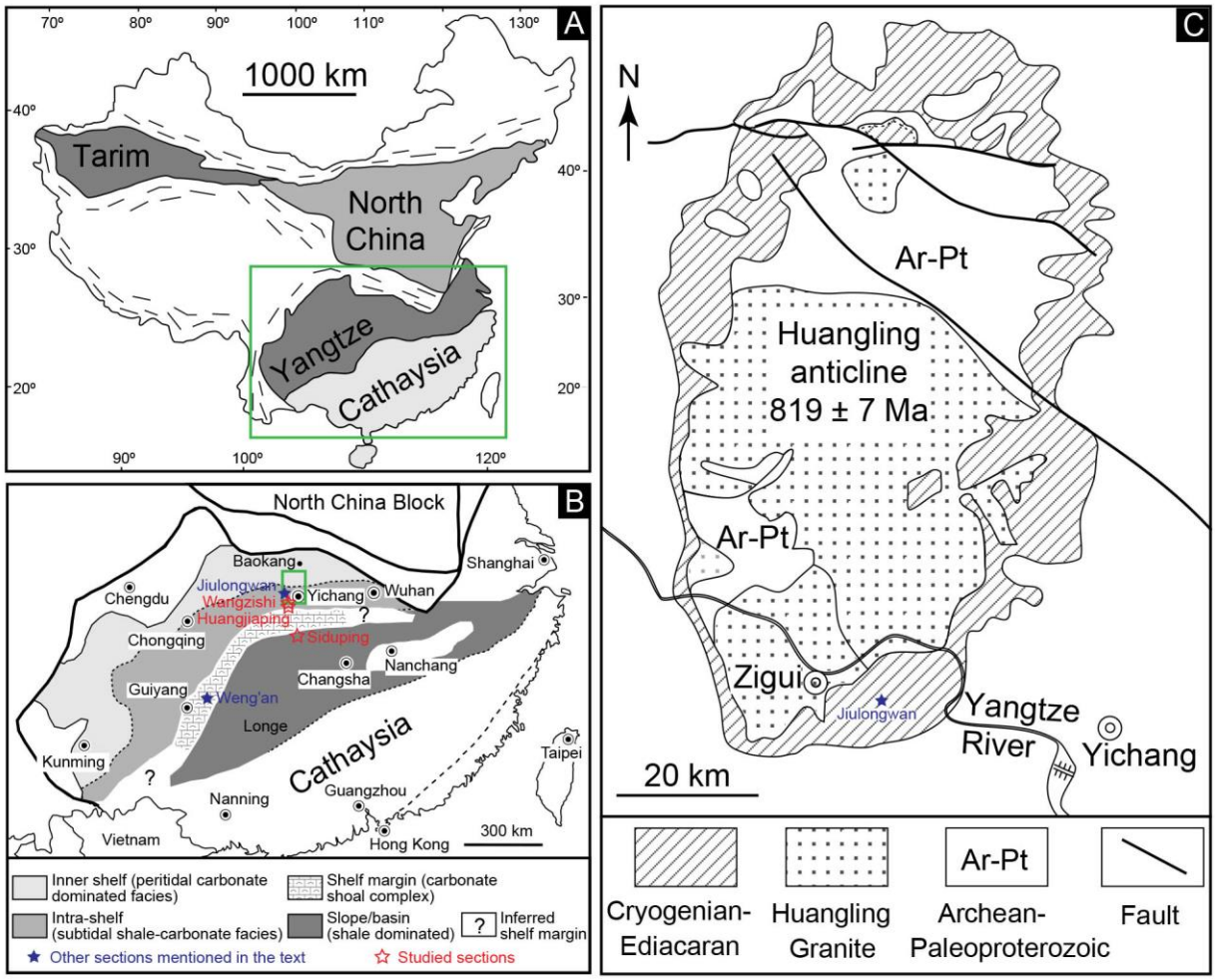
A
1000 km
Tarim
North China
Yangtze
Cathaysia
B
North China Block
Baokang
Shanghai
Chengdu
Jiulongwan
Wangzishi
Yichang
Wuhan
Huangjiaping
Chongqing
Siduping
Nanchang
Changsha
Guiyang
Weng'an
Longe
Kunming
Cathaysia
Taipei
Nanning
Guangzhou
Vietnam
Hong Kong
300 km
Inner shelf (peritidal carbonate dominated facies)
Shelf margin (carbonate shoal complex)
Intra-shelf (subtidal shale-carbonate facies)
Slope/basin (shale dominated)
Inferred shelf margin
Other sections mentioned in the text
Studied sections
C
N
Ar-Pt
Huangling anticline
819 ± 7 Ma
Ar-Pt
Zigui
Jiulongwan
Yangtze River
Yichang
20 km
Cryogenian-Ediacaran
Huangling Granite
Archean-Paleoproterozoic
Fault

Figure 4.1

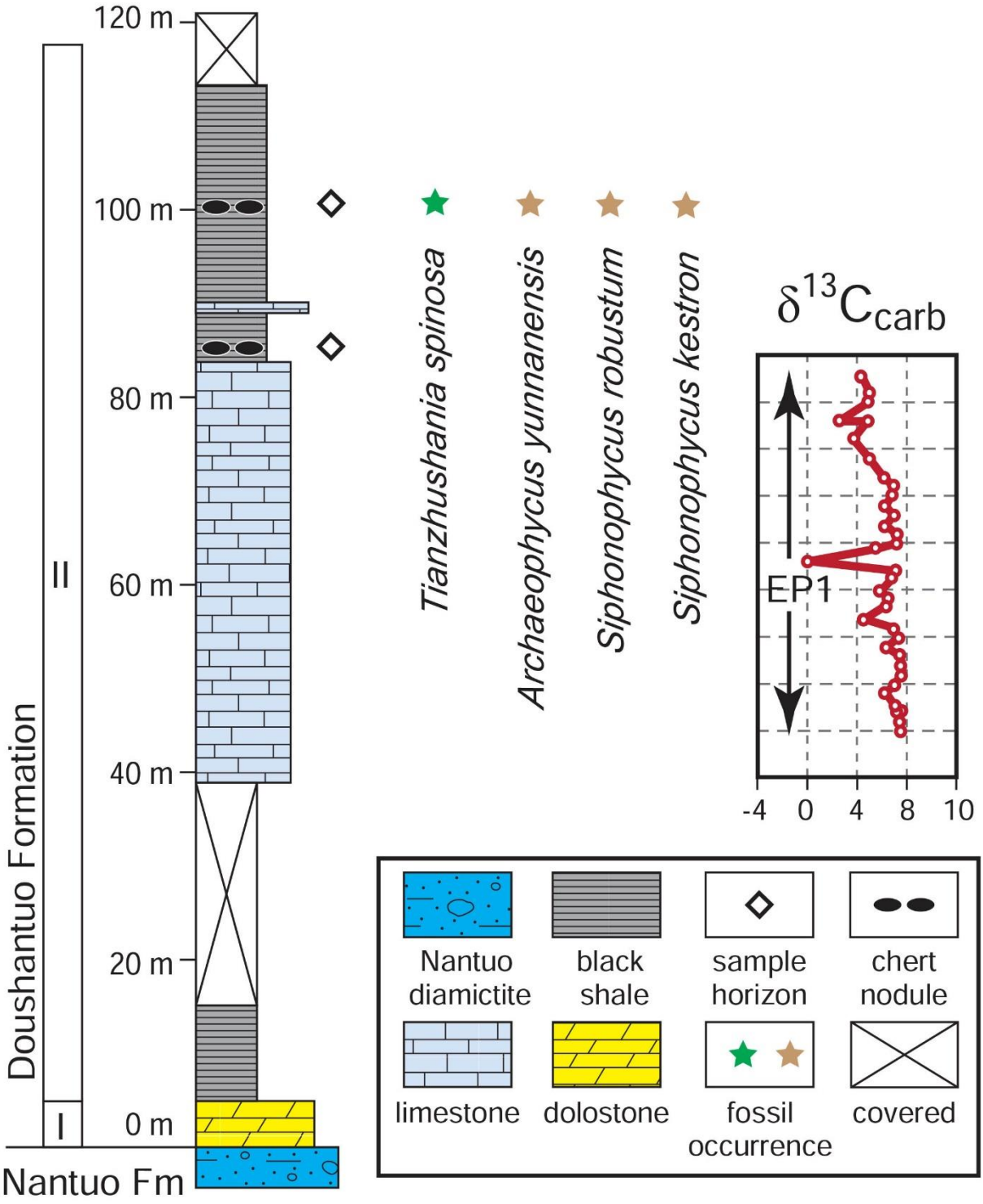
120 m
100 m
80 m
60 m
40 m
20 m
0 m
II
I
Doushantuo Formation
Nantuo Fm
Tianzhushania spinosa
Archaeophycus yunnanensis
Siphonophycus robustum
Siphonophycus kestron
δ13Ccarb
EP1
-4
0
4
8
10
Nantuo diamictite
black shale
sample horizon
chert nodule
limestone
dolostone
fossil occurrence
covered

Figure 4.2

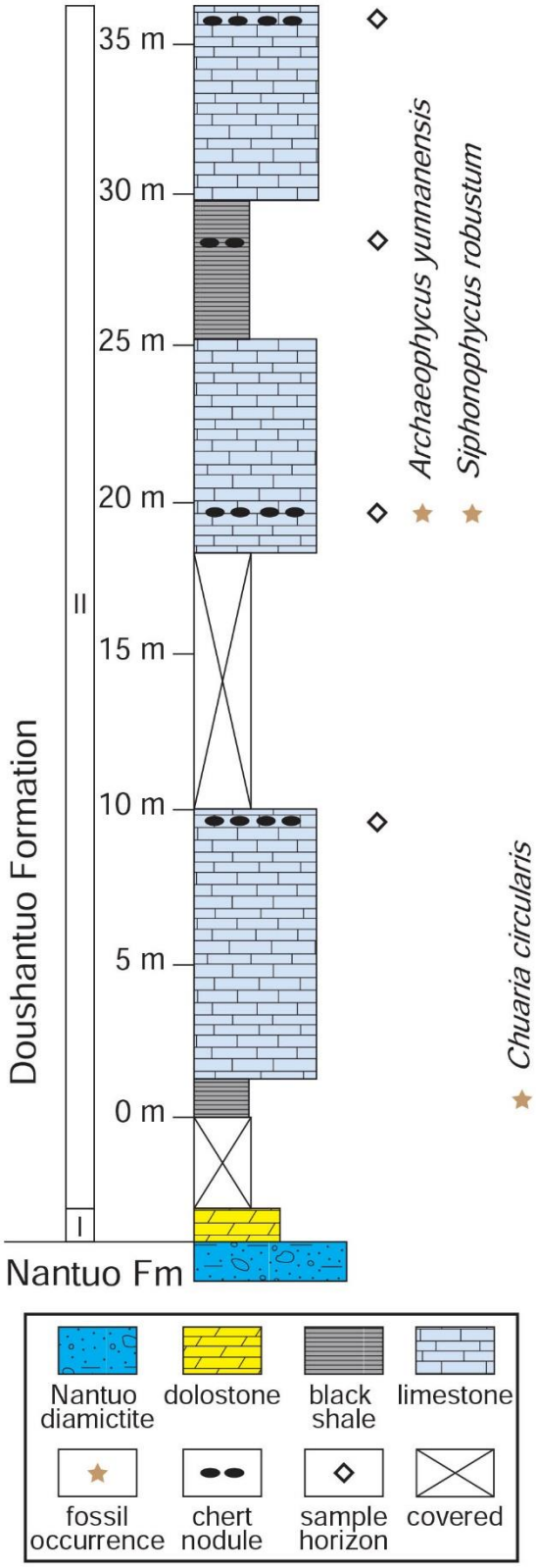
35 m
30 m
25 m
20 m
15 m
10 m
5 m
0 m
II
I
Doushantuo Formation
Nantuo Fm
Archaeophycus yunnanensis
Siphonophycus robustum
Chuaria circularis
Nantuo diamictite
dolostone
black shale
limestone
fossil occurrence
chert nodule
sample horizon
covered

Figure 4.3

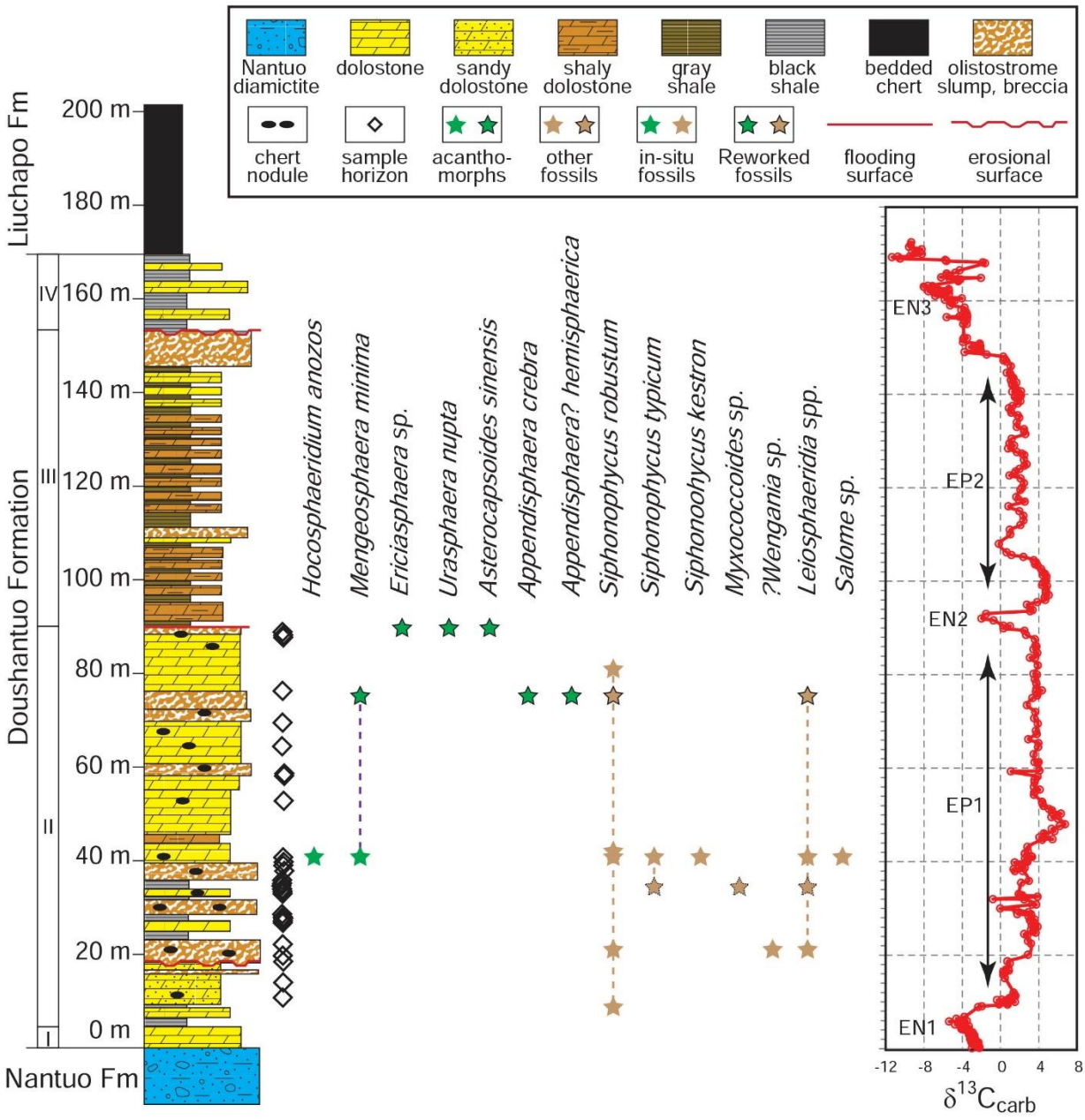
Nantuo diamictite
dolostone
sandy dolostone
shaly dolostone
gray shale
black shale
bedded chert
olistostrome slump, breccia
chert nodule
sample horizon
acantho-morphs
other fossils
in-situ fossils
Reworked fossils
flooding surface
erosional surface
Liuchapo Fm
Doushantuo Formation
Nantuo Fm
200 m
180 m
160 m
140 m
120 m
100 m
80 m
60 m
40 m
20 m
0 m
IV
III
II
I
Hocosphaeridium anozos
Mengeosphaera minima
Ericiasphaera sp.
Urasphaera nupta
Asterocapsoides sinensis
Appendisphaera crebra
Appendisphaera? hemisphaerica
Siphonophycus robustum
Siphonophycus typicum
Siphonoohycus kestron
Myxococcoides sp.
?Wengania sp.
Leiosphaeridia spp.
Salome sp.
EN3
EP2
EN2
EP1
EN1
-12
-8
-4
0
4
8
δ13Ccarb

Figure 4.4

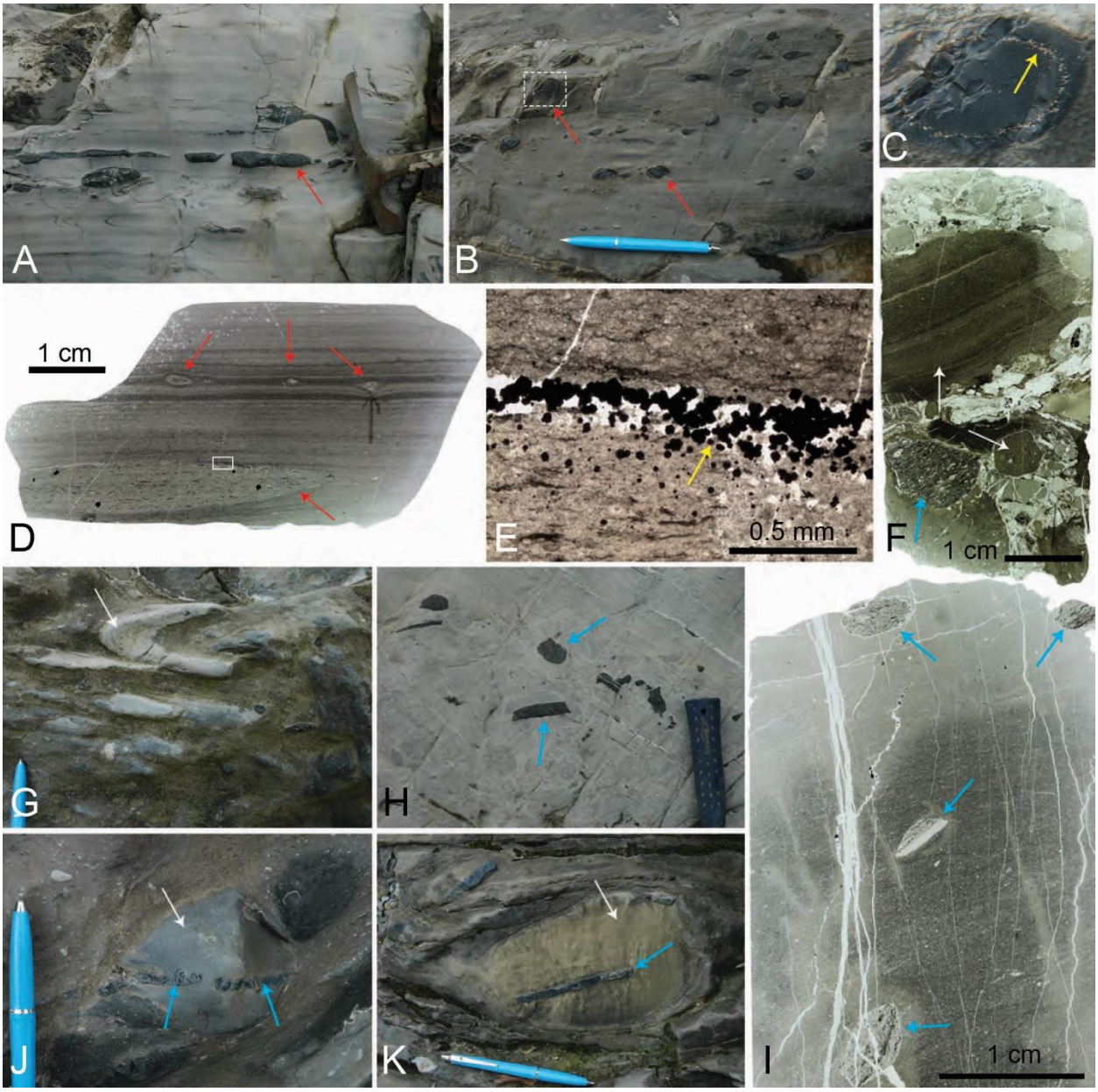

Figure 4.5

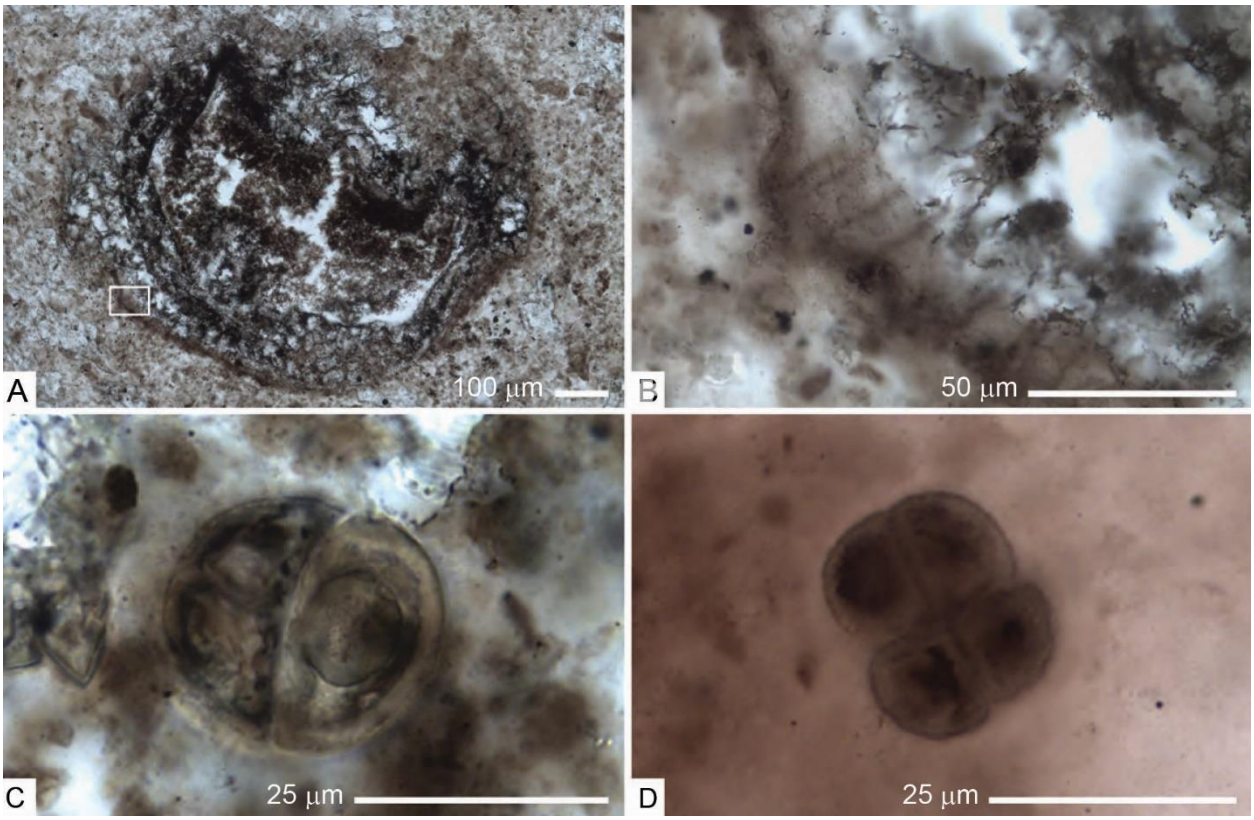

Figure 4.6

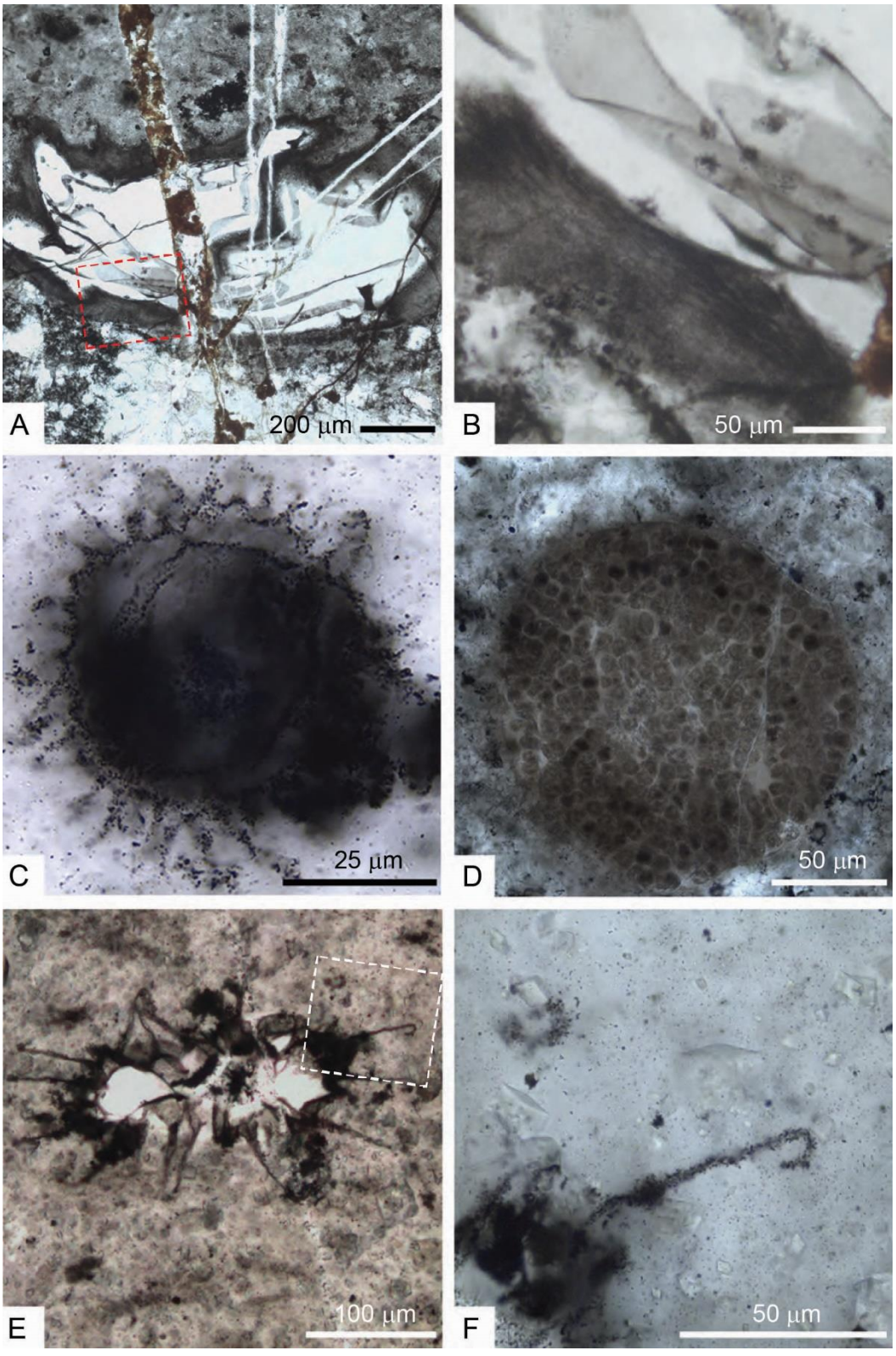

Figure 4.7

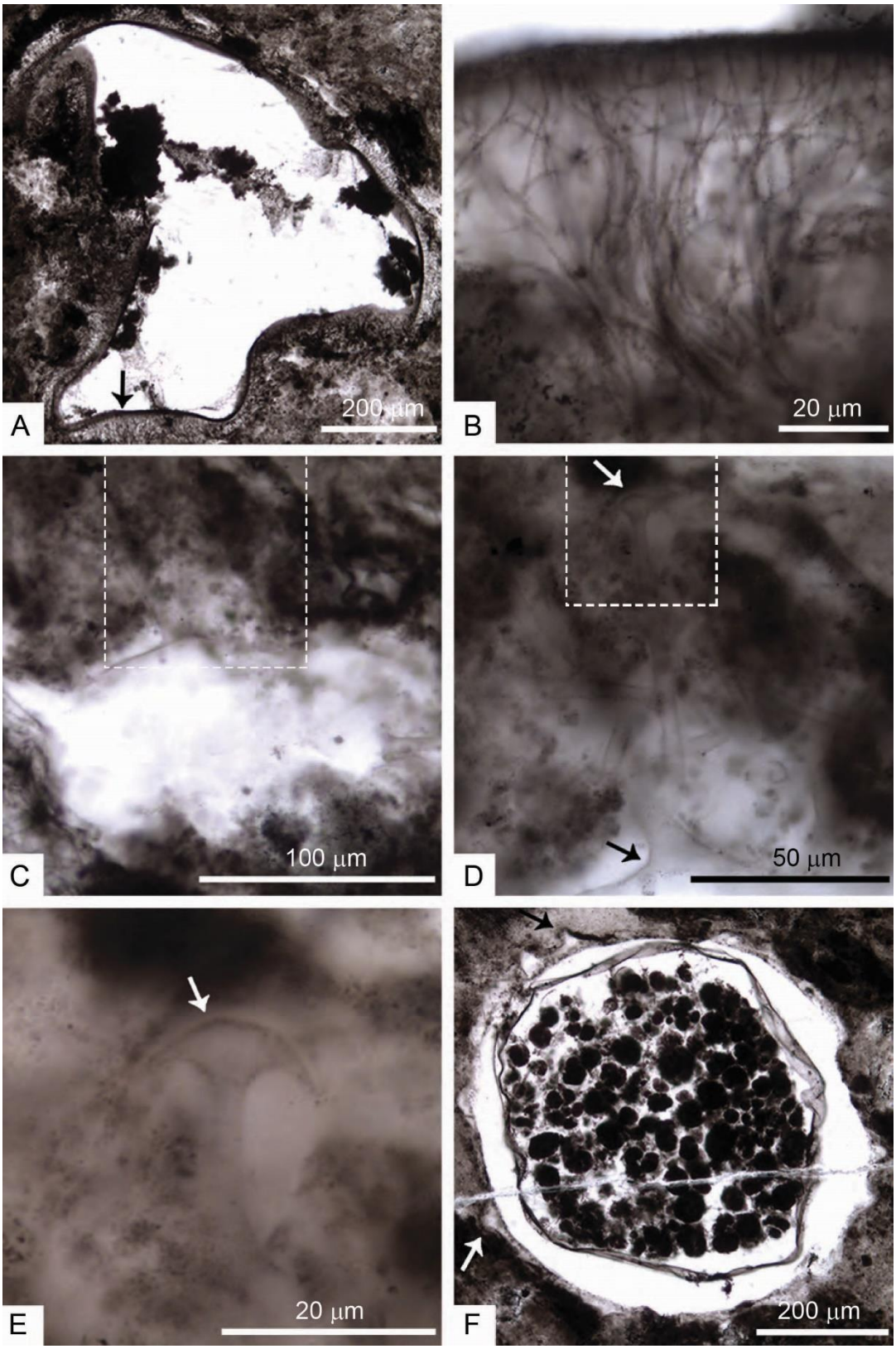

Figure 4.8

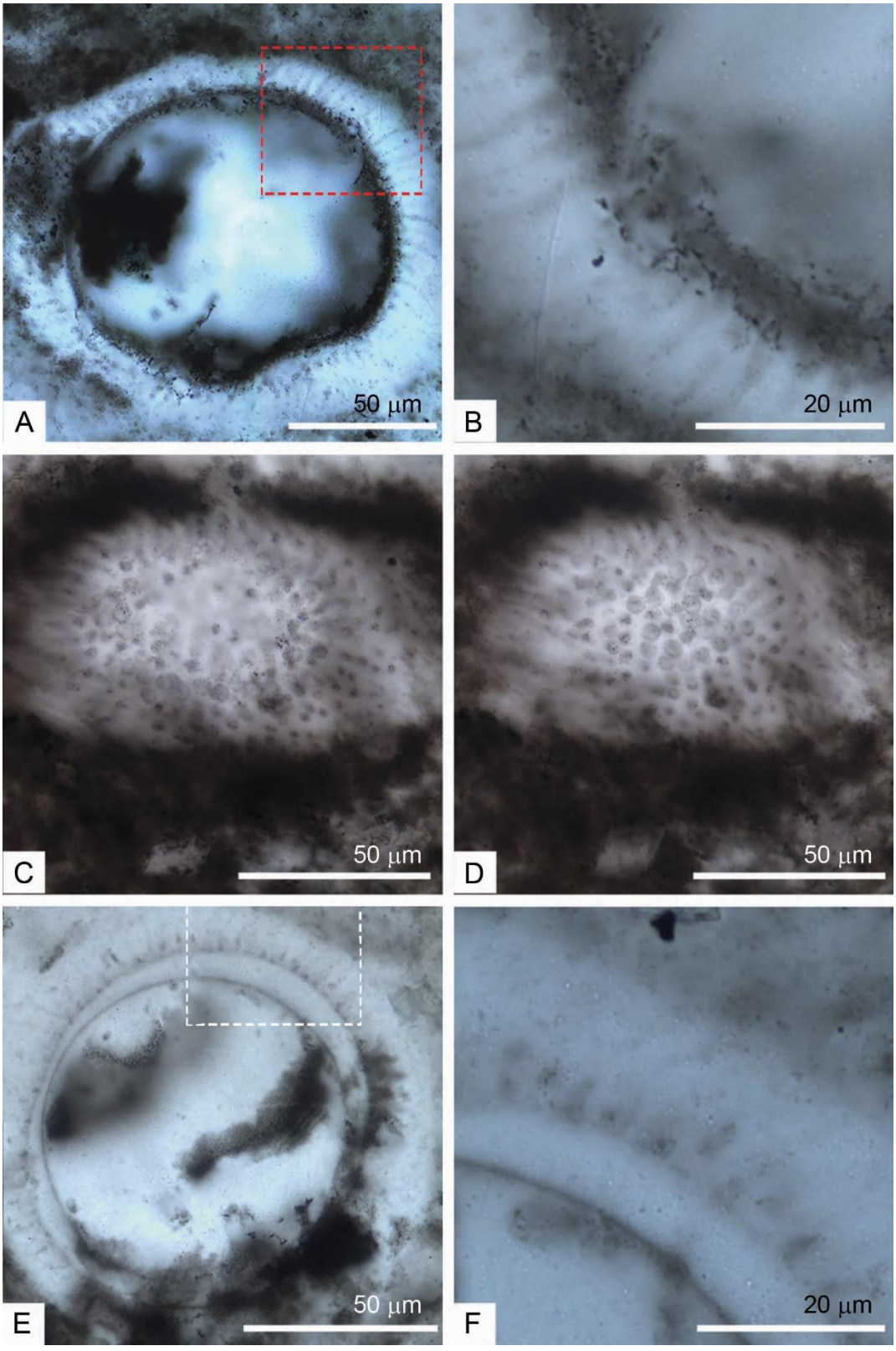

Figure 4.9

Conclusions

Here I present summaries of the main results for the projects associated with each of the chapters.

The following questions are examined in chapter 2. Can methods of fossil sampling from lithified rocks bias estimates of species richness, assemblage evenness and average specimen size? Is the magnitude of such bias sufficient to explain empirically observed differences between fossil assemblages from lithified and unlithified sediments in terms of species richness and assemblage evenness? How do assemblages with different species abundance and size distributions vary in terms of the magnitude of the bias induced by preferential intersection, and what implications does this have for variation in susceptibility to this bias through the Phanerozoic?

Model results demonstrate that preferential intersection can induce a biasing effect on estimates of species richness, assemblage evenness and average specimen size independent of the effects of other biasing mechanisms. The magnitude of this bias depends on the characters of the assemblage, particularly species abundance and size distributions. The magnitude of the induced bias is between half and one quarter of the difference observed between lithified and unlithified samples in empirical studies of the lithification bias, and therefore preferential intersection cannot fully explain the lithification bias. The factors that affect preferential intersection varied through the Phanerozoic. Low diversity, low evenness assemblages from lower Paleozoic settings may be little effected by this bias despite being almost exclusively derived from lithified sediments.

The main objective of chapter 3 is to understand the preservational modes, taphonomic processes, and likely trace makers of bromalites from the Middle Ordovician Winneshiek Lagerstätte. The interpretation of Winneshiek vermiform fossils as bromalites is supported by

several lines of evidence, including 1) evidence of loss of cohesion or liquefaction in some vermiform specimens, 2) conodont elements as undigested skeletal elements of food items preserved within vermiform specimens, 3) external morphological features reminiscent of feacal material and 4) a phosphatic composition that is a common mode of preservation for coprolites and cololites.

The microstructures of most studied vermiform fossils is dominated by homogenous, densely packed microspherules. The identity of these microstructures is uncertain and they may represent either phosphatic microspherical structures generated by the tracemaker during life or phosphatized coccoidal bacteria. Although we favor the former interpretation, neither can be rejected at this time. Whatever their identity the ubiquitous occurrence of these microspherical structures suggest they reflect an important component of vermiform phosphatization. Similar structures have been observed within phosphatized bromalites elsewhere, likely reflecting a common process of phosphatization in Winneshiek vermiform structures and other occurrences of phosphatized bromalites.

Several taxa co-occuring with the Winneshiek bromalites are potential tracemakers. These include eurypterids, placoderm fishes, “giant” conodonts and phylocarrid crustaceans. Eurypterids and conodonts have both been suggested as potential tracemakers at other localities where bromalites have been found. Based on their relative size and commonality at the Winneshiek Lagerstätte we regard these taxa as the most likely trace maker candidates.

The following questions are addressed in chapter 4. Are microfossils present in cherts of the Ediacaran Doushantuo Formation at the Wangzishi, Huangjiaping and Siduping sections in South China? Are biostratigraphically useful acanthomorphic acritarchs present? What do the biostratigraphic and chemostratigraphic records from these sections

tell us about the stratigraphic range of acanthomorph species in the Ediacaran Doushantuo Formation?

Microfossils were recovered from early diagenetic cherts at all three studied sections. Filamentous and coccoidal microfossils numerically dominated all samples. Specimens of *Tianzushania spinosa* were recovered from the sampled portion of the Wangzishi section, confirming the correlation of this portion of the section with Member II of the Doushantuo Formation as suggested by lithostratigraphy and carbon isotope chemostratigraphy. Multiple species of acanthomorphic acritarch were recovered from the upper slope Siduping section, including the biostratigraphically significant *Hocosphaeridium anozos*. In the Yangtze Gorges area *H. anozos* is present in Member III above the second negative carbon isotope excursion (EN2). However, at the Siduping section *H. anozos* is present in Member II of the Doushantuo Formation within EP1 and below EN2. The new discovery at Siduping is consistent with previous reports of the co-occurrence of *H. anozos* and *T. spinosa* in the upper Doushantuo Formation at Weng'an. Taken together, these data demonstrate that *H. anozos* is present in EP1 and stratigraphically overlaps with *T. spinosa*. Since the first appearance of *H. anozos* has been suggested to define the base of the eponymous *Tanarium conoideum-Hocosphaeridium scaberfacium-Hocosphaeridium anozos*-biozone, this means that either this biozone starts within Member II of the Doushantuo Formation or else that a transitional biozone separating the currently recognized lower biozone and a redefined upper biozone should be formally established.

References

Ader, M., M. Macouin, R. Trindade, M. Hadrien, Z. Yang, Z. Sun, and J. Besse. 2009. A multilayered water column in the Ediacaran Yangtze platform? Insights from carbonate and organic matter paired $\delta^{13}C$. Earth and Planetary Science Letters 288(1):213-227.

Aldridge, R. J., S. E. Gabbott, L. J. Siveter, and J. N. Theron. 2006. Bromalites from the Soom Shale Lagerstätte (Upper Ordovician) of South Africa: palaeoecological and palaeobiological implications. Palaeontology 49(4):857-871.

Allison, P. A. 1988. Konservat-Lagerstätten: cause and classification. Paleobiology 14(04):331-344.

Alroy, J., M. Aberhan, D. J. Bottjer, M. Foote, F. T. Fürsich, P. J. Harries, A. J. Hendy, S. M. Holland, L. C. Ivany, and W. Kiessling. 2008. Phanerozoic trends in the global diversity of marine invertebrates. Science 321:97-100.

Amstutz, G. C. 1958. Coprolites: A review of the literature and a study of specimens from southern Washington. Journal of Sedimentary Research 28(4):498-508.

An, Z., G. Jiang, J. Tong, L. Tian, Q. Ye, H. Song, and H. Song. 2015. Stratigraphic position of the Ediacaran Miaohe biota and its constrains on the age of the upper Doushantuo $\delta^{13}C$ anomaly in the Yangtze Gorges area, South China. Precambrian Research 271:243–253.

Becker, G. L., C.-H. Chen, J. W. Greenawalt, and A. L. Lehninger. 1974. Calcium phosphate granules in the hepatopancreas of the blue crab *Callinectes sapidus*. The Journal of Cell Biology 61(2):316-326.

Briggs, D. E. G., A. J. Kear, D. M. Martill, and P. R. Wilby. 1993. Phosphatization of soft-tissue in experiments and fossils. Journal of the Geological Society 150(6):1035-1038.

Briggs, D. E. G., H. P. Liu, R. M. McKay, and B. J. Witzke. 2015. Bivalved arthropods from the Middle Ordovician Winneshiek Lagerstätte, Iowa, USA. Journal of Paleontology 89(6):991-1006.

Briggs, D. E. G., and P. R. Wilby. 1996. The role of the calcium carbonate-calcium phosphate switch in the mineralization of soft-bodied fossils. Journal of the Geological Society 153(5):665-668.

Broce, J., J. D. Schiffbauer, K. S. Sharma, G. Wang, and S. Xiao. 2014. Possible Animal Embryos from the Lower Cambrian (Stage 3) Shuijingtuo Formation, Hubei Province, South China. Journal of Paleontology 88(2):385-394.

Brown, B. E. 1982. The form and function of metal-containing 'granules' in invertebrate tissues. Biological Reviews 57(4):621-667.

Bulmer, M. 1974. On fitting the Poisson lognormal distribution to species-abundance data. Biometrics:101-110.

Burton, R. F. 1972. The storage of calcium and magnesium phosphates and of calcite in the digestive glands of the Pulmonata (Gastropoda). Comparative Biochemistry and Physiology Part A: Physiology 43(3):655-663.

Bush, A. M., and R. K. Bambach. 2004. Did alpha diversity increase during the Phanerozoic? Lifting the veils of taphonomic, latitudinal, and environmental biases. The Journal of Geology 112:625-642.

Butterfield, N. J. 2002. *Leanchoilia* guts and the interpretation of three-dimensional structures in Burgess Shale-type fossils. Paleobiology 28(01):155-171.

Cherns, L., and V. P. Wright. 2000. Missing molluscs as evidence of large-scale, early skeletal aragonite dissolution in a Silurian sea. Geology 28:791-794.

Cherns, L., and V. P. Wright. 2009. Quantifying the impacts of early diagenetic aragonite dissolution on the fossil record. Palaios 24:756-771.

Condon, D., M. Zhu, S. Bowring, W. Wang, A. Yang, and Y. Jin. 2005. U-Pb ages from the neoproterozoic Doushantuo Formation, China. Science 308(5718):95-98.

Corrêa, J. D., M. Farina, and S. Allodi. 2002. Cytoarchitectural features of *Ucides cordatus* (Crustacea Decapoda) hepatopancreas: structure and elemental composition of electron-dense granules. Tissue and Cell 34(5):315-325.

Cui, H., A. J. Kaufman, S. Xiao, M. Zhu, C. Zhou, and X.-M. Liu. 2015. Redox architecture of an Ediacaran ocean margin: integrated chemostratigraphic ($\delta^{13}C$ - $\delta^{34}S$ - $^{87}Sr/^{86}Sr$ - Ce/Ce^{*}) correlation of the Doushantuo Formation. Chemical Geology 405:48-62.

Daley, G. M., and A. M. Bush. 2012. How and why does lithification bias biodiversity? A test based on experimental lithification of unconsolidated sediments. Geological Society of America Abstracts with Programs 44(7):33.

Daley, G. M., and A. M. Bush. 2014. Lithification does not neccessarily bias diversity: experimental evidence from synthetic rocks. Geological Society of America Abstracts with Programs 46(6):329.

Fisher, R. A., A. S. Corbet, and C. B. Williams. 1943. The relation between the number of species and the number of individuals in a random sample of an animal population. The Journal of Animal Ecology:42-58.

Foote, M., J. S. Crampton, A. G. Beu, and C. S. Nelson. 2015. Aragonite bias, and lack of bias, in the fossil record: lithological, environmental, and ecological controls. Paleobiology 41:245-265.

Garvie, C. L. 1996. The Molluscan Macrofauna of the Reklaw Formation, Marquez Member (Eocene, Lower Claibornian), in Texas. Bulletin of American Paleontology. 111, 1-177.

Gilmore, B. 1992. Scroll coprolites from the Silurian of Ireland and the feeding of early vertebrates. Palaeontology 35(2):319-333.

Grotzinger, J. P., D. A. Fike, and W. W. Fischer. 2011. Enigmatic origin of the largest-known carbon isotope excursion in Earth's history. Nature Geoscience 4(5):285-292.

Hendy, A. J. 2009. The influence of lithification on Cenozoic marine biodiversity trends. Paleobiology 35:51-62.

Hendy, A. J. 2011. Taphonomic overprints on Phanerozoic trends in biodiversity: lithification and other secular megabiases. Pp. 19-77. *In* P. A. Allison, and D. J. Bottjer, eds. Taphonomy. Springer.

Hollocher, K., and T. C. Hollocher. 2012. Early processes in the fossilization of terrestrial feces to coprolites, and microstructure preservation. Pp. 79-91. *In* A. P. Hunt, J. Milàn, S. G. Lucas, and J. A. Spielmann, eds. Vertebrate Coprolites. New Mexico Museum of Natural History and Science, Albuquerque, New Mexico.

Hopkin, S. P. 1990. Critical concentrations, pathways of detoxification and cellular ecotoxicology of metals in terrestrial arthropods. Functional Ecology 4:321-327.

Hopkin, S. P., and J. A. Nott. 1979. Some observations on concentrically structured, intracellular granules in the hepatopancreas of the shore crab *Carcinus maenas* (L.). Journal of the Marine Biological Association of the United Kingdom 59(04):867-877.

Howard, B., P. C. H. Mitchell, A. Ritchie, K. Simkiss, and M. Taylor. 1981. The composition of intracellular granules from the metal-accumulating cells of the common garden snail (*Helix aspersa*). Biochemical Journal 194(2):507-511.

Hunt, A. P. 1992. Late Pennsylvanian coprolites from the Kinney Brick Quarry, central New Mexico, with notes on the classification and utility of coprolites. New Mexico Bureau of Mines and Mineral Resources, Bulletin 138:221-229.

Jain, S. L. 1983. Spirally coiled "coprolites" from the Upper Triassic Maleri Formation, India. Palaeontology 26(4):813-829.

Jiang, G., A. J. Kaufman, N. Christie-Blick, S. Zhang, and H. Wu. 2007. Carbon isotope variability across the Ediacaran Yangtze platform in South China: Implications for a large surface-to-deep ocean $\delta^{13}C$ gradient. Earth and Planetary Science Letters 261(1):303-320.

Jiang, G., M. J. Kennedy, and N. Christie-Blick. 2003. Stable isotopic evidence for methane seeps in Neoproterozoic postglacial cap carbonates. Nature 426:822-826.
Jiang, G., X. Shi, S. Zhang, Y. Wang, and S. Xiao. 2011. Stratigraphy and paleogeography of the Ediacaran Doushantuo Formation (ca. 635–551Ma) in South China. Gondwana Research 19(4):831-849.
Kass, M. A., P. A. Bedrosian, B. J. Drenth, B. R. Bloss, R. M. McKay, H. Liu, B. M. French, and B. J. Witzke. 2013a. Geophysical signatures and modeling results from a buried impact structure in Decorah, Iowa, USA. American Geophysical Union Fall Meeting:Abstract P34C-04.
Kass, M. A., P. A. Bedrosian, B. J. Drenth, B. R. Bloss, R. M. McKay, H. Liu, B. M. French, and B. J. Witzke. 2013b. Modeling and inversion results from airborne geophysics over a buried impact structure in Decorah, Iowa, USA. Geological Society of America Abstracts with Programs 45(7):485.
Kidwell, S. M. 2005. Shell composition has no net impact on large-scale evolutionary patterns in mollusks. Science 307:914-917.
Korochantseva, E. V., M. Trieloff, C. A. Lorenz, A. I. Buykin, M. A. Ivanova, W. H. Schwarz, J. Hopp, and E. K. Jessberger. 2007. L-chondrite asteroid breakup tied to Ordovician meteorite shower by multiple isochron ^{40}Ar-^{39}Ar dating. Meteoritics & Planetary Science 42(1):113-130.
Kowalewski, M., M. Carroll, L. Casazza, N. S. Gupta, B. Hannisdal, A. Hendy, A. Richard Jr, M. LaBarbera, D. G. Lazo, and C. Messina. 2003. Quantitative fidelity of brachiopod-mollusk assemblages from modern subtidal environments of San Juan Islands, USA. Journal of Taphonomy 1(1):43-65.
Kowalewski, M., and A. P. Hoffmeister. 2003. Sieves and fossils: Effects of mesh size on paleontological patterns. Palaios 18:460-469.
Kowalewski, M., S. L. B. Wood, W. Kiessling, M. Aberhan, F. T. Fürsich, D. Scarponi, and A. P. Hoffmeister. 2006. Ecological, taxonomic, and taphonomic components of the post-Paleozoic increase in sample-level species diversity of marine benthos. Paleobiology 32:533-561.
Kraeuter, J., and D. S. Haven. 1970. Fecal pellets of common invertebrates of lower York River and lower Chesapeake Bay, Virginia. Chesapeake Science 11(3):159-173.
Lamboy, M., V. P. Rao, E. Ahmed, and N. Azzouzi. 1994. Nannostructure and significance of fish coprolites in phosphorites. Marine Geology 120(3-4):373-383.
Lamsdell, J. C., D. E. G. Briggs, H. P. Liu, B. J. Witzke, and R. M. McKay. 2015a. A new Ordovician arthropod from the Winneshiek Lagerstätte of Iowa (USA) reveals the ground plan of eurypterids and chasmataspidids. The Science of Nature 102:63.
Lamsdell, J. C., D. E. G. Briggs, H. P. Liu, B. J. Witzke, and R. M. McKay. 2015b. The oldest described eurypterid: a giant Middle Ordovician (Darriwilian) megalograptid from the Winneshiek Lagerstätte of Iowa. BMC Evolutionary Biology 15(1):1.
Lamsdell, J. C., S. T. LoDuca, G. O. Gunderson, R. C. Meyer, and D. E. G. Briggs. 2017. A new Lagerstätte from the Late Ordovician Big Hill Formation, Upper Peninsula, Michigan. Journal of the Geological Society 174:18-22.
Li, C., D. S. Hardisty, G. Luo, J. Huang, T. J. Algeo, M. Cheng, W. Shi, Z. An, J. Tong, S. Xie, N. Jiao, and T. W. Lyons. 2017. Uncovering the spatial heterogeneity of Ediacaran carbon cycling. Geobiology 15:211-224.
Li, C., G. D. Love, T. W. Lyons, D. A. Fike, A. L. Sessions, and X. Chu. 2010. A stratified redox model for the Ediacaran ocean. Science 328:80-83.
Li, C., N. J. Planavsky, W. Shi, Z. Zhang, C. Zhou, M. Cheng, L. G. Tarhan, G. Luo, and S. Xie. 2015. Ediacaran marine redox heterogeneity and early animal ecosystems. Scientific Reports 5:17097.
Liu, H., R. McKay, B. Witzke, and D. Briggs. 2009. The Winneshiek Lagerstätte, Iowa, USA and its depositional environments. Geological Journal of China Universities 15:285-289.
Liu, H. P., S. M. Bergström, B. J. Witzke, D. E. G. Briggs, R. M. McKay, and A. Ferretti. 2017. Exceptionally preserved conodont apparatuses with giant elements from the Middle Ordovician Winneshiek Konservat-Lagerstätte, Iowa, USA. Journal of Paleontology 91:493-511.

Liu, H. P., R. M. McKay, J. N. Young, B. J. Witzke, K. J. McVey, and X. Liu. 2006. A new Lagerstätte from the Middle Ordovician St. Peter Formation in northeast Iowa, USA. Geology 34(11):969-972.

Liu, P., S. Chen, M. Zhu, M. Li, C. Yin, and X. Shang. 2014a. High-resolution biostratigraphic and chemostratigraphic data fromthe Chenjiayuanzi section of the Doushantuo Formation in the Yangtze Gorges area, South China: Implication for subdivision andglobal correlation of the Ediacaran System. Precambrian Research 249:199-214.

Liu, P., S. Xiao, C. Yin, S. Chen, C. Zhou, and M. Li. 2014b. Ediacaran acanthomorphic acritarchs and other microfossils from chert nodules of the upper Doushantuo Formation in the Yangtze Gorges area, South China. Journal of Paleontology 72 (supplement to No 1):1-139.

Liu, P., C. Yin, S. Chen, F. Tang, and L. Gao. 2013. The biostratigraphic succession of acanthomorphic acritarchs of the Ediacaran Doushantuo Formation in the Yangtze Gorges area, South China and its biostratigraphic correlation with Australia. Precambrian Research 225:29-43.

Loret, S. M., and P. E. Devos. 1992. Structure and possible functions of the calcospherite-rich cells (R* cells) in the digestive gland of the shore crab *Carcinus maenas*. Cell and Tissue Research 267(1):105-111.

Martin, R. E. 1999. Taphonomy: a process approach. Cambridge University Press, Cambridge, 508.

Mason, A. Z., and J. A. Nott. 1981. The role of intracellular biomineralized granules in the regulation and detoxification of metals in gastropods with special reference to the marine prosobranch *Littorina littorea*. Aquatic Toxicology 1(3):239-256.

MATLAB 8.6, T. M., Inc., Natick, Massachusetts, United States.

McAllister, J. A. 1985. Reevaluation of the formation of spiral coprolites. University of Kansas, Paleontological Contributions 114:1-12.

McFadden, K. A., J. Huang, X. Chu, G. Jiang, A. J. Kaufman, C. Zhou, X. Yuan, and S. Xiao. 2008. Pulsed oxidation and biological evolution in the Ediacaran Doushantuo Formation. Proceedings of the National Academy of Sciences 105(9):3197-3202.

McFadden, K. A., S. Xiao, C. Zhou, and M. Kowalewski. 2009. Quantitative evaluation of the biostratigraphic distribution of acanthomorphic acritarchs in the Ediacaran Doushantuo Formation in the Yangtze Gorges area, South China. Precambrian Research 173(1):170-190.

McKay, R., H. Liu, B. J. Witzke, B. M. French, and D. E. G. Briggs. 2011. Preservation of the Middle Ordovician Winneshiek Shale in a probable impact crater. Geological Society of America Abstracts with Programs 43(5):189.

McKay, R. M., H. P. Liu, B. J. Witzke, and B. M. French. 2010. Geologic setting of the Winneshiek Lagerstätte-Decorah, Iowa. Geological Society of America Abstracts with Programs 42(2):89.

McKinney, M. L. 1986. Estimating volumetric fossil abundance from cross-sections: a stereological approach. Palaios:79-84.

Muscente, A., A. D. Hawkins, and S. Xiao. 2015. Fossil preservation through phosphatization and silicification in the Ediacaran Doushantuo Formation (South China): a comparative synthesis. Palaeogeography, Palaeoclimatology, Palaeoecology 434:46-62.

Nawrot, R. 2012. Decomposing lithification bias: preservation of local diversity structure in recently cemented storm-beach carbonate sands, San Salvador Island, Bahamas. Palaios 27:190-205.

Nowak, H., T. H. P. Harvey, H. P. Liu, R. M. McKay, and T. Servais. in press. Exceptionally preserved arthropodan microfossils from the Middle Ordovician Winneshiek Lagerstätte, Iowa, USA. Lethaia.

Ouyang, Q., C. Guan, C. Zhou, and S. Xiao. 2017. Acanthomorphic acritarchs of the Doushantuo Formation from an upper slope section in northwestern Hunan Province, South China, with implications for early Ediacaran biostratigraphy. Precambrian Research in revision.

Peckmann, J., B. Senowbari-Daryan, D. Birgel, and J. Goedert. 2007. The crustacean ichnofossil Palaxius associated with callianassid body fossils in an Eocene methane-seep limestone, Humptulips Formation, Olympic Peninsula, Washington. Lethaia 40:273-280.
Peel, J. S. 2015. Bromalites from the Cambrian (Series 2 and 3) of North Greenland. GFF 137(3):181-194.
Peel, J. S. 2017. Mineralized gutfills from the Sirius Passet Lagerstätte (Cambrian Series 2) of North Greenland. GFF 139:83-91.
Pesquero, M. D., V. Souza-Egipsy, L. Alcalá, C. Ascaso, and Y. Fernández-Jalvo. 2014. Calcium phosphate preservation of faecal bacterial negative moulds in hyaena coprolites. Acta Palaeontologica Polonica 59(4):997-1005.
Peterson, T. D. 1996. A refined technique for measuring crystal size distributions in thin section. Contributions to Mineralogy and Petrology 124:395-405.
Pielou, E. C. 1966. The measurement of diversity in different types of biological collections. Journal of theoretical biology 13:131-144.
Powell, M. G., and M. Kowalewski. 2002. Increase in evenness and sampled alpha diversity through the Phanerozoic: comparison of early Paleozoic and Cenozoic marine fossil assemblages. Geology 30:331-334.
Pullen, J. S. H., and P. S. Rainbow. 1991. The composition of pyrophosphate heavy metal detoxification granules in barnacles. Journal of Experimental Marine Biology and Ecology 150(2):249-266.
Raup, D. M. 1966. Geometric analysis of shell coiling: General problems. Journal of Paleontology 40:1178-1190.
Roy, K., D. Jablonski, and K. K. Martien. 2000. Invariant size–frequency distributions along a latitudinal gradient in marine bivalves. Proceedings of the National Academy of Sciences 97:13150-13155.
Sahoo, S. K., N. J. Planavsky, G. Jiang, B. Kendall, J. D. Owens, X. Wang, X. Shi, A. D. Anbar, and T. W. Lyons. 2016. Oceanic oxygenation events in the anoxic Ediacaran ocean. Geobiology 14:457-468.
Sanders, M. T., D. Merle, and L. Villier. 2015. The molluscs of the “Falunière” of Grignon (Middle Lutetian, Yvelines, France): quantification of lithification bias and its impact on the biodiversity assessment of the Middle Eocene of Western Europe. Geodiversitas 37:345-365.
Schmitz, B., D. A. Harper, B. Peucker-Ehrenbrink, S. Stouge, C. Alwmark, A. Cronholm, S. M. Bergström, M. Tassinari, and W. Xiaofeng. 2008. Asteroid breakup linked to the Great Ordovician biodiversification event. Nature Geoscience 1(1):49-53.
Scoffin, T. P. 1973. Crustacean faecal pellets, Favreina, from the Middle Jurassic of Eigg, Inner Hebrides. Scottish Journal of Geology 9(2):145-146.
Sessa, J. A., M. E. Patzkowsky, and T. J. Bralower. 2009. The impact of lithification on the diversity, size distribution, and recovery dynamics of marine invertebrate assemblages. Geology 37:115-118.
Shen, B., C.-T. Lee, and S. Xiao. 2011. Germanium/silicon ratios in diagenetic chert nodules from the Ediacaran Doushantuo Formation, South China. Chemical Geology 280:323-335.
Shen, C., B. R. Pratt, and X.-g. Zhang. 2014. Phosphatized coprolites from the middle Cambrian (Stage 5) Duyun fauna of China. Palaeogeography Palaeoclimatology Palaeoecology 410:104-112.
Simkiss, K., and M. G. Taylor. 1994. The formation of apatite from crab faecal pellets. Journal of the Marine Biological Association of the United Kingdom 74(02):459-462.
Tahata, M., Y. Ueno, T. Ishikawa, Y. Sawaki, K. Murakami, J. Han, D. Shu, Y. Li, J. Guo, N. Yoshida, and T. Komiya. 2013. Carbon and oxygen isotope chemostratigraphies of the Yangtze platform, South China: Decoding temperature and environmental changes through the Ediacaran. Gondwana Research 23:333-353.
Team, R. C. 2014. R: A language and environment for statistical computing. R Foundation for Statistical Computing, Vienna, Austria. 2013.
Van Roy, P., D. E. G. Briggs, and R. R. Gaines. 2015. The Fezouata fossils of Morocco; an extraordinary record of marine life in the Early Ordovician. Journal of the Geological Society 172(5):541-549.

Vannier, J., J. Liu, R. Lerosey-Aubril, J. Vinther, and A. C. Daley. 2014. Sophisticated digestive systems in early arthropods. Nature communications 5:1-9.
Vernhet, E., C. Heubeck, M.-Y. Zhu, and J.-M. Zhang. 2006. Large-scale slope instability at the southern margin of the Ediacaran Yangtze platform (Hunan province, central China). Precambrian Research 148:32–44.
Wagner, P. J., M. A. Kosnik, and S. Lidgard. 2006. Abundance distributions imply elevated complexity of post-Paleozoic marine ecosystems. Science 314:1289-1292.
Wang, J., G. Jiang, S. Xiao, Q. Li, and Q. Wei. 2008. Carbon isotope evidence for widespread methane seeps in the ~635 Ma Doushantuo cap carbonate in South China. Geology 36:347-350.
Wang, L., X. Shi, and G. Jiang. 2012. Pyrite morphology and redox fluctuations recorded in the Ediacaran Doushantuo Formation. Palaeogeography, Palaeoclimatology, Palaeoecology 333:218-227.
Wang, W., C. Guan, C. Zhou, Y. Peng, L. Pratt, X. Chen, L. Chen, Z. Chen, X. Yuan, and S. Xiao. 2017a. Integrated carbon, sulfur, and nitrogen isotope chemostratigraphy of the Ediacaran Lantian Formation in South China: Spatial gradient, ocean redox oscillation, and fossil distribution. Geobiology.
Wang, X., G. Jiang, X. Shi, and S. Xiao. 2016. Paired carbonate and organic carbon isotope variations of the Ediacaran Doushantuo Formation from an upper slope section at Siduping, South China. Precambrian Research 273:53-66.
Wang, Z., J. Wang, Y. Kouketsu, R. J. Bodnar, B. C. Gill, and S. Xiao. 2017b. Raman geothermometry of carbonaceous material in the basal Ediacaran Doushantuo cap dolostone: the thermal history of extremely negative $\delta^{13}C$ signatures in the aftermath of the terminal Cryogenian snowball Earth glaciation. Precambrian Research.
Wang, Z., J. Wang, E. Suess, G. Wang, C. Chen, and S. Xiao. 2017c. Silicified glendonites in the Ediacaran Doushantuo Formation (South China) and their potential paleoclimatic implications. Geology 45:115-118.
Wen, H., H. Fan, S. Tian, QilianWang, and R. Hu. 2016. The formation conditions of the early Ediacaran cherts, South China. Chemical Geology 430:45-69.
Williams, M. E. 1972. The origin of "spiral coprolites". The University of Kansas Paleontological Contributions 59:1-19.
Witzke, B. J., R. M. McKay, H. P. Liu, and D. E. G. Briggs. 2011. The Middle Ordovician Winneshiek Shale of Northeast Iowa - correlation and paleogeographic implications. Geological Society of America Abstracts with Programs 43(5):315.
Xiao, S. 2004. New multicellular algal fossils and acritarchs in Doushantuo chert nodules (Neoproterozoic, Yangtze Gorges, South China). Journal of Paleontology 78:393-401.
Xiao, S., K. A. McFadden, S. Peek, A. J. Kaufman, C. Zhou, G. Jiang, and J. Hu. 2012. Integrated chemostratigraphy of the Doushantuo Formation at the northern Xiaofenghe section (Yangtze Gorges, South China) and its implication for Ediacaran stratigraphic correlation and ocean redox models. Precambrian Research 192-95:125-141.
Xiao, S., A. D. Muscente, L. Chen, C. Zhou, J. D. Schiffbauer, A. D. Wood, N. F. Polys, and X. Yuan. 2014a. The Weng'an biota and the Ediacaran radiation of multicellular eukaryotes. National Science Review 1(4):498-520.
Xiao, S., G. M. Narbonne, C. Zhou, M. Laflamme, D. V. Grazhdankin, M. Moczydłowska-Vidal, and H. Cui. 2016. Toward an Ediacaran time scale: problems, protocols, and prospects. Episodes 39:540–555.
Xiao, S., J. D. Schiffbauer, K. A. McFadden, and J. Hunter. 2010. Petrographic and SIMS pyrite sulfur isotope analyses of Ediacaran chert nodules: Implications for microbial processes in pyrite rim formation, silicification, and exceptional fossil preservation. Earth and Planetary Science Letters 297(3):481-495.

Xiao, S., C. Zhou, P. Liu, D. Wang, and X. Yuan. 2014b. Phosphatized acanthomorphic acritarchs and related microfossils from the Ediacaran Doushantuo Formation at Weng'an (South China) and their implications for biostratigraphic correlation. Journal of Paleontology 88(1):1-67.
Yin, C. 1999. Microfossils from the Upper Sinian (late Neoproterozoic) Doushantuo Formation in Changyang, western Hubei, China. Continental Dynamics 4:1-18.
Yin, C., P. Liu, S. Chen, F. Tang, L. Gao, and Z. Wang. 2009. Acritarch biostratigraphic succession of the Ediacaran Doushantuo Formation in the Yangtze Gorges. Acta Palaeontologica Sinica 48:146-154.
Young, G. A., D. M. Rudkin, E. P. Dobrzanski, S. P. Robson, M. B. Cuggy, M. W. Demski, and D. P. Thompson. 2013. Great Canadian Lagerstätten 3. Late Ordovician Konservat-Lagerstätten in Manitoba. Geoscience Canada 39(4):201-213.
Young, G. A., D. M. Rudkin, E. P. Dobrzanski, S. P. Robson, and G. S. Nowlan. 2007. Exceptionally preserved Late Ordovician biotas from Manitoba, Canada. Geology 35(10):883-886.
Zabini, C., J. D. Schiffbauer, S. Xiao, and M. Kowalewski. 2012. Biomineralization, taphonomy, and diagenesis of Paleozoic lingulide brachiopod shells preserved in silicified mudstone concretions. Palaeogeography Palaeoclimatology Palaeoecology 326-328:118-127.
Zhao, Z.-q., Y.-s. Xing, Q.-x. Ding, G. Liu, Y. Zhao, S. Zhang, X. Meng, C. Yin, B. Ning, and P. Han. 1988. The Sinian System of Hubei. China University of Geosciences Press, Wuhan 205.
Zhou, C., and S. Xiao. 2007. Ediacaran δ 13 C chemostratigraphy of South China. Chemical Geology 237(1):89-108.
Zhou, C., S. Xiao, W. Wang, C. Guan, Q. Ouyang, and Z. Chen. 2017. The stratigraphic complexity of the middle Ediacaran carbon isotopic record in the Yangtze Gorges area, South China, and its implications for the age and chemostratigraphic significance of the Shuram excursion. Precambrian Research 288:23-38.
Zhou, C., G. Xie, K. McFadden, S. Xiao, and X. Yuan. 2007. The diversification and extinction of Doushantuo-Pertatataka acritarchs in South China: Causes and biostratigraphic significance. Geological Journal 42:229-262.
Zhu, M., M. Lu, J. Zhang, F. Zhao, G. Li, Y. Aihua, X. Zhao, and M. Zhao. 2013. Carbon isotope chemostratigraphy and sedimentary facies evolution of the Ediacaran Doushantuo Formation in western Hubei, South China. Precambrian Research 225:7-28.
Zhu, M., J. Zhang, and A. Yang. 2007. Integrated Ediacaran (Sinian) chronostratigraphy of South China. Palaeogeography, Palaeoclimatology, Palaeoecology 254(1):7-61.

Appendices

Appendix A. Matlab Code Used in Chapter 1.

CurveXYpntsNstd300

Model Inputs:

rng=# of model runs used to generate mean species richness, assemblage evenness and average specimen size

SpecSzDmlst= Nx6 sized matrix where each column =1 individual and columns contain information on species identity, size and dimensions.

Sizetax= Matrix of aspect ratios. Species linked to aspect ratios via a position in the matrix recorded within the SpecSzDmlst matrix.

S= number of specimens within a populated volume.

Msizecasts= Matrix of size values (in mm). Species linked to aspect ratios via a position in the matrix recorded within the SpecSzDmlst matrix.

v= dimensions of populated volume (in cm).

ix,iy=inputs used in Raup shell model, held constant.

Numh=number of slices through each populated volume.

om= Number of specimens within one bulk sample.

```
function [Rchpnts,Evpnts,Szpnts] =
CurveXYpntsNstd300(rng,SpecSzDmlst,Sizetax,S,Msizecats,v,ix,iy,numh)
%UNTITLED6 Summary of this function goes here
%--------------------------------------------------
om=1;

Rchpntspre=zeros(1,30);
Rchmaxpre=zeros(1,30);
Rchminpre=zeros(1,30);
Evpntspre=zeros(1,30);
Evmaxpre=zeros(1,30);
Evminpre=zeros(1,30);
Szpntspre=zeros(1,30);
Szmaxpre=zeros(1,30);
Szminpre=zeros(1,30);
while om<(31)
[Rchout,Evout,Szout] =
AltNestedLSd((om*10),rng,SpecSzDmlst,Sizetax,S,Msizecats,v,ix,iy,numh);
Rchpntspre(1,om)=sum(Rchout)/rng;
Rchmaxpre(1,om)=max(Rchout);
Rchminpre(1,om)=min(Rchout);
Evpntspre(1,om)=sum(Evout)/rng;
Evmaxpre(1,om)=max(Evout);
Evminpre(1,om)=min(Evout);
Szpntspre(1,om)=sum(Szout)/rng;
Szmaxpre(1,om)=max(Szout);
Szminpre(1,om)=min(Szout);
om=om+1
end
Rchpnts=zeros(3,30);
Evpnts=zeros(3,30);
Szpnts=zeros(3,30);
```

```
Rchpnts(1,:)=Rchpntspre;
Rchpnts(2,:)=Rchmaxpre;
Rchpnts(3,:)=Rchminpre;
Evpnts(1,:)=Evpntspre;
Evpnts(2,:)=Evmaxpre;
Evpnts(3,:)=Evminpre;
Szpnts(1,:)=Szpntspre;
Szpnts(2,:)=Szmaxpre;
Szpnts(3,:)=Szminpre;
end
function [Rchout,Evout,Szout] =
AltNestedLSd(Sint,Snt,SpecSzDmlst,Sizetax,S,Msizecats,v,ix,iy,numh)
% This function is an alternate way of using BivGast
%to generate an intersected sample.
%-----------------------------------------------------
SizecatsB=Msizecats/10;
Evdist=zeros(1,Snt);
Rchdist=zeros(1,Snt);
Szdist=zeros(1,Snt);
tfo=1;
BaseinterMat=zeros(300,40);
while tfo<(Snt+1)
BaseinterMat=BaseinterMat-BaseinterMat;
jvb=1;
preProx=0;
%while jvb<(Sint+1)
 while jvb<(Sint)
[intersampB]=AltNestedLSpartA(Sint,SpecSzDmlst,Sizetax,S,Msizecats,v,ix,iy,nu
mh,preProx);
[As,Bs]=size(intersampB);
[Az,Bz]=size(BaseinterMat);
preProx;
tfo;
jvb;
%checkout=sum(sum(intersampB))+sum(sum(BaseinterMat));
%if checkout<Sint
BaseinterMat=BaseinterMat+intersampB;
%else

%end
jvb=sum(sum(BaseinterMat));
%preProx=jvb+preProx;
preProx=jvb;
end
[Rchness,AvgSzness,Evness] = RchEvSzcode(BaseinterMat,SizecatsB);
Rchdist(1,tfo)=Rchness;
Szdist(1,tfo)=AvgSzness;
Evdist(1,tfo)=Evness;
tfo=tfo+1;
end
Rchout=Rchdist;
Szout=Szdist;
Evout=Evdist;
end
function [intersampC] =
AltNestedLSpartA(Sint,SpecSzDmlst,Sizetax,S,Msizecats,v,ix,iy,numh,preProx)
% This function is an alternate way of using BivGast
```

```
%to generate an intersected sample.
%-----------------------------------------------------
hrznp=round(rand(numh)*v(1,2));
hrzn=hrznp(1,:);
[Finlist,wntthru,ovlapmat] =
BivGastLS_E(SpecSzDmlst,Sizetax,S,Msizecats,v,ix,iy);
[intersamp,addon,jhkout]=MulthorizonsBfrNst(S,Finlist,1,1,hrzn);%What if I
added a variable, preProx,plus code, that this function used to assess
whether the new intersect samp will push the total over Sint?
checkt=sum(jhkout(:,14))+preProx;
%if checkt>Sint
close=(addon+preProx);
jhkout;
if (addon+preProx)>Sint;
     [intersampVa] = AltExcessIndiv(jhkout,Sint,preProx);
     Vadd=sum(sum(intersampVa));
     intersampB=intersampVa;
%    [Dout]=ExcessIndivCodeb(jhkout,preProx,Sint);
%     intersampB=Dout;
else
    intersampB=intersamp;
end
intersampC=intersampB;
 %That variable would need to be fed in through all of partA
end

function [intersamp,addon,jhkout] =
MulthorizonsBfrNst(S,jhkb,Amatrw,Amatcol,hrzn)
%UNTITLED2 Summary of this function goes here
% This function generates coordinates for a logarithmic spiral line
%that will serve as the basis for code implementing Raup's coiling model.
%-------------------------------------------------------------------------
%[tax,gx]=size(Amat);
tax=Amatrw;
gx=Amatcol;
%intersamp=zeros(tax,(gx-1));
%intersamppre=zeros(200,40);
intersamppre=zeros(300,40);
p=1;
[szd,szhr]=size(hrzn);
while p<(szhr+1);
 leshrz=jhkb(:,11)<=hrzn(p);
 abovehrz=jhkb(:,10)>=hrzn(p);
 sect=leshrz .* abovehrz;
 %jhkb(:,13)=jhkb(:,13)+sect %Since col13 is now used to store the
 %dimensions key
 jhkb(:,14)=jhkb(:,14)+sect;
 [jhkR,jhkC]=size(jhkb);
 %for k=1:S
 jhkb;
  [intrz,intclz]=size(intersamppre);
  intrz;
  intclz;
  k=1;
  while k<(S+1)
      %k
     %if jhkb(k,13)==1
```

```
      if jhkb(k,14)==1

intersamppre(jhkb(k,1),jhkb(k,2))=intersamppre(jhkb(k,1),jhkb(k,2))+1; %the
replacement of jhkb(K,2)[formerly columns] with size categories may be a
problem. However this problem is resolved by realizing that the sizekeys are
keys to the 40 long SizematMay which is just the raw sizes. So just give
intersamp 40 columns.
         %Az=jhkb(k,1)*1000; %However, the above problem is resolved by
         %Bz=jhkb(k,2)*1000;
         %Az=jhkb(k,1);
         %Bz=jhkb(k,2);
         %intersamp(Az,Bz)=intersamp(jhkb(k,1),jhkb(k,2))+1;
     else
     end
     k=k+1;
 end
 jhkb(:,14)=jhkb(:,14)+sect;
 p=p+1;
end
intersamp=intersamppre;
addon=sum(sum(intersamp));
jhkout=jhkb;
end

function [Finlist,wntthru,ovlapmat] =
BivGastLS_E(SpecSzDmlst,Sizetax,S,Msizecats,v,ix,iy)
%UNTITLED12 Summary of this function goes here
%-------------------------------------------------------------
lenFullmat=length(SpecSzDmlst);
SpecSzDmlstout=SpecSzDmlst;
Sizecats=Msizecats/10;
subsamprnd=randperm(lenFullmat);
subsamppre=SpecSzDmlst(:,subsamprnd);
subsamp=subsamppre(:,1:S);
[d1,d2]=sort(subsamp(1,:));
subsampB=subsamp(:,d2);
[tsub,lensub]=size(subsampB);
[Xbv,Ybv,Zbv] = gensurfcordsC2(0,.1,10^14,ix,iy,1,.1);
%Xbv=Xbv/6;
%Ybv=Ybv/6;
%Zbv=Zbv/6;
subsampB;
lensub;
[Xgst,Ygst,Zgst] = gensurfcordsD2(.5,1,.2,ix,iy,8,.1);
pntb=subsampB(4,S);
%if subsampB(4,lensub)==1
if pntb==1
    XX=Xbv;
    YY=Ybv;
    ZZ=Zbv;
else
    XX=Xgst;
    YY=Ygst;
    ZZ=Zgst;
end
ta=(rand*v(1,1));
tb=(rand*v(1,2));
```

```
tc=(rand*v(1,3));
estabmat=zeros(S,14);
ovlapmat=zeros(S,S);
XXmoda=(XX*((Sizecats(1,subsampB(6,lensub)))))+tc;
YYmoda=((YY*((Sizecats(1,subsampB(6,lensub))*Sizetax(subsampB(2,lensub),2))))
)+tb; %changed from subsampB(3,value), how it is in most  code version back
when I'm referncing a row, to (2,value) to reference the dimension key
ZZmoda=((ZZ*((Sizecats(1,subsampB(6,lensub))*Sizetax(subsampB(2,lensub),3))))
)+ta;
maxya=max(max(YYmoda));
minya=min(min(YYmoda));
maxxa=max(max(XXmoda));
minxa=min(min(XXmoda));
maxza=max(max(ZZmoda));
minza=min(min(ZZmoda));
estabmat(1,1)=subsampB(3,S);
estabmat(1,2)= subsampB(6,S);
estabmat(1,13)=subsampB(2,S);
estabmat(1,3)=ta;
estabmat(1,4)=tb;
estabmat(1,5)=tc;
estabmat(1,6)=maxza;
estabmat(1,7)=minza;
estabmat(1,8)=maxxa;
estabmat(1,9)=minxa;
estabmat(1,10)=maxya;
estabmat(1,11)=minya;
estabmat(1,12)=subsampB(4,S);
%gonethrough=1;
jx=2;
wntthru=1;
while jx<(S+1)
    jx;
if subsampB(4,jx)==1
    XX=Xbv;
    YY=Ybv;
    ZZ=Zbv;
else
    XX=Xgst;
    YY=Ygst;
    ZZ=Zgst;
end
taa=(rand*v(1,1));
tba=(rand*v(1,2));
tca=(rand*v(1,3));
XXmoda=(XX*((Sizecats(1,subsampB(6,jx)))))+tca;
YYmoda=((YY*((Sizecats(1,subsampB(6,jx))*Sizetax(subsampB(2,jx),2)))))+tba;
%same change as above
ZZmoda=((ZZ*((Sizecats(1,subsampB(6,jx))*Sizetax(subsampB(2,jx),3)))))+taa;
maxy=max(max(YYmoda));
miny=min(min(YYmoda));
maxx=max(max(XXmoda));
minx=min(min(XXmoda));
maxz=max(max(ZZmoda));
minz=min(min(ZZmoda));
%st=lensub;
st=1;
```

```
cnt=0;
tht=0;
while st<jx;
   OvlpP1=0;
   OvlpP2=0;
   [OvlpP1] =
TradishCount16b(estabmat(st,8),estabmat(st,9),estabmat(st,10),estabmat(st,11)
,estabmat(st,6),estabmat(st,7),maxx,minx,maxy,miny,maxz,minz);
   [OvlpP2] =
TradishCount16b(maxx,minx,maxy,miny,maxz,minz,estabmat(st,8),estabmat(st,9),e
stabmat(st,10),estabmat(st,11),estabmat(st,6),estabmat(st,7));
   ovlapmat(S,jx)=ovlapmat(S,jx)+OvlpP1;
   ovlapmat(S,jx)=ovlapmat(S,jx)+OvlpP2;
   Ovlp=OvlpP1+OvlpP2;
    %if Ovlp==0
     if Ovlp<2
       tht=tht+1;
       %st=st-1;
    else
    end
       st=st+1;
end

%if tht==0
if tht<1;
estabmat(jx,1)=subsampB(3,jx);
estabmat(jx,2)= subsampB(6,jx);
estabmat(jx,13)=subsampB(2,jx);
estabmat(jx,3)=taa;
estabmat(jx,4)=tba;
estabmat(jx,5)=tca;
estabmat(jx,6)=maxz;
estabmat(jx,7)=minz;
estabmat(jx,8)=maxx;
estabmat(jx,9)=minx;
estabmat(jx,10)=maxy;
estabmat(jx,11)=miny;
estabmat(jx,12)=subsampB(4,jx);
%gonethrough=gonethrough+1;
%jx=jx-1;
%st=st-1;
jx=jx+1;
else
cnt=cnt+1;
end
if cnt>10000
%   disp('timed out')%I think the issue is that the disp needs to be outside
a loop. The loop needs to assign some variable a value and afterwards an if-
else loop assesses the value.
jx=0;
wntthru=0;
else
end
end
Finlist=estabmat;
end
```

```
function [X,Y,Z] = gensurfcordsC2(rc,T,W,ro,yo,lps,th)
%UNTITLED2 Summary of this function goes here
% This function generates coordinates for a logarithmic spiral line
%that will serve as the basis for code implementing Raup's coiling model.
%--------------------------------------------------------------------------
lpsb=lps*16;
Ab=(1:lpsb);
Aa=Ab/16;
A=Aa*360;

rtheta=zeros(lpsb,50);
ytheta=zeros(lpsb,50);
xrtheta=zeros(lpsb,50);
yrtheta=zeros(lpsb,50);

for y=1:50 %which of the ro starting points
    for t=1:lpsb%which position along the curve
       rtheta(t,y)=ro(1,y)*(W^((Aa(1,t))/(2*pi)));

ytheta(t,y)=yo(1,y)*(W^((Aa(1,t))/(2*pi)))+(rc*T*((W^((Aa(1,t))/(2*pi))))-1);
    end
end
for y=1:50 %which of the ro starting points
    for t=1:lpsb%which position along the curve
       xrtheta(t,y)=rtheta(t,y)*cos((A(1,t))*(pi/180));
       yrtheta(t,y)=rtheta(t,y)*sin((A(1,t))*(pi/180));
    end
end

X=(xrtheta*2.5)/-75;
Y=(yrtheta*-2.5)/20;
Z=(ytheta*-1*2.5)/75;

end

function [X,Y,Z] = gensurfcordsD2(rc,T,W,ro,yo,lps,th)
%UNTITLED2 Summary of this function goes here
% This function generates coordinates for a logarithmic spiral line
%that will serve as the basis for code implementing Raup's coiling model.
%--------------------------------------------------------------------------
lpsb=lps*16;
Ab=(1:lpsb);
Aa=Ab/16;
A=Aa*360;

rtheta=zeros(lpsb,50);
ytheta=zeros(lpsb,50);
xrtheta=zeros(lpsb,50);
yrtheta=zeros(lpsb,50);

for y=1:50 %which of the ro starting points
    for t=1:lpsb%which position along the curve
       rtheta(t,y)=ro(1,y)*(W^((Aa(1,t))/(2*pi)));
```

```
ytheta(t,y)=yo(1,y)*(W^((Aa(1,t))/(2*pi)))+(rc*T*((W^((Aa(1,t))/(2*pi))))-1);
    end
end
for y=1:50 %which of the ro starting points
    for t=1:lpsb%which position along the curve
       xrtheta(t,y)=rtheta(t,y)*cos((A(1,t))*(pi/180));
       yrtheta(t,y)=rtheta(t,y)*sin((A(1,t))*(pi/180));
    end
end

X=(xrtheta*2.5)*5/(50*th);
Y=(yrtheta*2.5)*5/(50*th);
Z=(ytheta*-1*2.5)*5/(50*th);
end
function [Ovlp] =
TradishCount16b(MaxXLG,MinXLG,MaxYLG,MinYLG,MaxZLG,MinZLG,MaxXsm,MinXsm,MaxYs
m,MinYsm,MaxZsm,MinZsm)
%This function checks for shell nesting
%-------------------------------------------------------
thb=0;
     if (MaxYsm>=MinYLG && MaxYLG>MaxYsm)|| (MaxYLG>=MinYsm &&
MaxYsm>MaxYLG)||(MaxYLG>=MaxYsm && MinYsm>=MinYLG);
                 if (MaxXsm>=MinXLG && MaxXLG>MaxXsm)|| (MaxXLG>=MinXsm &&
MaxXsm>MaxXLG)||(MaxXLG>=MaxXsm && MinXsm>=MinXLG);
                             if (MaxZsm>=MinZLG && MaxZLG>MaxZsm)||
(MaxZLG>=MinZsm && MaxZsm>MaxZLG)||(MaxZLG>=MaxZsm && MinZsm>=MinZLG);
                              thb=thb+1;
                             else
                             end
                 else
                 end
     else
     end
if thb>0
    Ovlp=0;
else
    Ovlp=1;%So 1 is good, 1 means they do not overlap
end
%surf(XXmodLG,ZZmodLG,YYmodLG)
%hold
%surf(XXmodsm,ZZmodsm,YYmodsm)
%hold
end

function [Dout] =ExcessIndivCodeb(Markedfinlist,preProx,Sint)
%This code takes the intersamp matrix with intersected specimens
%indicated and removes non-intersected specimens. This makes it possible to
%identify when Sint has been reached and adjust the output matrix
%accordingly.
%-----------------------------------------------------------------
p=Markedfinlist(:,14);
[l,j]=size(p);
intersectstat=zeros(l,1);
occupiedstat=zeros(l,1);
k=1;
```

```
while k<(l+1)
      %k
     %if jhkb(k,13)==1
     if Markedfinlist(k,14)>0
        intersectstat(k,1)=1;
     else
     end
     %if Markedfinlist(k,1)>0
     %    occupiedstat(k,1)=1;
     %else
     %end
     k=k+1;
end
 traninsect=transpose(intersectstat);
%rem=(1:l)*intersectstat;
rem=(1:l).*traninsect;
remb=rem(rem~=0);
[tg,addonb]=size(remb);
needadd=Sint-preProx;
remc=remb(1,(randperm(addonb)));
remd=remc(1,(1:needadd));
reme=sort(remd);
%Filledmrkedfinlist=Markedfinlist(remb,:);
%[ta,ts]=size(Filledmrkedfinlist);
%rearange=randperm(ta);
%C=Filledmrkedfinlist(rearange,:);
%Dout=C(1:(Sint-preProx),:);
intersamppre=zeros(200,40);
k=1;
 while k<(needadd+1)
      %k
     %if jhkb(k,13)==1

intersamppre(Markedfinlist((reme(k)),1),Markedfinlist((reme(k)),2))=intersamp
pre(Markedfinlist((reme(k)),1),Markedfinlist((reme(k)),2))+1; %the
replacement of jhkb(K,2)[formerly columns] with size categories may be a
problem. However this problem is resolved by realizing that the sizekeys are
keys to the 40 long SizematMay which is just the raw sizes. So just give
intersamp 40 columns.
         %Az=jhkb(k,1)*1000; %However, the above problem is resolved by
         %Bz=jhkb(k,2)*1000;
         %Az=jhkb(k,1);
         %Bz=jhkb(k,2);
         %intersamp(Az,Bz)=intersamp(jhkb(k,1),jhkb(k,2))+1;
     k=k+1;
 end
 Dout=intersamppre;

end

function [Rch,AvgSz,Ev] = RchEvSzcode(sectsamp,Sizecats)
%this function takes a matrix and calculates the richness, evenness and
%average size of the sample it represents.
%-------------------------------------------------------------------------
colsums=sum(sectsamp);
```

```
%[jb,hb]=size(sectsamp);%Now that I'm not using all 40 columns of the
intersamp matrix
rowsumsb=sum(transpose(sectsamp));%this is where the problem is coming from.
rowsums=rowsumsb;%There are only 9 entries in Sizecats, but the code is
trying
[jm,hx]=size(rowsums);%to go up to 40
[jb,hb]=size(Sizecats);

for ju=1:hx;
    if rowsums(ju)>0;
        rowsums(ju)=1;
    else
    end
end
Rch=sum(rowsums);
toh=0;
tjh=1;
while tjh<(hb+1);
    toh=toh+(colsums(tjh)*Sizecats(tjh));
    tjh=tjh+1;
end
AvgSz=toh/(sum(colsums));
totindiv=sum(rowsumsb);
pi=rowsumsb./totindiv;
lnpi=log(pi);
[bx,by]=size(lnpi);
tsz=bx*by;
for pup=1:tsz;
    if lnpi(pup)==-Inf;
        lnpi(pup)=0;
    else
    end
end
%Ev=lnpi;
preH=pi.*lnpi;
H=sum(preH)*-1;
Ev=H/(log(Rch));
end
function [intersampVa] = AltExcessIndiv(jhkmat,Sint,preProx)
%This function is an alternate way of randomly subsetting
%intersected specimens so that the total size of an intersected
%sample equals Sint
%-----------------------------------------------
[ta,tb]=size(jhkmat);
jhkmat;
TotIntN=sum(jhkmat(:,14));
Rowscheck=zeros(ta,2);
RowscheckA=jhkmat(:,14);
RowscheckB=transpose(1:ta);
vc=1;
while vc<(ta+1)
    if RowscheckA(vc,1)>1
       RowscheckA(vc,1)=1;
    else
    end
    vc=vc+1;
end
```

```
RowscheckA;
addnumb=Sint-preProx;
%tavect=transpose((1:ta));
%Intsectpre=tavect.*jhkmat(:,14);%This might be the problem, because jhkmat's
14 are not 1's, but 2's or 4's.
Intsectpre=RowscheckA.*RowscheckB;
Intsect=Intsectpre(Intsectpre~=0);
[za,zb]=size(Intsect);
arangd=randperm(za);
Intsectb=Intsect(arangd,:);
Intsectc=Intsectb((addnumb+1):za,:);
Intsectd=sort(Intsectc);
jhkmatV=jhkmat;
[tg,tf]=size(jhkmatV);
jhkmatV(Intsectd,14)=0;%This line is where something is going wrong
[ol,om]=size(jhkmatV);
jhkmatB=jhkmatV;
intersampV=zeros(300,40);
 k=1;
  while k<(ta+1)
      %k
     %if jhkb(k,13)==1
      %if jhkmatB(k,14)==1
     if jhkmatB(k,14)>0

intersampV(jhkmatB(k,1),jhkmatB(k,2))=intersampV(jhkmatB(k,1),jhkmatB(k,2))+1
; %the replacement of jhkb(K,2)[formerly columns] with size categories may be
a problem. However this problem is resolved by realizing that the sizekeys
are keys to the 40 long SizematMay which is just the raw sizes. So just give
intersamp 40 columns.
         %Az=jhkb(k,1)*1000; %However, the above problem is resolved by
         %Bz=jhkb(k,2)*1000;
         %Az=jhkb(k,1);
         %Bz=jhkb(k,2);
         %intersamp(Az,Bz)=intersamp(jhkb(k,1),jhkb(k,2))+1;
     else
     end
     k=k+1;
 end
intersampVa=intersampV;
end
```

Code for Random Draw Model

```
CurveXYpntsRand300


function [Rchpnts,Evpnts,Szpnts] =
CurveXYpntsRand300(rng,SpecSzDmlst,Sizetax,S,Msizecats,v,ix,iy,numh)
```

```
%UNTITLED6 Summary of this function goes here
%-----------------------------------------------------
om=1;

Rchpntspre=zeros(1,30);
Rchmaxpre=zeros(1,30);
Rchminpre=zeros(1,30);
Evpntspre=zeros(1,30);
Evmaxpre=zeros(1,30);
Evminpre=zeros(1,30);
Szpntspre=zeros(1,30);
Szmaxpre=zeros(1,30);
Szminpre=zeros(1,30);
while om<(31)
[Rchout,Evout,Szout] = NlistRchEvAvgSzRnd(SpecSzDmlst,Msizecats,(om*10),rng);
Rchpntspre(1,om)=sum(Rchout)/rng;
Rchmaxpre(1,om)=max(Rchout);
Rchminpre(1,om)=min(Rchout);
Evpntspre(1,om)=sum(Evout)/rng;
Evmaxpre(1,om)=max(Evout);
Evminpre(1,om)=min(Evout);
Szpntspre(1,om)=sum(Szout)/rng;
Szmaxpre(1,om)=max(Szout);
Szminpre(1,om)=min(Szout);
om=om+1
end
Rchpnts=zeros(3,30);
Evpnts=zeros(3,30);
Szpnts=zeros(3,30);
Rchpnts(1,:)=Rchpntspre;
Rchpnts(2,:)=Rchmaxpre;
Rchpnts(3,:)=Rchminpre;
Evpnts(1,:)=Evpntspre;
Evpnts(2,:)=Evmaxpre;
Evpnts(3,:)=Evminpre;
Szpnts(1,:)=Szpntspre;
Szpnts(2,:)=Szmaxpre;
Szpnts(3,:)=Szminpre;
end
function [Rchlsrnd,Evlsrnd,AvgSzlsrnd] =
NlistRchEvAvgSzRnd(Nlist,Sizecats,S,Snt)
%UNTITLED5 Summary of this function goes here
%-----------------------------------------------------------
Rchhold=zeros(1,Snt);
Evhold=zeros(1,Snt);
Szhold=zeros(1,Snt);
mo=1;
while mo<(Snt+1)
[po,fullen]=size(Nlist);
lk=randperm(fullen);
NlistB=Nlist(:,lk);
Nlistsub=NlistB(:,1:S);
[ty,sublen]=size(Nlistsub);
SpecIDcont=zeros(1,300);
Sizecont=zeros(1,40);
ju=1;
while ju<(sublen+1)
```

```
   SpecIDcont(1,Nlistsub(3,ju))=SpecIDcont(1,Nlistsub(3,ju))+1;
   Sizecont(1,Nlistsub(6,ju))=Sizecont(1,Nlistsub(6,ju))+1;
   ju=ju+1;
end
%Sizemax=max(Nlistsub(1,:));
%SpecIDmax=max(Nlistsub(3,:));
colsums=Sizecont;
%[jb,hb]=size(sectsamp);
jb=200;
%hb=40;
hb=length(Sizecats);
rowsumsb=SpecIDcont;
rowsums=rowsumsb;
[jm,hx]=size(rowsums);
for ju=1:hx;
    if rowsums(ju)>0;
        rowsums(ju)=1;
    else
    end
end
Rch=sum(rowsums);
toh=0;
tjh=1;
while tjh<(hb+1);
    toh=toh+(colsums(tjh)*Sizecats(tjh));
    tjh=tjh+1;
end
AvgSz=toh/(sum(colsums));
totindiv=sum(rowsumsb);
pi=rowsumsb./totindiv;
lnpi=log(pi);
[bx,by]=size(lnpi);
tsz=bx*by;
for pup=1:tsz;
    if lnpi(pup)==-Inf;
        lnpi(pup)=0;
    else
    end
end
%Ev=lnpi;
preH=pi.*lnpi;
H=sum(preH)*-1;
Ev=H/(log(Rch));
Rchhold(1,mo)=Rch;
Evhold(1,mo)=Ev;
Szhold(1,mo)=AvgSz;
mo=mo+1;
end
Rchlsrnd=Rchhold;
Evlsrnd=Evhold;
AvgSzlsrnd=Szhold;
end
```

Code for Preferential Intersection model outputting sets of raw data for a single sample size

```
function [RchpntsOut,EvpntsOut,SzpntsOut] =
CurveXYpntsNstdRawDat(rng,SpecSzDmlst,Sizetax,S,Msizecats,v,ix,iy,numh)
%UNTITLED6 Summary of this function goes here
%-----------------------------------------------------
om=1;
RchpntsOutpre=zeros(rng,1);
EvpntsOutpre=zeros(rng,1);
SzpntsOutpre=zeros(rng,1);
while om<(2)
[Rchout,Evout,Szout] =
AltNestedLSd((300),rng,SpecSzDmlst,Sizetax,S,Msizecats,v,ix,iy,numh);
%[Rchout,Evout,Szout] =
AltNestedLSd((10),rng,SpecSzDmlst,Sizetax,S,Msizecats,v,ix,iy,300);
RchpntsOutpre(:,om)=Rchout;
EvpntsOutpre(:,om)=Evout;
SzpntsOutpre(:,om)=Szout;
om=om+1
end
RchpntsOut=RchpntsOutpre;
EvpntsOut=EvpntsOutpre;
SzpntsOut=SzpntsOutpre;
end
function [Rchout,Evout,Szout] =
AltNestedLSd(Sint,Snt,SpecSzDmlst,Sizetax,S,Msizecats,v,ix,iy,numh)
% This function is an alternate way of using BivGast
%to generate an intersected sample.
%-----------------------------------------------------
SizecatsB=Msizecats/10;
Evdist=zeros(1,Snt);
Rchdist=zeros(1,Snt);
Szdist=zeros(1,Snt);
tfo=1;
BaseinterMat=zeros(300,40);
while tfo<(Snt+1)
BaseinterMat=BaseinterMat-BaseinterMat;
jvb=1;
preProx=0;
%while jvb<(Sint+1)
 while jvb<(Sint)
[intersampB]=AltNestedLSpartA(Sint,SpecSzDmlst,Sizetax,S,Msizecats,v,ix,iy,nu
mh,preProx);
[As,Bs]=size(intersampB);
[Az,Bz]=size(BaseinterMat);
preProx;
tfo;
jvb;
%checkout=sum(sum(intersampB))+sum(sum(BaseinterMat));
%if checkout<Sint
BaseinterMat=BaseinterMat+intersampB;
%else

%end
jvb=sum(sum(BaseinterMat));
%preProx=jvb+preProx;
preProx=jvb;
end
[Rchness,AvgSzness,Evness] = RchEvSzcode(BaseinterMat,SizecatsB);
```

```
Rchdist(1,tfo)=Rchness;
Szdist(1,tfo)=AvgSzness;
Evdist(1,tfo)=Evness;
tfo=tfo+1;
end
Rchout=Rchdist;
Szout=Szdist;
Evout=Evdist;
end
function [intersampC] =
AltNestedLSpartA(Sint,SpecSzDmlst,Sizetax,S,Msizecats,v,ix,iy,numh,preProx)
% This function is an alternate way of using BivGast
%to generate an intersected sample.
%-----------------------------------------------------
hrznp=round(rand(numh)*v(1,2));
hrzn=hrznp(1,:);
[Finlist,wntthru,ovlapmat] =
BivGastLS_E(SpecSzDmlst,Sizetax,S,Msizecats,v,ix,iy);
[intersamp,addon,jhkout]=MulthorizonsBfrNst(S,Finlist,1,1,hrzn);%What if I
added a variable, preProx,plus code, that this function used to assess
whether the new intersect samp will push the total over Sint?
checkt=sum(jhkout(:,14))+preProx;
%if checkt>Sint
close=(addon+preProx);
jhkout;
if (addon+preProx)>Sint;
     [intersampVa] = AltExcessIndiv(jhkout,Sint,preProx);
     Vadd=sum(sum(intersampVa));
     intersampB=intersampVa;
%    [Dout]=ExcessIndivCodeb(jhkout,preProx,Sint);
%     intersampB=Dout;
else
    intersampB=intersamp;
end
intersampC=intersampB;
 %That variable would need to be fed in through all of partA
end

function [intersamp,addon,jhkout] =
MulthorizonsBfrNst(S,jhkb,Amatrw,Amatcol,hrzn)
%UNTITLED2 Summary of this function goes here
% This function generates coordinates for a logarithmic spiral line
%that will serve as the basis for code implementing Raup's coiling model.
%-------------------------------------------------------------------------
%[tax,gx]=size(Amat);
tax=Amatrw;
gx=Amatcol;
%intersamp=zeros(tax,(gx-1));
%intersamppre=zeros(200,40);
intersamppre=zeros(300,40);
p=1;
[szd,szhr]=size(hrzn);
while p<(szhr+1);
 leshrz=jhkb(:,11)<=hrzn(p);
 abovehrz=jhkb(:,10)>=hrzn(p);
 sect=leshrz .* abovehrz;
 %jhkb(:,13)=jhkb(:,13)+sect %Since col13 is now used to store the
```

```
 %dimensions key
 jhkb(:,14)=jhkb(:,14)+sect;
 [jhkR,jhkC]=size(jhkb);
 %for k=1:S
 jhkb;
  [intrz,intclz]=size(intersamppre);
  intrz;
  intclz;
  k=1;
  while k<(S+1)
      %k
     %if jhkb(k,13)==1
      if jhkb(k,14)==1

intersamppre(jhkb(k,1),jhkb(k,2))=intersamppre(jhkb(k,1),jhkb(k,2))+1; %the
replacement of jhkb(K,2)[formerly columns] with size categories may be a
problem. However this problem is resolved by realizing that the sizekeys are
keys to the 40 long SizematMay which is just the raw sizes. So just give
intersamp 40 columns.
          %Az=jhkb(k,1)*1000; %However, the above problem is resolved by
          %Bz=jhkb(k,2)*1000;
          %Az=jhkb(k,1);
          %Bz=jhkb(k,2);
          %intersamp(Az,Bz)=intersamp(jhkb(k,1),jhkb(k,2))+1;
     else
     end
     k=k+1;
 end
 jhkb(:,14)=jhkb(:,14)+sect;
 p=p+1;
end
intersamp=intersamppre;
addon=sum(sum(intersamp));
jhkout=jhkb;
end

function [Finlist,wntthru,ovlapmat] =
BivGastLS_E(SpecSzDmlst,Sizetax,S,Msizecats,v,ix,iy)
%UNTITLED12 Summary of this function goes here
%-------------------------------------------------------------
lenFullmat=length(SpecSzDmlst);
SpecSzDmlstout=SpecSzDmlst;
Sizecats=Msizecats/10;
subsamprnd=randperm(lenFullmat);
subsamppre=SpecSzDmlst(:,subsamprnd);
subsamp=subsamppre(:,1:S);
[d1,d2]=sort(subsamp(1,:));
subsampB=subsamp(:,d2);
[tsub,lensub]=size(subsampB);
[Xbv,Ybv,Zbv] = gensurfcordsC2(0,.1,10^14,ix,iy,1,.1);
%Xbv=Xbv/6;
%Ybv=Ybv/6;
%Zbv=Zbv/6;
subsampB;
lensub;
[Xgst,Ygst,Zgst] = gensurfcordsD2(.5,1,.2,ix,iy,8,.1);
pntb=subsampB(4,S);
```

```
%if subsampB(4,lensub)==1
if pntb==1
    XX=Xbv;
    YY=Ybv;
    ZZ=Zbv;
else
    XX=Xgst;
    YY=Ygst;
    ZZ=Zgst;
end
ta=(rand*v(1,1));
tb=(rand*v(1,2));
tc=(rand*v(1,3));
estabmat=zeros(S,14);
ovlapmat=zeros(S,S);
XXmoda=(XX*((Sizecats(1,subsampB(6,lensub)))))+tc;
YYmoda=((YY*((Sizecats(1,subsampB(6,lensub))*Sizetax(subsampB(2,lensub),2))))
)+tb; %changed from subsampB(3,value), how it is in most  code version back
when I'm referncing a row, to (2,value) to reference the dimension key
ZZmoda=((ZZ*((Sizecats(1,subsampB(6,lensub))*Sizetax(subsampB(2,lensub),3))))
)+ta;
maxya=max(max(YYmoda));
minya=min(min(YYmoda));
maxxa=max(max(XXmoda));
minxa=min(min(XXmoda));
maxza=max(max(ZZmoda));
minza=min(min(ZZmoda));
estabmat(1,1)=subsampB(3,S);
estabmat(1,2)= subsampB(6,S);
estabmat(1,13)=subsampB(2,S);
estabmat(1,3)=ta;
estabmat(1,4)=tb;
estabmat(1,5)=tc;
estabmat(1,6)=maxza;
estabmat(1,7)=minza;
estabmat(1,8)=maxxa;
estabmat(1,9)=minxa;
estabmat(1,10)=maxya;
estabmat(1,11)=minya;
estabmat(1,12)=subsampB(4,S);
%gonethrough=1;
jx=2;
wntthru=1;
while jx<(S+1)
    jx;
if subsampB(4,jx)==1
    XX=Xbv;
    YY=Ybv;
    ZZ=Zbv;
else
    XX=Xgst;
    YY=Ygst;
    ZZ=Zgst;
end
taa=(rand*v(1,1));
tba=(rand*v(1,2));
tca=(rand*v(1,3));
```

```
XXmoda=(XX*((Sizecats(1,subsampB(6,jx)))))+tca;
YYmoda=((YY*((Sizecats(1,subsampB(6,jx))*Sizetax(subsampB(2,jx),2)))))+tba;
%same change as above
ZZmoda=((ZZ*((Sizecats(1,subsampB(6,jx))*Sizetax(subsampB(2,jx),3)))))+taa;
maxy=max(max(YYmoda));
miny=min(min(YYmoda));
maxx=max(max(XXmoda));
minx=min(min(XXmoda));
maxz=max(max(ZZmoda));
minz=min(min(ZZmoda));
%st=lensub;
st=1;
cnt=0;
tht=0;
while st<jx;
   OvlpP1=0;
   OvlpP2=0;
   [OvlpP1] =
TradishCount16b(estabmat(st,8),estabmat(st,9),estabmat(st,10),estabmat(st,11)
,estabmat(st,6),estabmat(st,7),maxx,minx,maxy,miny,maxz,minz);
   [OvlpP2] =
TradishCount16b(maxx,minx,maxy,miny,maxz,minz,estabmat(st,8),estabmat(st,9),e
stabmat(st,10),estabmat(st,11),estabmat(st,6),estabmat(st,7));
   ovlapmat(S,jx)=ovlapmat(S,jx)+OvlpP1;
   ovlapmat(S,jx)=ovlapmat(S,jx)+OvlpP2;
   Ovlp=OvlpP1+OvlpP2;
    %if Ovlp==0
     if Ovlp<2
       tht=tht+1;
       %st=st-1;
    else
    end
       st=st+1;
end

%if tht==0
if tht<1;
estabmat(jx,1)=subsampB(3,jx);
estabmat(jx,2)= subsampB(6,jx);
estabmat(jx,13)=subsampB(2,jx);
estabmat(jx,3)=taa;
estabmat(jx,4)=tba;
estabmat(jx,5)=tca;
estabmat(jx,6)=maxz;
estabmat(jx,7)=minz;
estabmat(jx,8)=maxx;
estabmat(jx,9)=minx;
estabmat(jx,10)=maxy;
estabmat(jx,11)=miny;
estabmat(jx,12)=subsampB(4,jx);
%gonethrough=gonethrough+1;
%jx=jx-1;
%st=st-1;
jx=jx+1;
else
cnt=cnt+1;
end
```

```
if cnt>10000
%   disp('timed out')%I think the issue is that the disp needs to be outside
a loop. The loop needs to assign some variable a value and afterwards an if-
else loop assesses the value.
jx=0;
wntthru=0;
else
end
end
Finlist=estabmat;
end

function [X,Y,Z] = gensurfcordsC2(rc,T,W,ro,yo,lps,th)
%UNTITLED2 Summary of this function goes here
% This function generates coordinates for a logarithmic spiral line
%that will serve as the basis for code implementing Raup's coiling model.
%--------------------------------------------------------------------------
lpsb=lps*16;
Ab=(1:lpsb);
Aa=Ab/16;
A=Aa*360;

rtheta=zeros(lpsb,50);
ytheta=zeros(lpsb,50);
xrtheta=zeros(lpsb,50);
yrtheta=zeros(lpsb,50);

for y=1:50 %which of the ro starting points
    for t=1:lpsb%which position along the curve
       rtheta(t,y)=ro(1,y)*(W^((Aa(1,t))/(2*pi)));

ytheta(t,y)=yo(1,y)*(W^((Aa(1,t))/(2*pi)))+(rc*T*((W^((Aa(1,t))/(2*pi))))-1);
    end
end
for y=1:50 %which of the ro starting points
    for t=1:lpsb%which position along the curve
       xrtheta(t,y)=rtheta(t,y)*cos((A(1,t))*(pi/180));
       yrtheta(t,y)=rtheta(t,y)*sin((A(1,t))*(pi/180));
    end
end

X=(xrtheta*2.5)/-75;
Y=(yrtheta*-2.5)/20;
Z=(ytheta*-1*2.5)/75;

end

function [X,Y,Z] = gensurfcordsD2(rc,T,W,ro,yo,lps,th)
%UNTITLED2 Summary of this function goes here
% This function generates coordinates for a logarithmic spiral line
%that will serve as the basis for code implementing Raup's coiling model.
%--------------------------------------------------------------------------
lpsb=lps*16;
Ab=(1:lpsb);
Aa=Ab/16;
A=Aa*360;
```

```
rtheta=zeros(lpsb,50);
ytheta=zeros(lpsb,50);
xrtheta=zeros(lpsb,50);
yrtheta=zeros(lpsb,50);

for y=1:50 %which of the ro starting points
    for t=1:lpsb%which position along the curve
       rtheta(t,y)=ro(1,y)*(W^((Aa(1,t))/(2*pi)));

ytheta(t,y)=yo(1,y)*(W^((Aa(1,t))/(2*pi)))+(rc*T*((W^((Aa(1,t))/(2*pi))))-1);
    end
end
for y=1:50 %which of the ro starting points
    for t=1:lpsb%which position along the curve
       xrtheta(t,y)=rtheta(t,y)*cos((A(1,t))*(pi/180));
       yrtheta(t,y)=rtheta(t,y)*sin((A(1,t))*(pi/180));
    end
end

X=(xrtheta*2.5)*5/(50*th);
Y=(yrtheta*2.5)*5/(50*th);
Z=(ytheta*-1*2.5)*5/(50*th);
end
function [Ovlp] =
TradishCount16b(MaxXLG,MinXLG,MaxYLG,MinYLG,MaxZLG,MinZLG,MaxXsm,MinXsm,MaxYs
m,MinYsm,MaxZsm,MinZsm)
%This function checks for shell nesting
%-------------------------------------------------------
thb=0;
     if (MaxYsm>=MinYLG && MaxYLG>MaxYsm)|| (MaxYLG>=MinYsm &&
MaxYsm>MaxYLG)||(MaxYLG>=MaxYsm && MinYsm>=MinYLG);
                if (MaxXsm>=MinXLG && MaxXLG>MaxXsm)|| (MaxXLG>=MinXsm &&
MaxXsm>MaxXLG)||(MaxXLG>=MaxXsm && MinXsm>=MinXLG);
                            if (MaxZsm>=MinZLG && MaxZLG>MaxZsm)||
(MaxZLG>=MinZsm && MaxZsm>MaxZLG)||(MaxZLG>=MaxZsm && MinZsm>=MinZLG);
                             thb=thb+1;
                            else
                            end
                else
                end
     else
     end
if thb>0
    Ovlp=0;
else
    Ovlp=1;%So 1 is good, 1 means they do not overlap
end
%surf(XXmodLG,ZZmodLG,YYmodLG)
%hold
%surf(XXmodsm,ZZmodsm,YYmodsm)
%hold
end

function [Dout] =ExcessIndivCodeb(Markedfinlist,preProx,Sint)
%This code takes the intersamp matrix with intersected specimens
```

```
%indicated and removes non-intersected specimens. This makes it possible to
%identify when Sint has been reached and adjust the output matrix
%accordingly.
%-----------------------------------------------------------------
p=Markedfinlist(:,14);
[l,j]=size(p);
intersectstat=zeros(l,1);
occupiedstat=zeros(l,1);
k=1;
while k<(l+1)
      %k
     %if jhkb(k,13)==1
     if Markedfinlist(k,14)>0
        intersectstat(k,1)=1;
     else
     end
     %if Markedfinlist(k,1)>0
     %    occupiedstat(k,1)=1;
     %else
     %end
     k=k+1;
end
 traninsect=transpose(intersectstat);
%rem=(1:l)*intersectstat;
rem=(1:l).*traninsect;
remb=rem(rem~=0);
[tg,addonb]=size(remb);
needadd=Sint-preProx;
remc=remb(1,(randperm(addonb)));
remd=remc(1,(1:needadd));
reme=sort(remd);
%Filledmrkedfinlist=Markedfinlist(remb,:);
%[ta,ts]=size(Filledmrkedfinlist);
%rearange=randperm(ta);
%C=Filledmrkedfinlist(rearange,:);
%Dout=C(1:(Sint-preProx),:);
intersamppre=zeros(200,40);
k=1;
 while k<(needadd+1)
      %k
     %if jhkb(k,13)==1

intersamppre(Markedfinlist((reme(k)),1),Markedfinlist((reme(k)),2))=intersamp
pre(Markedfinlist((reme(k)),1),Markedfinlist((reme(k)),2))+1; %the
replacement of jhkb(K,2)[formerly columns] with size categories may be a
problem. However this problem is resolved by realizing that the sizekeys are
keys to the 40 long SizematMay which is just the raw sizes. So just give
intersamp 40 columns.
         %Az=jhkb(k,1)*1000; %However, the above problem is resolved by
         %Bz=jhkb(k,2)*1000;
         %Az=jhkb(k,1);
         %Bz=jhkb(k,2);
         %intersamp(Az,Bz)=intersamp(jhkb(k,1),jhkb(k,2))+1;
     k=k+1;
 end
 Dout=intersamppre;
```

```
end

function [Rch,AvgSz,Ev] = RchEvSzcode(sectsamp,Sizecats)
%this function takes a matrix and calculates the richness, evenness and
%average size of the sample it represents.
%-------------------------------------------------------------------------
colsums=sum(sectsamp);
%[jb,hb]=size(sectsamp);%Now that I'm not using all 40 columns of the
intersamp matrix
rowsumsb=sum(transpose(sectsamp));%this is where the problem is coming from.
rowsums=rowsumsb;%There are only 9 entries in Sizecats, but the code is
trying
[jm,hx]=size(rowsums);%to go up to 40
[jb,hb]=size(Sizecats);

for ju=1:hx;
    if rowsums(ju)>0;
        rowsums(ju)=1;
    else
    end
end
Rch=sum(rowsums);
toh=0;
tjh=1;
while tjh<(hb+1);
    toh=toh+(colsums(tjh)*Sizecats(tjh));
    tjh=tjh+1;
end
AvgSz=toh/(sum(colsums));
totindiv=sum(rowsumsb);
pi=rowsumsb./totindiv;
lnpi=log(pi);
[bx,by]=size(lnpi);
tsz=bx*by;
for pup=1:tsz;
    if lnpi(pup)==-Inf;
        lnpi(pup)=0;
    else
    end
end
%Ev=lnpi;
preH=pi.*lnpi;
H=sum(preH)*-1;
Ev=H/(log(Rch));
end
function [intersampVa] = AltExcessIndiv(jhkmat,Sint,preProx)
%This function is an alternate way of randomly subsetting
%intersected specimens so that the total size of an intersected
%sample equals Sint
%-----------------------------------------------
[ta,tb]=size(jhkmat);
jhkmat;
TotIntN=sum(jhkmat(:,14));
Rowscheck=zeros(ta,2);
RowscheckA=jhkmat(:,14);
RowscheckB=transpose(1:ta);
```

```
vc=1;
while vc<(ta+1)
    if RowscheckA(vc,1)>1
       RowscheckA(vc,1)=1;
    else
    end
    vc=vc+1;
end
RowscheckA;
addnumb=Sint-preProx;
%tavect=transpose((1:ta));
%Intsectpre=tavect.*jhkmat(:,14);%This might be the problem, because jhkmat's
14 are not 1's, but 2's or 4's.
Intsectpre=RowscheckA.*RowscheckB;
Intsect=Intsectpre(Intsectpre~=0);
[za,zb]=size(Intsect);
arangd=randperm(za);
Intsectb=Intsect(arangd,:);
Intsectc=Intsectb((addnumb+1):za,:);
Intsectd=sort(Intsectc);
jhkmatV=jhkmat;
[tg,tf]=size(jhkmatV);
jhkmatV(Intsectd,14)=0;%This line is where something is going wrong
[ol,om]=size(jhkmatV);
jhkmatB=jhkmatV;
intersampV=zeros(300,40);
 k=1;
  while k<(ta+1)
      %k
     %if jhkb(k,13)==1
      %if jhkmatB(k,14)==1
     if jhkmatB(k,14)>0

intersampV(jhkmatB(k,1),jhkmatB(k,2))=intersampV(jhkmatB(k,1),jhkmatB(k,2))+1
; %the replacement of jhkb(K,2)[formerly columns] with size categories may be
a problem. However this problem is resolved by realizing that the sizekeys
are keys to the 40 long SizematMay which is just the raw sizes. So just give
intersamp 40 columns.
         %Az=jhkb(k,1)*1000; %However, the above problem is resolved by
         %Bz=jhkb(k,2)*1000;
         %Az=jhkb(k,1);
         %Bz=jhkb(k,2);
         %intersamp(Az,Bz)=intersamp(jhkb(k,1),jhkb(k,2))+1;
     else
     end
     k=k+1;
 end
intersampVa=intersampV;
end
```

Code for Random Draw model outputting sets of raw data for a single sample size

RADsizedimdistribJuneD

```
function [RADSzDmMat] =
RADsizedimdistribJuneD(ConsolA,BDimlist,GDimlist,BSzlist,GSzlist,BGlist,BinSi
zeDist)
%This function brings together several subfunctions
%designed to go from the initial spread out numbers of species of different
%abundances to a subsample of size Nsub
%THIS IS THE CODE THAT ESTABLISHES the relationship between Dimlist,Szlist
and ExpSpecvect
%so the matrix this code generates needs to be saved.
%-------------------------------------------------
%[ConsolA] =ConverttoSpecFreq(ExpSpecvect);
[RADsampA] =ConverttoRankAbund(ConsolA);
lenRAD=length(RADsampA);
BDimrnd=randperm(1000000);
GDimrnd=randperm(1000000);
BSzrnd=randperm(1000000);
GSzrnd=randperm(1000000);
BGrnd=randperm(1000000);
%Abundrnd=randperm(lenRAD);
%[DimlistB] =MakeLonger(Dimlist,1000000);
[BDimlistB]=MakeLonger(BDimlist,1000000);
[GDimlistB]=MakeLonger(GDimlist,1000000);
[BSzlistB] =MakeLonger(BSzlist,1000000);
[GSzlistB] =MakeLonger(GSzlist,1000000);
[BGlistB] =MakeLonger(BGlist,1000000);
%DimlistC=DimlistB(Dimrnd);
BDimlistC=BDimlistB(BDimrnd);
GDimlistC=GDimlistB(GDimrnd);
BSzlistC=BSzlistB(BSzrnd);
GSzlistC=GSzlistB(GSzrnd)
BGlistC=BGlistB(BGrnd);
%DimlistD=DimlistC(1,1:lenRAD);
%SzlistD=SzlistC(1,1:lenRAD);
BGlistD=BGlistC(1,1:lenRAD);
%preRADszDmMat=zeros(4,lenRAD);
preRADszDmMat=zeros(5,lenRAD);
specIDs=(1:lenRAD);
preRADszDmMat(3,:)=RADsampA;
preRADszDmMat(4,:)=BGlistD;
preRADszDmMat(5,:)=specIDs;
NumbBiv=sum(BGlistD);
NumbGast=lenRAD-NumbBiv;
BDimlistD=BDimlistC(1,1:NumbBiv);
GDimlistD=GDimlistC(1,1:NumbGast);
BSzlistD=BSzlistC(1,1:NumbBiv);
GSzlistD=GSzlistC(1,1:NumbGast);
Bivplace=1;
Gastplace=1;
fk=1;
while fk<(lenRAD+1)
   if preRADszDmMat(4,fk)==1;
%preRADszDmMat(1,:)=BSzlistD(1,Bivplace);
%preRADszDmMat(2,:)=BDimlistD(1,Bivplace);
```

```
%preRADszDmMat(1,fk)=BSzlistD(1,Bivplace);
preRADszDmMat(2,fk)=BDimlistD(1,Bivplace);
Bivplace=Bivplace+1
   else
%preRADszDmMat(1,:)=GSzlistD(1,Gastplace);
%preRADszDmMat(2,:)=GDimlistD(1,Gastplace);
%preRADszDmMat(1,fk)=GSzlistD(1,Gastplace);
preRADszDmMat(2,fk)=GDimlistD(1,Gastplace);
Gastplace=Gastplace+1
   end
   fk=fk+1
end
preRADszDmMat(1,:)=BinSizeDist;
preRADszDmMatB=preRADszDmMat;
RADSzDmMat=preRADszDmMatB;
end
function [ConsolMat] =ConverttoSpecFreq(ExpecSpecFreq)
%UNTITLED6 Summary of this function goes here
%-------------------------------------------------------
S=round(sum(ExpecSpecFreq));
Len=length(ExpecSpecFreq);
Stormat=zeros(1,Len);
Wholemat=floor(ExpecSpecFreq);
ExpecSpecFreqB=ExpecSpecFreq-Wholemat;
jq=1;
%po=ExpecSpecFreq(1,1);
%while po>=1
 %   po=ExpecSpecFreq(1,jq);
  %  jq=jq+1;
%end
%This finds the first element in the matrix whose value is less than 1.
%jq=jq-1;
bp=jq;
Counter=0;
midpnt=0;
while bp<S
   if Counter==0
       lowbnd=bp;
   else
   end
   Counter=Counter+ExpecSpecFreqB(1,bp);
   if Counter>=1;
       midpnt=bp-round((bp-lowbnd)/2);
       Stormat(1,midpnt)=Stormat(1,midpnt)+1;
       Counter=Counter-1;
       lowbnd=bp;
   else
   end
   bp=bp+1;
end
ConsolMat=Stormat + Wholemat;
end
function [Rankabundout] =ConverttoRankAbund(Consolidated)
%This function converts the species frequencies generated by
%ConverttoSpecFreq to rank abundance data
%-------------------------------------------------------
vt=length(Consolidated);
```

```
Rankabundmat=zeros(1,(sum(Consolidated)));
Upbnda=Consolidated(1,1);
Rankabundmat(1,1:Upbnda)=1;
Specsofar=0;
Specsofar=Specsofar+Consolidated(1,1);
vj=2;
while vj<(vt+1);
    if Consolidated(1,vj)>0
        lwbnd=Specsofar+1;
        Specsofar=Specsofar+Consolidated(1,vj);
        Upbnd=Specsofar;
        Rankabundmat(1,lwbnd:Upbnd)=vj;
        vj=vj+1;
    else
        vj=vj+1;
    end
end
 Rankabundout=Rankabundmat;
end
function [PopOut] =ConvertRADtoNlist(RADsamp)
%This function converts the rank abundance data to an N-length
%list where the element value corresponds to the species ID
%and the number of occurrences of each value is equal to the species'
%abundance in the original RAD
%-----------------------------------------------------------
Ntot=sum(RADsamp);
Fullpop=zeros(1,Ntot);
Stot=length(RADsamp);
Totabund=RADsamp(1,1);
Highend=RADsamp(1,1);
Fullpop(1,1:Highend)=1;
Indivsofar=0;
Indivsofar=Indivsofar+RADsamp(1,1);
pj=2;
while pj<(Stot+1)
   lowend=Indivsofar+1;
   Indivsofar=Indivsofar+RADsamp(1,pj);
   Highend=Indivsofar;
   Fullpop(1,lowend:Highend)=pj;
   pj=pj+1;
end
PopOut=Fullpop;
end
function [SubsetDist] = Subsamplenorep(FullDist,SubN)
%This function takes a random subset of an N-length
%data set.
%-------------------------------------------
Ntot=length(FullDist);
FullDistB=FullDist(1,randperm(Ntot));
FullDistC=FullDistB(1,1:SubN);
SubsetDist=sort(FullDistC);
end
function [newRADC] = ConvertNlisttoRAD(Nlist)
%This function converts an N-length list of individual species identities
%into RAD format
%-------------------------------------------------
S=max(Nlist);
```

```
newRAD=zeros(1,S);
for jx=1:S
    newRAD(1,jx)=sum(Nlist(:)==jx);
end
newRADB=newRAD;
newRADC=sort(newRADB(newRADB~=0));
end
function [longmat] =MakeLonger(Dupmat,Xlen)
%UNTITLED11 Summary of this function goes here
%Both the size and dimensions portions of SpecSzDmlst
%should not be the sizes or dimensions themsleves but references
%to the appropriate rows in sizecats and sizetax
%--------------------------------------------------------
DupmatB=Dupmat;
h=1;
while h<(Xlen+1)
    DupmatB=[DupmatB,DupmatB];
    h=length(DupmatB);
end
longmat=DupmatB(:,1:Xlen);
end
```

ConverttoConsolRADb

```
function [ConsolRAD,TotA,TotB] =ConverttoConsolRADb(Spreadfi,S)
%UNTITLED6 Summary of this function goes here
%--------------------------------------------------------
ExpecSpecFreq=Spreadfi;
%S=round(sum(ExpecSpecFreq));
Len=length(ExpecSpecFreq);
Stormat=zeros(1,Len);
Wholemat=floor(ExpecSpecFreq);
ExpecSpecFreqB=ExpecSpecFreq-Wholemat;
jq=1;
%po=ExpecSpecFreq(1,1);
%while po>=1
 %   po=ExpecSpecFreq(1,jq);
  %  jq=jq+1;
%end
%This finds the first element in the matrix whose value is less than 1.
%jq=jq-1;
bp=1;
wolspec=sum(Wholemat);
Counter=0;
midpnt=0;
%while bp<S
 %while jq<(S+1)
 while jq<(Len+1)
   if Counter==0
       lowbnd=bp;
```

```
    else
    end
    Counter=Counter+ExpecSpecFreqB(1,bp);
    if Counter>=1;
        midpnt=bp-round((bp-lowbnd)/2);
        Stormat(1,midpnt)=Stormat(1,midpnt)+1;
        Counter=Counter-1;
        lowbnd=bp;
    else
    end
    %jq=sum(Stormat)+wolspec;
    jq=jq+1;
    bp=bp+1;
end
ConsolRADpre=Stormat + Wholemat;
abundcats=(1:1000000);
ConsolRADpreb=ConsolRADpre.*abundcats;
k=1;
jk=0;
while jk<(S+1)
jk=sum(ConsolRADpre(1,1:k));
k=k+1;
end
ConsolRAD=ConsolRADpre(1,1:k);
TotA=sum(ConsolRAD);
TotB=sum(ConsolRADpreb(1,1:k));
end
```

BasicLogSeriesA

```
function [ExpSpecLSpre] = BasicLogSeriesA(N,S,Alpha,X)
%UNTITLED3 Summary of this function goes here
%--------------------------------------------------------------------
%X=fminsearch(@(Xguess)FindFishersX(Alpha,N,Xguess),3);
PreX=ones(1,N);
PreV=(1:N);
Xvect=X.*PreX;
%XvectB=zeros(1,N);
XvectB=0;
%for jk=1:N
    %XvectB(1,jk)=Xvect(1,jk)^jk;
     %XvectB(1,jk)=Xvect.^PreV;
XvectB=Xvect.^PreV;
%end
XvectC=(Alpha*XvectB)./PreV;
jut=0;
jpt=1;
while jut<S
    %jpt=sum(XvectC(1,(1:jpt)));
    jut=jut+Xvect(1,jpt);
    jpt=jpt+1;
end
```

```
XvectD=XvectC(1,1:(jpt-1));
%ExpSpecLSpre=XvectD;
ExpSpecLSpre=XvectC;
end
function [AlphDiff] = FindFishersX(Alph,N,Xguess)
%This function calculates an estimated Alph using the formula
%alph=(N*(1-X))/X based on an initial guess of what
%X is. This estimate of Alph is then subtracted from the actual Alph, giving
% the value AlphDiff. This function can then be run through fminsearch to
% find the value of Alpha that minimizes the difference between Sest and S.
%out=fminsearch(@(Xguess)FindFishersX(Alph,N,Xguess),3)
%Above is the correct fminsearch format
%-------------------------------------------------------------------------
alphest=(N*(1-Xguess))/Xguess;
AlphDiff=abs(Alph-alphest);

end
```

LogNormRADGen

```
function [Abundlist,AbundlistB,AbundlistC] = LogNormRadGen(mupar,sigmpar,S,N)
%This code uses the inverse cumulative distribution function for the
%lognormal distribution to generate a RAD data set for the lognormal
%distribution
%X = logninv(P,mu,sigma)
%-------------------------------------------------------------------
incr=100/(S+1);
adj=incr/2;
Preabundlist=(1:S);
PreabundlistB=Preabundlist .* incr;
PreabundlistC=PreabundlistB+adj;
PreabundlistD=PreabundlistC./100;
Abundlist=zeros(1,S);
HB=1;
while HB<(S+1)
    X=logninv((PreabundlistD(1,HB)),mupar,sigmpar);
    Abundlist(1,HB)=X;
    HB=HB+1;
end
Abundlist;
Totlist=sum(Abundlist);
AbundlistB=Abundlist./Totlist;
AbundlistC=AbundlistB*N;

end
```

LSBivGastPrepJuneD

```
function [NlngSpecSzDmlst] = LSBivGastPrepJuneD(RADSzDmMat)
```

```
%This function brings together several subfunctions
%designed to go from the initial spread out numbers of species of different
%abundances to a subsample of size Nsub
%The relationship between Dimlist,Szlist and ExpSpecvect needs to be
%established prior to this code
%NOTE:SpecSzctsMat is an i column long matrix of size CATEGORIES, not size
values.
%Each column is a species and each row in a column corresponds to the size
%category that one individual of that species falls into. So the total
%number of occupied elements in that column will be equivalent to the total
%number of individuals of that species across samples.
%-------------------------------------------------
RADsampAb=RADSzDmMat(3,:);
RADsampA=RADSzDmMat(5,:);
Ntotb=sum(RADsampAb);
NlistSpecSzDm=zeros(6,Ntotb);
[PopOutA] =ConvertRADtoNlist(RADsampAb);
NlistSpecSzDm(3,:)=PopOutA;
for xu=1:Ntotb
    %NlistSpecSzDm(3,xu)=RADSzDmMat(3,PopOutA(1,xu));
    NlistSpecSzDm(2,xu)=RADSzDmMat(2,PopOutA(1,xu));
    NlistSpecSzDm(1,xu)=RADSzDmMat(1,PopOutA(1,xu));
    NlistSpecSzDm(4,xu)=RADSzDmMat(4,PopOutA(1,xu));
    NlistSpecSzDm(5,xu)=RADSzDmMat(5,PopOutA(1,xu));
    NlistSpecSzDm(6,xu)=RADSzDmMat(1,PopOutA(1,xu));
end
xb=1;
%while xb<(Ntotb+1)
%   RADSzDmMat(1,PopOutA(1,xb));
%   presix=rand*iszmat(1,RADSzDmMat(1,PopOutA(1,xb)));
%    sixent=round(presix);
%    if sixent<1
%        sixent=1;
%    else
%    end
%    sixent;
%    xb
%    NlistSpecSzDm(6,xb)=SpecSzctsMat(sixent,RADSzDmMat(1,PopOutA(1,xb)));
%    xb=xb+1;
%end




NlngSpecSzDmlst=NlistSpecSzDm;
end
function [ConsolMat] =ConverttoSpecFreq(ExpecSpecFreq)
%UNTITLED6 Summary of this function goes here
%-------------------------------------------------------
S=round(sum(ExpecSpecFreq));
Len=length(ExpecSpecFreq);
Stormat=zeros(1,Len);
Wholemat=floor(ExpecSpecFreq);
ExpecSpecFreqB=ExpecSpecFreq-Wholemat;
jq=1;
```

```
%po=ExpecSpecFreq(1,1);
%while po>=1
 %   po=ExpecSpecFreq(1,jq);
  %  jq=jq+1;
%end
%This finds the first element in the matrix whose value is less than 1.
%jq=jq-1;
bp=jq;
Counter=0;
midpnt=0;
while bp<S
   if Counter==0
       lowbnd=bp;
   else
   end
   Counter=Counter+ExpecSpecFreqB(1,bp);
   if Counter>=1;
       midpnt=bp-round((bp-lowbnd)/2);
       Stormat(1,midpnt)=Stormat(1,midpnt)+1;
       Counter=Counter-1;
       lowbnd=bp;
   else
   end
   bp=bp+1;
end
ConsolMat=Stormat + Wholemat;
end
function [Rankabundout] =ConverttoRankAbund(Consolidated)
%This function converts the species frequencies generated by
%ConverttoSpecFreq to rank abundance data
%-----------------------------------------------------------
vt=length(Consolidated);
Rankabundmat=zeros(1,(sum(Consolidated)));
Upbnda=Consolidated(1,1);
Rankabundmat(1,1:Upbnda)=1;
Specsofar=0;
Specsofar=Specsofar+Consolidated(1,1);
vj=2;
while vj<(vt+1);
    if Consolidated(1,vj)>0
        lwbnd=Specsofar+1;
        Specsofar=Specsofar+Consolidated(1,vj);
        Upbnd=Specsofar;
        Rankabundmat(1,lwbnd:Upbnd)=vj;
        vj=vj+1;
    else
        vj=vj+1;
    end
end
 Rankabundout=Rankabundmat;
end
function [PopOut] =ConvertRADtoNlist(RADsamp)
%This function converts the rank abundance data to an N-length
%list where the element value corresponds to the species ID
%and the number of occurrences of each value is equal to the species'
%abundance in the original RAD
%-----------------------------------------------------------
```

```
Ntot=sum(RADsamp);
Fullpop=zeros(1,Ntot);
Stot=length(RADsamp);
Totabund=RADsamp(1,1);
Highend=RADsamp(1,1);
Fullpop(1,1:Highend)=1;
Indivsofar=0;
Indivsofar=Indivsofar+RADsamp(1,1);
pj=2;
while pj<(Stot+1)
   lowend=Indivsofar+1;
   Indivsofar=Indivsofar+RADsamp(1,pj);
   Highend=Indivsofar;
   Fullpop(1,lowend:Highend)=pj;
   pj=pj+1;
end
PopOut=Fullpop;
end
function [SubsetDist] = Subsamplenorep(FullDist,SubN)
%This function takes a random subset of an N-length
%data set.
%-----------------------------------------------
Ntot=length(FullDist);
FullDistB=FullDist(1,randperm(Ntot));
FullDistC=FullDistB(1,1:SubN);
SubsetDist=sort(FullDistC);
end
function [newRADC] = ConvertNlisttoRAD(Nlist)
%This function converts an N-length list of individual species identities
%into RAD format
%-------------------------------------------------
S=max(Nlist);
newRAD=zeros(1,S);
for jx=1:S
    newRAD(1,jx)=sum(Nlist(:)==jx);
end
newRADB=newRAD;
newRADC=sort(newRADB(newRADB~=0));
end
```

Important inputs used with code above:

The following inputs were used with the code presented above. They were derived from the various literature sources described in the Methods section of Chapter 1 and described in more detail in Appendix II below.

BDimlistA

1 2 3 10 12 13 17 18 19 20 21 22 24
25 26 27 28 29 31 32 35 36 40

GDimlistA

4 5 6 7 8 9 11 14 15 16 23 30 33
34 37 38 39

BSzlistA

3 7 15 16 17 19 20 25

GSzlistA

1 2 4 5 6 8 9 10 11 12 13 14 18
21 22 23 24

BGlista

0 0 1 0 0 0 1 0 0 0 0 0 0
0 1 1 1 0 1 1 0 0 0 0 1

BinSizeDistJab2_39pre

2 3 3 4 4 4 4 5 5 5 6 6 6
6 7 7 7 8 8 8 8 8 9 9 9
9 9 10 10 10 11 11 11 11 12 12 12
13 13

BinSizeDistKowl_39pre

1 1 2 2 3 3 3 4 4 4 4 4 4
4 4 4 4 4 4 4 4 4 4 5 5
5 5 5 6 6 6 6 6 6 6 6 7
7 8

BinSizeDistSessa_39pre

1 1 1 1 2 2 2 2 3 3 3 3 4
4 4 4 4 4 4 4 5 5 5 5 6
6 6 6 6 7 7 8 8 8 9 9 9
10 10

BinSizeDistJab2_87pre

2 2 3 3 3 4 4 4 4 4 4 4 4
5 5 5 5 5 5 6 6 6 6 6 6
6 6 6 7 7 7 7 7 7 7 8 8
8 8 8 8 8 8 8 8 8 9 9 9
9 9 9 9 9 9 9 9 10 10 10 10
10 10 10 10 10 10 10 10 10 10 11 11
11 11 11 11 11 11 12 12 12 12 12 12
13 13

BinSizeDistKowl_87pre

1 1 1 1 2 2 2 2 2 3 3 3 3
3 3 3 4 4 4 4 4 4 4 4 4
4 4 4 4 4 4 4 4 4 4 4 4
4 4 4 4 4 4 4 4 4 4 4 4
4 4 5 5 5 5 5 5 5 5 5 5
5 5 5 6 6 6 6 6 6 6 6 6
6 6 6 6 6 6 6 6 6 7 7 7
8 8

BinSizeDistSessa_87pre

1 1 1 1 1 1 1 1 2 2 2 2 2
2 2 2 2 3 3 3 3 3 3 3 3
3 4 4 4 4 4 4 4 4 4 4 4
4 4 4 4 4 4 4 5 5 5 5 5
5 5 5 5 6 6 6 6 6 6 6 6
6 6 6 6 7 7 7 7 8 8 8 8
8 8 8 9 9 9 9 9 9 10 10 10
10 11

BinSizeDistJab2_50pre

1 2 3 4 4 4 4 4 5 5 5 5 6
6 6 6 6 7 7 7 7 8 8 8 8
8 8 9 9 9 9 9 9 9 10 10 10
10 11 11 11 11 11 11 12 12 12 12 13
13

BinSizeDistKowl_50pre

1 1 1 2 2 2 3 3 3 3 4 4 4
4 4 4 4 4 4 4 4 4 4 4 4
4 4 4 4 4 5 5 5 5 5 5 5
6 6 6 6 6 6 6 6 6 6 7 7
8

BinSizeDistSessa_50pre

1 1 1 1 2 2 2 2 2 3 3 3 3
3 4 4 4 4 4 4 4 4 4 4 5
5 5 5 5 6 6 6 6 6 6 6 7
7 8 8 8 8 9 9 9 9 10 10 10
11

TaxDimensions

1 0.00100000000000000 1

1 0.188571429000000 0.623134328000000

1 0.461000000000000 1.57333333300000

1 0.267415730000000 0.267415730000000

1 0.278431373000000 1

1 0.289099526000000 0.289099526000000

1 0.555205047000000 0.555205047000000

1 0.410071942000000 0.410071942000000

1 0.290969900000000 0.290969900000000

1 0.00100000000000000 1

1 1 1

1 0.409090909000000 1.05194805200000

1 0.0500000000000000 0.160000000000000

1 0.514195584000000 0.514195584000000

1 0.295275591000000 0.295275591000000

1 1 1

1 0.328143990000000 1.90909090900000

1 0.404494382000000 1.36516853900000

1 0.391644909000000 1.14621409900000

1 0.377777778000000 1.60740740700000

1 0.301369863000000 1.34246575300000

1 0.301369863000000 1.34246575300000

1 0.540816327000000 0.540816327000000

1 0.414814815000000 2.81512605000000

1 0.409090909000000 1.05194805200000

1 0.170124481000000 1

1 0.170124481000000 1

1 0.458333333000000 1.42708333300000

1 0.585585586000000 2.22522522500000

1 0.307167235000000 0.307167235000000

1 0.343434343000000 1.04040404000000

1 0.325714286000000 1.76000000000000

1 0.517751479000000 0.517751479000000

1 0.250000000000000 0.250000000000000

1 0.280254777000000 1.95555555600000

1 0.454545455000000 1.69930069900000

1 0.526315789000000 0.526315789000000

1 0.596153846000000 0.596153846000000

1 2 2

1 0.409090909000000 1.05194805200000

SizeCategories

2	2.82842712500000	4	5.65685424900000	8	11.3137085000000	16
	22.6274170000000	32	45.2548340000000	64	90.5096679900000	128
	181.019336000000	256				

Valtd:

[50,10,50]

# of slices=3;

These inputs were used as follows:

Valtd=v, used in function CurveXYpntsNstd300

SizeCategories = Msizecats, used in function CurveXYpntsNstd300

TaxDimensions=Sizetax, used in function CurveXYpntsNstd300

The data sets that begin with BinSizeDist all contain size values associated with species and correspond to one of the combinations of species abundance distribution (39 corresponds to Alph=3, 87 corresponds to Alph=6, 50 corresponds to the lognormal distribution. These numbers refer to the total number of species within the N sized sample) and size distribution (Jab, Kowl or Sessa). Values within these matrices correspond not directly to sizes themselves but to locations within the SizeCategories matrix. For example, an entry in a BinSizeDist matrix of ‘3’ means that htat species is associated with the size given in the ‘1x3’ position in the SizeCategories matrix.

Appendix B. In depth discussion of models used in Chapter 1

To explore the impact of preferential intersection on paleobiological sampling, we developed a simple model that captures the basic aspects of fossil sampling from lithified rock. The model in its simplest form consisted of a cubic volume with some number of fossil specimens distributed throughout the volume. This populated volume, which was analogous to a fossiliferous rock, was then bisected by one or more horizontal planes, corresponding to planar fractures, at random points along its vertical axis. Specimens that intersected one or more planes were considered exposed and were counted, contributing to the fossil sample. This process was then repeated until a user-defined sample size quota was reached.

In order to represent in Matlab the components of this model (i.e., the cubic volume, the bisecting planes, and the specimens distributed throughout the volume), they were reduced to simplified geometric forms that could be represented as sets of coordinates. This was straightforward for the rock volume and fracture surfaces. The rock volume was represented by eight sets of coordinates that together define the corners of a cubic volume. A single point on the vertical axis defined the two-dimensional plane that bisected this volume. The fossil contents, which in our model were mollusk shells, were more geometrically complex than simple cubes or planes but could also be represented as simplified geometric forms. To do this, we used Raup (1966)'s coiling model (Fig. 1). Raup's model is capable of replicating the shapes of a wide variety of molluscan shells using a parameterized equation. Briefly, Raup's model consists of a set of starting points placed around a circle with lines starting from these points coil around a vertical axis. The morphology of the resulting shell is controlled by the rate of whorl expansion (i.e., the rate at which radius of the circle around which the points are placed increases in size with coiling) and translation rate (i.e., the rate by which the circle shifts along the vertical axis relative to coiling

around the axis). Examples of model shells generated using our Matlab code written to implement Raup's model are shown in Figure 1. Using Raup's models we generated morphologies for a generic bivalve and gastropod that could then be modified to reflect differences between species in terms of size and shape and be distributed throughout the three-dimensional cubic volume. The Matlab implementation of our analog model therefore consisted of a cubic volume populated by specimens, all represented by sets of coordinates .

We first created nine parent populations of shells, from which specimens could be drawn at random to populate the cubic volumes. These nine parent populations represented different combinations of three species abundance distributions and three sources of species size data, which are described below. Each parent population contained 1,000,000 specimens to ensure an adequate sampling universe. These specimens represented different species that followed an abundance distribution. For simplicity, each species was defined by a distinct but uniform size and shape (i.e., there were inter-specific variations in size and shape, but there were no intra-specific variations). The model used shell height (i.e., distance from the dorsal to the ventral sides of specimens) as a measure of size.

Data on species abundances is commonly presented in the paleoecological literature, however these are usually limited to samples of only a few hundred or at best thousands of individuals. Therefore, in order to have a sampling universe sufficient to explore variation in diversity up to sample sizes of thousands of individuals, we chose to generate artificial data sets of size N = 1,000,000 based on realistic parameters. To do this, we used three species abundance distributions: two following the logseries distribution (Fisher et al. 1943) and one following the lognormal distribution (Bulmer 1974). In one of the logseries distributions, we set Fisher's alpha equal to 6, which yielded species richness-sample size relationship that was similar to those

observed in the studies of Sessa et al. (2009) and Hendy (2009). In the second logseries distribution, we used a Fisher's alpha value of 3, in order to examine the behavior of a less even and less species rich assemblage. For a given alpha value and a set number of individuals (N = 1,000,000), the logseries distribution predicts a specific species richness in the assemblage (i.e., 39 species when alpha = 3 and 87 species when alpha = 6). These species richness values correspond to the number of species that would be recovered if all 1,000,000 individuals were sampled.

We followed the methods of Wagner et al. (2006) in generating lognormally distributed distributions. Unlike the logseries distribution, the lognormal species abundance distribution does not specify a particular species richness associated with a particular set of parameters. Rather, a particular lognormal distribution specifies how species are distributed among abundance classes while the number of species within a particular lognormally distributed assemblage is a user-defined parameter. For our analyses, we generated lognormally distributed parent distributions with total species richness values of 50. These distributions yielded parent populations with richness values of the same order of magnitude as those produced by logseries distributions. Parameter values for the lognormal distribution were mu = 1.2281 and sigma = 1.2408.

Three sources of size data (Kowalewski et al. (2006), Roy et al. (2000), and Sessa et al. (2009)) formed the basis for constructing the parent populations with varying size between model species. The supplementary data set of Kowalewski et al. (2006) provided lists of specimens identified to species level with associated measurements of shell height. The mean of individual species provided a basis for a data set of species sizes. Roy et al. (2000) provided numbers of species assigned to different size bins. Sessa et al. (2009) provided lists of species taken from both her own work and previously published sources. While Sessa et al. (2009) did not provide species

size information, one of her sources of species abundance data, Garvie (1996), gave species-level size information including shell heights, width:height ratios, and length:height ratios. Measurements were given for the largest specimen of a species. This information was used as a source of size information for the species lists of Sessa et al. (2009).

Data on shell height were available in Kowalewski et al. (2006) and Sessa et al. (2009). However, Roy et al. (2000) recorded specimen size as the average of shell height and length. For the purposes of modeling, we chose to treat the Roy et al. (2000) size data as measurements of shell height. This means that the species size distribution referred to here as Roy et al. (2000) is not identical to what would have been produced had Roy et al. (2000) chosen to use only shell height as a measure of size. Since the Roy et al. (2000) data set covers a substantially larger size range than the two other data sets, analysis of these three data sets is potentially informative about how the distribution of species among size bin impacts the results of preferential intersection, — a primary goal of this study. Therefore, we chose to treat the size categories of the Roy et al. (2000) data set as if they represented shell height measurements in order to assess the impact of using a species size data set with these characteristics on model results.

We used the same binning scheme, $\log_2$, for all three size data sets. We then converted these binned species size data sets to lists of species size values for each of the three data sets. The number of times a size bin value occurred in a list corresponded to the number of species that fell in that size bin in that particular data set. We used the midpoint between $\log_2$ values as the cutoff point to determine which size bin a species went in, i.e. a species with a height of 35 mm would be placed in the size 32 bin while a species with a height of 39 mm would be placed in the 45.3 size bin. The sizes assigned to species corresponded to the value of the size bin, i.e. all species placed in the 32 mm bin were assigned a size of 32 mm. These lists of binned sizes served as the

basis for assigning size values to model species. The three binned size distributions are shown in Figure 7.

In contrast to specimen size, where we used three data sets to explore the effect of species size, only a single data set on shell shape was used for all analyses. This data set was generated by taking the species list of Sessa et al. (2009) and downloading data on measurements of shell height, width, and length from the Paleobiology database (retrieved May, 2016). The PBDB only presents measurements at the genus level, so the list of measurements was made at the genera level. Sets of measurements were then converted to aspect ratios by linearly scaling shell height to 1. For genera whose height-width-length data were not available in PBDB, width:height and length:height ratios were taken from Garvie (1996). See the list of inputs in Appendix I for the lists of sizes and dimensions used.

The compiled data of relative abundance, size, and shape were then used to generate parent populations from which specimens could be drawn to populate model rock volumes. To do this, the code first created a 5 × Sp matrix, where Sp equals the number of species in a particular parent population (i.e., 39 for logseries with alpha = 3; 87 for the logseries with alpha = 6; and 50 for the lognormal data set) and each column corresponds to a single species. The first row corresponds to species size and was filled by randomly selecting (without replacement) Sp values from the list of bin sizes. The second and third rows correspond to width:height and length:height ratios. These rows were similarly filled by randomly selecting (without replacement) Sp entries from the list of aspect ratios. The fourth row was set equal to species abundance values generated by the logseries or lognormal species abundance code. Entries in the fifth row were randomly assigned either 1 or 0, corresponding to bivalve or gastropod identity, respectively. Two thirds of species were labelled as gastropods while the rest were labelled as bivalves, similar to those observed in Kowalewski et

al. (2006). The sixth row contained ordered number entries from 1 to Sp, recording species identify. This 5 × Sp species-level matrix was then converted to a 5 × 1,000,000 specimen-level matrix using data in the third row (species abundance), with each column corresponding to an individual specimen in the parent population (N = 1,000,000).

Model rock volumes were populated by randomly drawing specimens, without replacement, from the parent distribution and then randomly assigning them locations in the rock volume (Figs. 2, 3B). The generic bivalve and gastropod shells created using the Raup model served as the basis for generating specimens of different species that varied in both size and shape. These generic model shells possess shell height, width, and length values of 1 mm. Therefore, in order to generate a specimen of a particular size, the generic set of coordinates were linearly scaled so that the specimen had a shell height equal to the size bin value assigned to its species. For simplicity, we chose to associate each species with only a single size value and ignored intraspecific size variation. Specimen shape was modified by the model in association with size modification. While the shell heights were scaled only by the size bin value, the shell lengths and widths were scaled additionally by the length or width aspect ratios, respectively. Again, for simplicity, each species was associated with only a single shape and intraspecific shape variation was ignored.

Model realism demands that the model should not allow bivalve and gastropod shells to occupy the same space and thus crosscut one another. It was therefore necessary for the code to identify instances of shell crosscutting as the volume was being populated with specimens and correct for this overlap. While the volume was being populated, the code compared each newly added specimen to each previously added specimen, in the order of their addition to the volume, to assess whether specimens overlapped in space. If the range of coordinates along the x, y, and z

axes of one specimen overlapped with that of any specimen previously placed in the volume, then the two specimens were considered to overlap. If the code detected overlap with any existing specimens, then the new-coming specimen was randomly assigned a new location in the volume and overlap was reassessed. This process was repeated until there was no overlap, at which point the code would move on to placing the next specimen. In order to handle situations where no more specimens could be placed in a volume without creating overlaps, the code monitored the number of failed attempts to place a specimen. If this number went above 10,000, the code would terminate attempts to place specimens, display a 'timed out' message, and set the output variable 'wntthru' equal to 0. Aborted volumes were not used in analyses.

Once the volume was populated by specimens, one or more positions along the vertical axis between the top and bottom of the volume were selected at random (Fig. 3C). These points represent fracture horizons. All specimens that intersected one or more of these horizons were counted by the code, and their species identity and associated information recorded. These specimens constituted the fossil sample collected from that volume of rock (Fig. 3D). The code recorded information about each intersected specimen, including its species identity and size, and recorded this information in a master list of sampled specimens. The code continued to generate and sample populated volumes until a user-supplied sample size quota was met. This quota represents the total sample size and is represented in the horizontal axis in Figures 4–6. In different model runs, the quotas were set at 10, 50, 100, 150, 200, 250, and 300 specimens, allowing us to examine the effects of different sample sizes on the magnitude of bias induced by preferential intersection.

For all but the smallest quotas, the number of specimens sampled from any one populated volume was below the quota. To reach this quota, the code therefore repeated the cycle of

populating and sampling a new volume, each time adding newly intersected specimens to the master list. This cycle was repeated until the total number of specimens on the master list was equal to the user-defined quota. It is important to understand the relationship among the total number of splits, the per-volume splitting intensity, and the sample size quota. The total number of splits is inherently related to the sample size quota, as any time a greater number of populated volumes were generated as demanded by the sample size quota, there would also be an increase in the total number of splits. The number of splits per populated volume, however, was set by the user to be equal to 3 for all model runs.

Because a splitting plane can intersect multiple specimens, the code must also deal with circumstances where the addition of the final set of intersected specimens overshoots the sampling quota. In such circumstances, the code assessed whether the sample size quota had been met following each sampling of a populated volume. If, after the addition of the newly intersected specimens, the total number of specimens on the master list was not greater than the quota, then the entire set of newly intersected specimens was added. However, if the intersected specimens in the final splitting were more than needed to reach the quota, then the code randomly selected only the number of specimens needed to meet the quota.

Once the quota was reached, the code calculated the species richness, evenness, and average specimen size of the sample. This was done using the information on species identity and size that was included in the entry for each intersected specimen in the master list. Calculation of species richness was straightforward and the code simply tallied the number of distinct species in the master list. For evenness, the code calculated Peilou's J (Pielou 1966), again based on the master list. For average specimen size, the code simply took the average size of all specimens on the master list regardless of species identity.

The procedure outlined above produced only a single set of values of species richness, evenness, and average specimen size for the generated bulk sample. This procedure was therefore repeated 150 times, and mean values and 95% confidence intervals for species richness, evenness, and mean specimen size were calculated based on the range of values yielded over the 150 model runs. This is straightforward for species richness and assemblage evenness. However, average specimen size merits further clarification. The code calculated the mean value of 150 average specimen size values, or the mean of means. The mean values and confidence intervals of species richness, evenness and average specimen size were calculated for each of the seven sample quotas examined in the model (Figs. 4–6).

As a null model to compare against the model of preferential intersection, we also wrote code to generate a random draw model. This model simply draws a quota of specimens at random from the same parent distribution used to populate the model volumes. This model is analogous to fossil collection by sieving unconsolidated sediments and retrieving all specimens contained within a given volume of sediments. A random draw model has previously been used to model fossil collection via sieving in a study of biases associated with choice of mesh size (Kowalewski and Hoffmeister 2003). Like the preferential intersection model, the random draw model was repeated 150 times for each quota size in order to calculate the mean and 95% confidence interval of species richness, evenness, and average specimen size.

The nine parent populations described above provided a basis for assessing how the magnitude of bias induced by preferential intersection varied in response to changes in the species abundance distribution and the distribution of species among size classes. Each parent population was run through both the preferential intersection and random draw models. The resulting curves of mean values and confidence intervals for species richness, assemblage evenness, and average

specimen size allowed us to examine how the magnitude of the bias changed with sample size for each combination of species abundance distribution and species size data set. We also performed one-tailed t-tests on sets of 150 values produced by the preferential intersection and random draw models, at a sample size of 300 specimens, to determine whether the two models produced significantly different richness, evenness, and average specimen size. T-tests were performed using the ‘t.test’ function in R.

Appendix C. Table of Microfossils from sections of the Doushantuo Formation

Sample	Measured Stratigraphic Height (m)	Corrected Stratigraphic Height(m)	Lithology	Taxon	Revised Universal Coordinates	England Finder Corrected	Label Position	Chert Reworked or Insitu?	Microfossils found
13SDP_DST2_1	8.75	10.9	sandy dolostone	*Siphonophycus robustum*	119.4_8.5, difficult to see below 40x	U20_1	Label to left	In-situ	yes
13SDP_DST2_2	11.5	14.4	sandy dolostone						no
13SDP_DST2_3	12	15	sandy dolostone						no
13SDP_DST2_4	14.2	17.75	sandy dolostone					Uncertain (insufficient features)	no
13SDP_DST2_5	15	18.75	sandy dolostone						no
S-19	19	19	sandy dolostone						no
13SDP_DST2_6	15.2	19	sandy dolostone						no
13SDP_DST2_7	15.7	19.625	sandy dolostone					In-situ	no
S-19.8	19.8	19.8	olistostrome breccia					Reworked	no
S-20.0	20	20	olistostrome breccia						no
S-20.3	20.3	20.3	olistostrome breccia						no
S-20.4_1	20.4	20.4	olistostrome breccia					Reworked	no
S-20.5	20.5	20.5	olistostrome breccia					Reworked	no
13SDP_DST2_8	16.4	20.5	olistostrome breccia					In-situ	no
S-20.6	20.6	20.6	olistostrome breccia					Reworked (?)	no
S-20.8	20.8	20.8	olistostrome breccia						no
S-21.1_1	21.1	21.1	olistostrome breccia	Unidentified Acritarch	133.9_14.3	Q34_1	Label to left	In-situ	yes
S-21.1_2	21.1	21.1	olistostrome breccia					In-situ	no
13SDP_DST2_9	17	21.2	olistostrome breccia					Reworked (?)	no
S-21.5	21.5	21.5	olistostrome breccia						no
13SDP_DST2_10	17.2	21.5	olistostrome breccia	*Siphonophycus robustum*	126.6_13.6	P26_2	Label to left	In-situ	yes
13SDP_DST2_10	17.2	21.5	olistostrome breccia	*Siphonophycus robustum*	125.3_5.7	n W25_3,W25_4,X	Label to left	In-situ	yes
13SDP_DST2_10	17.2	21.5	olistostrome breccia	*Siphonophycus robustum*	121.2_8.6	U21_1	Label to left	In-situ	yes
13SDP_DST2_10	17.2	21.5	olistostrome breccia	*Siphonophycus robustum*	114.9_13	P14_4	Label to left	In-situ	yes
13SDP_DST2_10	17.2	21.5	olistostrome breccia	*Siphonophycus robustum*	116.4_17.3	L16(center)	Label to left	In-situ	yes
13SDP_DST2_11	17.7	22.1	olistostrome breccia					In-situ	no
13SDP_DST2_13	19.1	23.9	olistostrome breccia	*Tianzushania spinosa* (?)	130_15.2	N30_2	Label to left	Reworked (?)	yes
13SDP_DST2_13	19.1	23.9	olistostrome breccia	Unidentified Acritarch	131.7_16	M31_4	Label to left	Reworked(?)	yes
S-27.2	27.2	27.2	olistostrome breccia						no

13SDP_DST2_14	26	28.7	olistostrome breccia					In-situ	no
13SDP_DST2_15	26.5	29.2	olistostrome breccia					In-situ	no
13SDP_DST2_16	27.5	30.3	olistostrome breccia					In-situ	no
13SDP_DST2_17	28.2	31.1	olistostrome breccia					In-situ	no
S-31.2	31.2	31.2	olistostrome breccia						no
13SDP_DST2_18	28.4	31.3	olistostrome breccia					Reworked	no
S-31.5	31.5	31.5	olistostrome breccia					In-situ	no
S-33.3_1	33.3	33.3	olistostrome breccia					Reworked (?)	no
S-33.3_2	33.3	33.3	olistostrome breccia					Reworked (?)	no
S-33.5	33.5	33.5	olistostrome breccia					Reworked	no
S-33.9	33.9	33.9	olistostrome breccia					Reworked	no
S-34.1	34.1	34.1	dolostone					In-situ	no
S-34.2	34.2	34.2	dolostone					Reworked	no
13SDP_DST2_19	33.5	35	dolostone	*Myxococoides sp.*	107.4_8.5	U7(center)	Label to left	Uncertain (insufficient features)	yes
13SDP_DST2_19	33.5	35	dolostone	*Myxococoides sp.*	107.7_8.3	U7_4	Label to left	Uncertain (insufficient features)	yes
13SDP_DST2_19	33.5	35	dolostone	*Siphonophycus typicum*	107.8_8.5	U7_2	Label to left	Uncertain (insufficient features)	yes
13SDP_DST2_19	33.5	35	dolostone	*Siphonophycus typicum*	117.8_8.6	U7_2	Label to left	Uncertain (insufficient features)	yes
13SDP_DST2_19	33.5	35	dolostone	*Siphonophycus typicum*	106.7_9.3	T6_4	Label to left	Uncertain (insufficient features)	yes
13SDP_DST2_19	33.5	35	dolostone	*Siphonophycus typicum*	107.5_20.4	H7(center)	Label to left	Uncertain (insufficient features)	yes
13SDP_DST2_19	33.5	35	dolostone	*Myxococoides sp.*	106.9_9.2	T7_3	Label to left	Uncertain (insufficient features)	yes
13SDP_DST2_19	33.5	35	dolostone	*Myxococoides sp.*	106.9_9.1	T7_3	Label to left	Uncertain (insufficient features)	yes
S-35.3	35.3	35.3	olistostrome breccia					In-situ	no
S-35.6	35.6	35.6	olistostrome breccia					Reworked(?)	no
13SDP_DST2_20	34.5	36	olistostrome breccia					In-situ	no
S-36.2_1	36.2	36.2	olistostrome breccia					In-situ	no
S-36.2_2	36.2	36.2	olistostrome breccia					Reworked	no
13SDP_DST2_21	34.7	36.3	olistostrome breccia					In-situ	no
S-37.1	37.1	37.1	olistostrome breccia					Reworked	no
S-37.4	37.4	37.4	olistostrome breccia	Unidentified Acritarch	161_18.9	J61_1	Label to left	Reworked	yes
13SDP_DST2_22	35.8	37.4	olistostrome breccia						no

13SDP_DST2_23	36.2	37.9	olistostrome breccia					Uncertain (insufficient features)	no
13SDP_DST2_24	36.5	38.2	olistostrome breccia					Reworked	no
S-38.9	38.9	38.9	dolostone						no
S-39.1	39.1	39.1	dolostone					In-situ	no
S-39.2	39.2	39.2	dolostone					In-situ	no
13SDP_DST2_25	37.5	39.2	dolostone					Reworked	no
S-39.4	39.4	39.4	dolostone						no
S-39.5	39.5	39.5	dolostone						no
S-39.6	39.6	39.6	dolostone					In-situ	no
13SDP_DST2_26	38	39.7	dolostone					In-situ	no
S-39.7	39.7	39.7	dolostone						no
S-39.9	39.9	39.9	dolostone					In-situ	no
S-40_1	40	40	dolostone					In-situ	no
S-40_2	40	40	dolostone					In-situ	no
S-40.05	40.05	40.05	dolostone					In-situ	no
S-40.25_1	40.25	40.25	dolostone					In-situ	no
S-40.25_2	40.25	40.25	dolostone					In-situ	no
S-40.3	40.3	40.3	dolostone					In-situ	no
S-40.35	40.35	40.35	dolostone					In-situ	no
13SDP_DST2_27	38.6	40.4	dolostone					In-situ	no
S-40.6	40.6	40.6	dolostone					In-situ	no
S-40.7	40.7	40.7	dolostone					In-situ	no
13SDP_DST2_28	39.1	40.9	dolostone	*Siphonophycus kestron*	138.8_15.3	N38_2	Label to left	In-situ	yes
13SDP_DST2_28	39.1	40.9	dolostone	*Siphonophycus robustum*	118.3_16.8	L18_3	Label to left	In-situ	yes
13SDP_DST2_28	39.1	40.9	dolostone	*Leiosphaeridia sp.*	111.9_23.3	E11_4	Label to left	In-situ	yes
13SDP_DST2_28	39.1	40.9	dolostone	*Leiosphaeridia sp.(?)*	135.7_19.2	J35_2	Label to left	In-situ	yes
13SDP_DST2_28	39.1	40.9	dolostone	*Leiosphaeridia sp.*	127.9_21	G27_4	Label to left	In-situ	yes
13SDP_DST2_28	39.1	40.9	dolostone	Unidentified Acritarch	124.6_15.5	N24_2	Label to left	In-situ	yes
13SDP_DST2_28	39.1	40.9	dolostone	*Siphonophycus kestron*	127.7_17	L27_2	Label to left	In-situ	yes
13SDP_DST2_28	39.1	40.9	dolostone	*Siphonophycus kestron*	108.8_18	K8_4	Label to left	In-situ	yes
13SDP_DST2_28	39.1	40.9	dolostone	*Siphonophycus robustum*	143_13.6	O43_3	Label to left	In-situ	yes
13SDP_DST2_28	39.1	40.9	dolostone	*Siphonophycus robustum*	136.5_13.9	Y36_1	Label to left	In-situ	yes
13SDP_DST2_28	39.1	40.9	dolostone	*Siphonophycus robustum*	141.1_15	N41_3	Label to left	In-situ	yes
13SDP_DST2_28	39.1	40.9	dolostone	*Siphonophycus robustum*	119.1_14.2	O19_3	Label to left	In-situ	yes
13SDP_DST2_28	39.1	40.9	dolostone	*Siphonophycus typicum*	111_14.6	O11_1	Label to left	In-situ	yes
13SDP_DST2_28	39.1	40.9	dolostone	*Siphonophycus robustum*	105.7_15.4	N5_4	Label to left	In-situ	yes
13SDP_DST2_28	39.1	40.9	dolostone	*Siphonophycus robustum*	132.3_15.9	M32_3	Label to left	In-situ	yes
13SDP_DST2_28	39.1	40.9	dolostone	*Siphonophycus robustum*	125.2_16.8	L25_3	Label to left	In-situ	yes
13SDP_DST2_28	39.1	40.9	dolostone	*Siphonophycus robustum*	138.4_16.7	L38_3	Label to left	In-situ	yes
13SDP_DST2_28	39.1	40.9	dolostone	*Siphonophycus robustum*	126.1_17.2	L26_1	Label to left	In-situ	yes

13SDP_DST2_28	39.1	40.9	dolostone	*Siphonophycus robustum*	115.6_18.3	K15_4	Label to left	In-situ	yes
13SDP_DST2_28	39.1	40.9	dolostone	*Siphonophycus robustum*	121.2_18.7	J21_3	Label to left	In-situ	yes
13SDP_DST2_28	39.1	40.9	dolostone	*Siphonophycus robustum*	110.2_18	K11(center)	Label to left	In-situ	yes
13SDP_DST2_28	39.1	40.9	dolostone	*Siphonophycus robustum*	132.8_21	G32_2	Label to left	In-situ	yes
13SDP_DST2_28	39.1	40.9	dolostone	*Siphonophycus robustum*	135.3_21.6	F35_3	Label to left	In-situ	yes
13SDP_DST2_28	39.1	40.9	dolostone	*Siphonophycus robustum*	135.2_22.6	E35_3	Label to left	In-situ	yes
13SDP_DST2_28	39.1	40.9	dolostone	*Siphonophycus typicum*	136.2_22.7	E36_3	Label to left	In-situ	yes
13SDP_DST2_28	39.1	40.9	dolostone	*Siphonophycus robustum*	134.8_22.9	E34_2	Label to left	In-situ	yes
13SDP_DST2_28	39.1	40.9	dolostone	*Siphonophycus robustum*	119.3_24	D19(center)	Label to left	In-situ	yes
13SDP_DST2_28	39.1	40.9	dolostone	*Siphonophycus robustum*	115.7_24.4	D15_2	Label to left	In-situ	yes
13SDP_DST2_28	39.1	40.9	dolostone	*Siphonophycus robustum*	106.4_17.2	L6_2	Label to left	In-situ	yes
13SDP_DST2_28	39.1	40.9	dolostone	*Siphonophycus robustum*	117.5_17.3	L17_2	Label to left	In-situ	yes
13SDP_DST2_28	39.1	40.9	dolostone	*Siphonophycus robustum*	140.7_22.8	E40_2	Label to left	In-situ	yes
13SDP_DST2_28	39.1	40.9	dolostone	*Unidentified Acritarch*	105.6_15	N5_4	Label to left	In-situ	yes
13SDP_DST2_29	39.1	41.3	dolostone					In-situ	no
S-41.4	41.4	41.4	dolostone					In-situ	no
S-41.5	41.5	41.5	dolostone					In-situ	no
S-41.6_1	41.6	41.6	dolostone	*Siphonophycus robustum*	140_21.3	F40_3	Label to left	In-situ	yes
S-41.6_1	41.6	41.6	dolostone	*Siphonophycus robustum*	141.9_21.3	F42_3	Label to left	In-situ	yes
S-41.6_1	41.6	41.6	dolostone	*Siphonophycus robustum*	122.4_21.5	F22_4	Label to left	In-situ	yes
S-41.6_1	41.6	41.6	dolostone	*Siphonophycus robustum*	128.8_21.7	F28_3	Label to left	In-situ	yes
S-41.6_1	41.6	41.6	dolostone	*Siphonophycus robustum*	149.6_21.8	F49_2	Label to left	In-situ	yes
S-41.6_1	41.6	41.6	dolostone	*Siphonophycus robustum*	151.4_21.7, difficult to see below 40x	F51_2	Label to left	In-situ	yes
S-41.6_1	41.6	41.6	dolostone	*Siphonophycus robustum*	150.4_21.8	F50_2	Label to left	In-situ	yes
S-41.6_1	41.6	41.6	dolostone	*Siphonophycus robustum*	150.3_21.8	F50_1	Label to left	In-situ	yes
S-41.6_1	41.6	41.6	dolostone	*Leiosphaeridia sp.*	148.5_21.9	F48_2	Label to left	In-situ	yes
S-41.6_1	41.6	41.6	dolostone	*Hocosphaeridium anozos*	132.8_5.5	F32_2	Label to left	In-situ	yes
S-41.6_2	41.6	41.6	dolostone	*Siphonophycus robustum*	156.9_21	G57_1	Label to left	In-situ	yes
S-41.6_2	41.6	41.6	dolostone	*Hocosphaeridium anozos*	143.5_21.2	G43_2	Label to left	In-situ	yes
S-41.6_3	41.6	41.6	dolostone	Unidentified Acritarch	136.1_17	L36_1	Label to left	In-situ	yes
S-41.6_3	41.6	41.6	dolostone	*Siphonophycus typicum*	131.9_7.7	U32_3	Label to left	In-situ	yes
S-41.6_3	41.6	41.6	dolostone	*Siphonophycus robustum*	131.9_8.6	T32_3	Label to left	In-situ	yes
S-41.6_3	41.6	41.6	dolostone	*Siphonophycus robustum*	136.4_19.1	J36_2	Label to left	In-situ	yes
S-41.6_3	41.6	41.6	dolostone	*Hocosphaeridium anozos*	131.1_7.6	U31_3	Label to left	In-situ	yes
S-41.6_3	41.6	41.6	dolostone	*Siphonophycus kestron (?)*	140.6_6	W40_2	Label to left	In-situ	yes
S-41.6_3	41.6	41.6	dolostone	*Siphonophycus kestron*	134.6_8	U34_2	Label to left	In-situ	yes
S-41.6_3	41.6	41.6	dolostone	*Acritarch (?)*	142.3_2.7	Z42(center)	Label to left	In-situ	yes
S-41.6_3	41.6	41.6	dolostone	*Leiosphaeridia sp.*	133.7_7.2	V33_2	Label to left	In-situ	yes
S-41.6_3	41.6	41.6	dolostone	*Leiosphaeridia sp.*	145.4_9.8	S45_2	Label to left	In-situ	yes
S-41.6_3	41.6	41.6	dolostone	*Leiosphaeridia sp.*	151_16.3	L51_3	Label to left	In-situ	yes

S-41.6_3	41.6	41.6	dolostone	*Leiosphaeridia sp.*	136.4_15.5	M36_4	Label to left	In-situ	yes
S-41.6_3	41.6	41.6	dolostone	*Leiosphaeridia sp.*	135.6_18.3	K35_2	Label to left	In-situ	yes
S-41.6_3	41.6	41.6	dolostone	*Leiosphaeridia sp.*	136.7_19.7	J36_4	Label to left	In-situ	yes
S-41.6_3	41.6	41.6	dolostone	*Leiosphaeridia sp.*	140_21.3	F40_3	Label to left	In-situ	yes
S-41.6_3	41.6	41.6	dolostone	*Leiosphaeridia sp.*	133.7_7.2	V33_2	Label to left	In-situ	yes
S-41.75_1	41.75	41.75	dolostone					In-situ	no
S-41.75_2	41.75	41.75	dolostone					In-situ	no
S-41.85	41.85	41.85	dolostone					In-situ	no
S41.9_1	41.9	41.9	dolostone					In-situ	no
S41.9_2	41.9	41.9	dolostone					In-situ	no
13SDP_DST2_30	40.5	42.4	dolostone						no
13SDP_DST2_31	40.7	42.6	dolostone					In-situ	no
13SDP_DST2_32	41.1	43	dolostone	*Leiosphaeridia sp.*	123.2_7.6	U23_3	Label to left	In-situ	yes
13SDP_DST2_32	41.1	43	dolostone	*Leiosphaeridia sp.*	119.1_10.9	R19_3	Label to left	In-situ	yes
13SDP_DST2_32	41.1	43	dolostone	*Leiosphaeridia sp.*	111.5_13.2	P11_2	Label to left	In-situ	yes
13SDP_DST2_32	41.1	43	dolostone	*Leiosphaeridia sp.*	111_13.7	O11_3	Label to left	In-situ	yes
13SDP_DST2_32	41.1	43	dolostone	*Leiosphaeridia sp.*	120_16.5	M20_1	Label to left	In-situ	yes
13SDP_DST2_32	41.1	43	dolostone	*M. minima*	128.5_9.6	S28_4	Label to left	In-situ	yes
13SDP_DST2_32	41.1	43	dolostone	*M. minima*	123.1_10.2	S23_1	Label to left	In-situ	yes
13SDP_DST2_32	41.1	43	dolostone	*Siphonophycus kestron (?)*	136.6_8.4	T36_4	Label to left	In-situ	yes
13SDP_DST2_32	41.1	43	dolostone	*Siphonophycus robustum*	137_8.5	T37_3	Label to left	In-situ	yes
13SDP_DST2_32	41.1	43	dolostone	*Siphonophycus robustum*	137.6_8.9	T37_2	Label to left	In-situ	yes
13SDP_DST2_32	41.1	43	dolostone	*Siphonophycus robustum*	137.5_9	T37_2	Label to left	In-situ	yes
13SDP_DST2_33a	41.1	43.3	dolostone	*Siphonophycus robustum*	138.3_15.6	M38_4	Label to left	In-situ	yes
13SDP_DST2_33a	41.1	43.3	dolostone	*Siphonophycus robustum*	142.3_8.3	T42_4	Label to left	In-situ	yes
13SDP_DST2_33a	41.1	43.3	dolostone	*Siphonophycus robustum*	139.1_7.4	U39_3	Label to left	In-situ	yes
13SDP_DST2_33a	41.1	43.3	dolostone	*Siphonophycus robustum*	138.3_8.5	T38_4	Label to left	In-situ	yes
13SDP_DST2_33a	41.1	43.3	dolostone	*Siphonophycus robustum*	139_9.5	S39_3	Label to left	In-situ	yes
13SDP_DST2_33a	41.1	43.3	dolostone	*Siphonophycus robustum*	139.2_9.8	S39(center)	Label to left	In-situ	yes
13SDP_DST2_33a	41.1	43.3	dolostone	*Siphonophycus robustum*	138.3_9.9, difficult to see below 40x	S38_2	Label to left	In-situ	yes
13SDP_DST2_33a	41.1	43.3	dolostone	*Siphonophycus robustum*	142.7_8.9 (difficult to see below 40x)	T42_2	Label to left	In-situ	yes
13SDP_DST2_33a	41.1	43.3	dolostone	*Siphonophycus robustum*	138.9_10.4	R39_3	Label to left	In-situ	yes
13SDP_DST2_33a	41.1	43.3	dolostone	*Siphonophycus robustum*	142.6_10.2	S42_2	Label to left	In-situ	yes
13SDP_DST2_33a	41.1	43.3	dolostone	*Siphonophycus robustum*	138.1_11.9, difficult to see below 40x	Q38_1	Label to left	In-situ	yes
13SDP_DST2_33a	41.1	43.3	dolostone	*Siphonophycus robustum*	138.4_11.9, difficult to see below 40x	Q38_2	Label to left	In-situ	yes
13SDP_DST2_33a	41.1	43.3	dolostone	*Siphonophycus robustum*	138.7_12	Q38_2	Label to left	In-situ	yes
13SDP_DST2_33a	41.1	43.3	dolostone	*Siphonophycus robustum*	138.8_12.2	Q39_1	Label to left	In-situ	yes
13SDP_DST2_33a	41.1	43.3	dolostone	*Siphonophycus robustum*	138.9_14	O39_1	Label to left	In-situ	yes
13SDP_DST2_33a	41.1	43.3	dolostone	*Siphonophycus robustum*	139.2_14.8	N39_1	Label to left	In-situ	yes
S-44.65	44.65	44.65	dolostone					In-situ	no
S-44.7	44.7	44.7	dolostone						no

S-44.75	44.75	44.75	dolostone					In-situ	no
S-45.8	45.8	45.8	dolostone					In-situ	no
13SDP_DST2_34	52.5	55	dolostone						no
S-57.2	57.2	57.2	dolostone					Uncertain (insufficient features)	no
S-57.3	57.3	57.3	dolostone					Uncertain (insufficient features)	no
S-57.5	57.5	57.5	dolostone					Uncertain (insufficient features)	no
S-57.6	57.6	57.6	dolostone					Uncertain (insufficient features)	no
S-57.65	57.65	57.65	dolostone					Uncertain (insufficient features)	no
S-59.3	59.3	59.3	olistostrome breccia					In-situ	no
13SDP_DST2_35	56.8	59.4	olistostrome breccia					In-situ	no
S-59.6_1	59.6	59.6	olistostrome breccia					Uncertain (insufficient features)	no
S-59.6_2	59.6	59.6	olistostrome breccia					Uncertain (insufficient features)	no
S-59.6_3	59.6	59.6	olistostrome breccia					Uncertain (insufficient features)	no
13SDP_DST2_36	57.4	60.4	olistostrome breccia					Uncertain (insufficient features)	no
13SDP_DST2_37	63.5	66.8	dolostone					Uncertain (insufficient features)	no
13SDP_DST2_38	67	70.5	dolostone						no
S-76.4_4_1	76.4	76.4	dolostone					Reworked	no
S-76.4_4_2	76.4	76.4	dolostone	*Mengeosphaera minima (?)*	135_18.7	J35_3	Label to left	Reworked	yes
S-76.4_4_2	76.4	76.4	dolostone	*Leiosphaeridia sp.*	136_19	J36_1	Label to left	Reworked	yes
S-76.4_4_2	76.4	76.4	dolostone	*Appendisphaera hemisphaerica*	134.1_19	J34_1	Label to left	Reworked	yes
S-76.4_4_2	76.4	76.4	dolostone	*Leiosphaeridia sp.*	135.9_18.7	J36_3	Label to left	Reworked	yes
S-76.4_4_2	76.4	76.4	dolostone	*Appendisphaera crebra*	138.4_17.2	L38_2	Label to left	Reworked	yes
S-76.4_4_2	76.4	76.4	dolostone	*Leiosphaeridia sp.*	138.7_17.3	K38_4	Label to left	Reworked	yes
S-76.4_4_2	76.4	76.4	dolostone	*Appendisphaera hemisphaerica*	137.5_17.3	K37_4	Label to left	Reworked	yes
S-76.4_4_2	76.4	76.4	dolostone	*Leiosphaeridia sp.*	138.3_17.4	K38_3	Label to left	Reworked	yes
S-76.4_4_2	76.4	76.4	dolostone	*Leiosphaeridia sp.*	138.5_17.4	K38_4	Label to left	Reworked	yes
S-76.4_4_2	76.4	76.4	dolostone	*Leiosphaeridia sp.*	139_17.3	K39_3	Label to left	Reworked	yes
S-76.4_4_2	76.4	76.4	dolostone	*Leiosphaeridia sp.*	139_17.5	K39_3	Label to left	Reworked	yes
S-76.4_4_2	76.4	76.4	dolostone	*Leiosphaeridia sp.*	138_17.5	K38_3	Label to left	Reworked	yes
S-76.4_4_2	76.4	76.4	dolostone	*Leiosphaeridia sp.*	137.9_17.6	K38_3	Label to left	Reworked	yes
S-76.4_4_2	76.4	76.4	dolostone	*Mengeosphaera minima*	136.6_18	K36_2	Label to left	Reworked	yes
S-76.4_4_2	76.4	76.4	dolostone	*Leiosphaeridia sp.*	135.6_18.5	J35_4	Label to left	Reworked	yes
S-76.4_4_2	76.4	76.4	dolostone	*Appendisphaera hemisphaerica*	137.7_17.8	K37_2	Label to left	Reworked	yes
S-76.4_4_2	76.4	76.4	dolostone	*Leiosphaeridia sp.*	135.8_19	J35_2	Label to left	Reworked	yes
S-76.4_4_2	76.4	76.4	dolostone	*Leiosphaeridia sp.*	135.9_18.8	J36_1	Label to left	Reworked	yes
S-76.4_4_2	76.4	76.4	dolostone	*Leiosphaeridia sp.*	136_18.7	J36_3	Label to left	Reworked	yes
S-76.4_4_2	76.4	76.4	dolostone	*Leiosphaeridia sp.*	136_18.7	J36_3	Label to left	Reworked	yes
S-76.4_4_2	76.4	76.4	dolostone	*Leiosphaeridia sp.*	165_5.3	W65_3	Label to left	Reworked	yes
S-76.4_4_2	76.4	76.4	dolostone	*Leiosphaeridia sp.*	164.5_19.3	H64_4	Label to left	Reworked	yes

13SDP_DST2_39	72.7	76.5	dolostone					In-situ	no
S-81.9	81.9	81.9	dolostone					In-situ	no
S-82.2	82.2	82.2	dolostone					In-situ	no
13SDP_DST2_40	74	82.5	dolostone	*Siphonophycus robustum*	139.2_15 difficult to see below 40x	N39_1	Label to left	In-situ	yes
S-83.3	83.3	83.3	dolostone					In-situ	no
13SDP_DST2_41	76.5	85.3	dolostone					In-situ	no
13SDP_DST2_41a	76.5	85.4	dolostone					In-situ	no
13SDP_DST2_42	79	88.1	dolostone					In-situ	no
13SDP_DST2_43	80	89.2	olistostrome breccia	*Ericiasphaera sp.*	135.5_23.3	E35_2	Label to left	Reworked	yes
13SDP_DST2_43	80	89.2	olistostrome breccia	*Asterocapsoides sinensis*	114.6_11.6	R14_2	Label to left	Reworked	yes
13SDP_DST2_43	80	89.2	olistostrome breccia	*Urasphaera nupta*	135.7_23.5	D35_4	Label to left	Reworked	yes
S-90.2	90.2	90.2	shaley dolostone					In-situ	no
13SDP_DST2_44	81.5	90.9	dolostone						no
S-94.8	94.8	94.8	shaley dolostone					In-situ	no
13SDP_DST2_45	85	94.8	shaley dolostone						no
S-98.5	98.5	98.5	shaley dolostone						no
S-106.6	106.6	106.6	shaley dolostone					In-situ	no
S-108.6	108.6	108.6	shaley dolostone						no
S-130.2	130.2	130.2	shaley dolostone					Reworked	no
S-170	170	170	bedded chert					In-situ	no
S-170.01	170.01	170.01	bedded chert					In-situ	no
S-170.02	170.02	170.02	bedded chert					In-situ	no
S-170.03	170.03	170.03	bedded chert					In-situ	no
S-170.05	170.05	170.05	bedded chert					In-situ	no
S-170.06	170.06	170.06	bedded chert					In-situ	no
S-170.07	170.07	170.07	bedded chert					In-situ	no
S-170.08	170.08	170.08	bedded chert					In-situ	no
S-172	172	172	bedded chert					In-situ	no
S-174.4	174.4	174.4	bedded chert					In-situ	no
S-174.5	174.5	174.5	bedded chert					In-situ	no
S-175	175	175	bedded chert					In-situ	no
S-175.6	175.6	175.6	bedded chert					In-situ	no
S-176	176	176	bedded chert					In-situ	no
S-176.4	176.4	176.4	bedded chert					In-situ	no
S-177.3	177.3	177.3	bedded chert					In-situ	no
S-177.8_1	177.8	177.8	bedded chert					In-situ	no
S-177.8_2	177.8	177.8	bedded chert					In-situ	no
S-178.1	178.1	178.1	bedded chert					In-situ	no
S-178.6	178.6	178.6	bedded chert					In-situ	no
S-178.7	178.7	178.7	bedded chert					In-situ	no
S-179.7	179.7	179.7	bedded chert					In-situ	no

S-180	180	180	bedded chert					In-situ	no
S-181	181	181	bedded chert					In-situ	no
S-181.2	181.2	181.2	bedded chert					In-situ	no
S-181.5	181.5	181.5	bedded chert					In-situ	no
S-182	182	182	bedded chert					In-situ	no
S-182.3	182.3	182.3	bedded chert					In-situ	no
S-182.6	182.6	182.6	bedded chert					In-situ	no
S-183.6	183.6	183.6	bedded chert					In-situ	no
S-184	184	184	bedded chert					In-situ	no
S-185.2	185.2	185.2	bedded chert					In-situ	no
S-185.7	185.7	185.7	bedded chert					In-situ	no
S-187.5	187.5	187.5	bedded chert					In-situ	no
S-187.7	187.7	187.7	bedded chert					In-situ	no
S-188.5	188.5	188.5	bedded chert					In-situ	no
S-188.7	188.7	188.7	bedded chert					In-situ	no
S-190	190	190	bedded chert					In-situ	no
S-190.5	190.5	190.5	bedded chert					In-situ	no
S-192	192	192	bedded chert					In-situ	no
S192.4	192.4	192.4	bedded chert					In-situ	no
13_WZS_DST2_2A	1.2	86.2	black shale					In-situ	no
13_WZS_DST2_2B	1.2	86.2	black shale					In-situ	no
13_WZS_DST2_2C	1.2	86.2	black shale					In-situ	no
13_WZS_DST2_2D	1.2	86.2	black shale					In-situ	no
13_WZS_DST2_2E	1.2	86.2	black shale					In-situ	no
13_WZS_DST2_2F	1.2	86.2	black shale					In-situ	no
13_WZS_DST2_3A	0.66	85.66	black shale					In-situ	no
13_WZS_DST2_3B	0.66	85.66	black shale					In-situ	no
13_WZS_DST2_3C	0.66	85.66	black shale					In-situ	no
13_WZS_DST2_3D	0.66	85.66	black shale					In-situ	no
13_WZS_DST2_3E	0.66	85.66	black shale					In-situ	no
13_WZS_DST2_3F	0.66	85.66	black shale					In-situ	no
13_WZS_DST2_3G	0.66	85.66	black shale					In-situ	no
13_WZS_DST2_3H	0.66	85.66	black shale					In-situ	no
13_WZS_DST2_3I	0.66	85.66	black shale					In-situ	no
13_WZS_DST2_3J	0.66	85.66	black shale					In-situ	no
13_WZS_DST2_3K	0.66	85.66	black shale					In-situ	no
13_WZS_DST2_3L	0.66	85.66	black shale					In-situ	no
13_WZS_DST2_4A	20.05	100.05	black shale					In-situ	no
13_WZS_DST2_4B	20.05	100.05	black shale					In-situ	no
13_WZS_DST2_4C	20.05	100.05	black shale					In-situ	no

13_WZS_DST2_5A	20.5	100.5	black shale					In-situ	no
13_WZS_DST2_5B	20.5	100.5	black shale					In-situ	no
13_WZS_DST2_5C	20.5	100.5	black shale	*Paratetraphycus giganteum*	114_20.5	H14_2	Label to left	In-situ	yes
13_WZS_DST2_5C	20.5	100.5	black shale	*Siphonophycus robustum*	16.2_19.7	H16_1	Label to left	In-situ	yes
13_WZS_DST2_5C	20.5	100.5	black shale	*Siphonophycus kestron*	114.7_20	H14_4	Label to left	In-situ	yes
13_WZS_DST2_5C	20.5	100.5	black shale	*Siphonophycus robustum*	115.5_18.8	J15_4	Label to left	In-situ	yes
13_WZS_DST2_5C	20.5	100.5	black shale	*Siphonophycus robustum*	116_18.9	J16_3	Label to left	In-situ	yes
13_WZS_DST2_5C	20.5	100.5	black shale	*Siphonophycus robustum*	114.7_18.1	K14_2	Label to left	In-situ	yes
13_WZS_DST2_5C	20.5	100.5	black shale	*Siphonophycus robustum*	115.4_19.5	J15_2	Label to left	In-situ	yes
13_WZS_DST2_5C	20.5	100.5	black shale	*Siphonophycus kestron*	114_19.6	H14_3	Label to left	In-situ	yes
13_WZS_DST2_5C	20.5	100.5	black shale	*Siphonophycus robustum*	115.5_19	J15_4	Label to left	In-situ	yes
13_WZS_DST2_5C	20.5	100.5	black shale	*Siphonophycus robustum*	15.9_19.2	J16_1	Label to left	In-situ	yes
13_WZS_DST2_5C	20.5	100.5	black shale	*Siphonophycus robustum*	115.7_19.6	H15_4	Label to left	In-situ	yes
13_WZS_DST2_5C	20.5	100.5	black shale	*Siphonophycus robustum*	114.3_19	J14(center)	Label to left	In-situ	yes
13_WZS_DST2_5C	20.5	100.5	black shale	*Siphonophycus robustum*	115.9_19	J16_3	Label to left	In-situ	yes
13_WZS_DST2_5C	20.5	100.5	black shale	*Siphonophycus robustum*	114.9_20.2	H15_1	Label to left	In-situ	yes
13_WZS_DST2_5C	20.5	100.5	black shale	*Siphonophycus robustum*	116_20.3	H16_1	Label to left	In-situ	yes
13_WZS_DST2_5C	20.5	100.5	black shale	*Siphonophycus robustum*	115.4_20.3	H15_2	Label to left	In-situ	yes
13_WZS_DST2_5C	20.5	100.5	black shale	*Siphonophycus robustum*	115.5_21	G15_4	Label to left	In-situ	yes
13_WZS_DST2_5C	20.5	100.5	black shale	*Siphonophycus robustum*	115.9_19.9	H16_3	Label to left	In-situ	yes
13_WZS_DST2_5C	20.5	100.5	black shale	*Siphonophycus robustum*	115.4_21.6	F15_4	Label to left	In-situ	yes
13_WZS_DST2_5C	20.5	100.5	black shale	*Siphonophycus robustum*	115.4_21.6	F15_4	Label to left	In-situ	yes
13_WZS_DST2_5C	20.5	100.5	black shale	*Siphonophycus robustum*	115.8_19	J16_3	Label to left	In-situ	yes
13_WZS_DST2_5C	20.5	100.5	black shale	*Siphonophycus robustum*	115.9_18.9	J16_3	Label to left	In-situ	yes
13_WZS_DST2_5C	20.5	100.5	black shale	*Siphonophycus kestron*	113.7_20.2	H13_2	Label to left	In-situ	yes
13_WZS_DST2_5C	20.5	100.5	black shale	Unidentified Acritarch	116.1_18.8	J16_3	Label to left	In-situ	yes
13_WZS_DST2_5C	20.5	100.5	black shale	*Siphonophycus robustum*	115.3_20.7	J15_4	Label to left	In-situ	yes
13_WZS_DST2_5C	20.5	100.5	black shale	*Siphonophycus robustum*	114.3_21.4	G14_1	Label to left	In-situ	yes
13_WZS_DST2_5C	20.5	100.5	black shale	*Siphonophycus robustum*	114.3_22.3	F14_3	Label to left	In-situ	yes
13_WZS_DST2_5C	20.5	100.5	black shale	*Tianzushania spinosa*	110.3_19.8	H10_1	Label to left	In-situ	
13_WZS_DST2_FloatA			black shale					In-situ	no
13_WZS_DST2_FloatB			black shale					In-situ	no
13_WZS_DST2_FloatC			black shale					In-situ	no
13_HJP_DST2_1	0	0	dolostone					In-situ	no
13_HJP_DST2_2	10	10	dolostone					In-situ	no
13_HJP_DST2_3A	10	10	dolostone					In-situ	no
13_HJP_DST2_3B	10	10	dolostone					In-situ	no
13_HJP_DST2_4A	10	10	dolostone					In-situ	no
13_HJP_DST2_4B	10	10	dolostone					In-situ	no
13_HJP_DST2_4C	10	10	dolostone					In-situ	no
13_HJP_DST2_5A	20	20	dolostone	*Siphonophycus robustum*	130.5_15.3	N30_2	Label to right	In-situ	yes

13_HJP_DST2_5A	20	20	dolostone	*Siphonophycus robustum*	131.5_15.8	M31_4	Label to right	In-situ	yes
13_HJP_DST2_5A	20	20	dolostone	*Tianzushania spinosa*	132.6_18.4	K32_2	Label to right	In-situ	yes
13_HJP_DST2_5B	20	20	dolostone	*Siphonophycus typicum*	114.8_10.1	S15_1	Label to right	In-situ	yes
13_HJP_DST2_5B	20	20	dolostone	*Siphonophycus robustum*	117.8_13.9	O18_3	Label to right	In-situ	yes
13_HJP_DST2_5B	20	20	dolostone	*Siphonophycus robustum*	114.8_17.7	K15_3	Label to right	In-situ	yes
13_HJP_DST2_5B	20	20	dolostone	*Salome sp.*	118.6_17.9	K18_4	Label to right	In-situ	yes
13_HJP_DST2_5C	20	20	dolostone	*Paratetraphycus giganteum*	113.9_9.7	S14_3	Label to right	In-situ	yes
13_HJP_DST2_5C	20	20	dolostone	*Siphonophycus robustum*	108.9_11.9	Q9_3	Label to right	In-situ	yes
13_HJP_DST2_6A	36	36	dolostone					In-situ	no
13_HJP_DST2_6B	36	36	dolostone					In-situ	no
13_HJP_DST2_6C	36	36	dolostone					In-situ	no
13_HJP_DST2_7A	~below sample 5	~below sample 5	dolostone					In-situ	no
13_HJP_DST2_7B	~below sample 5	~below sample 5	dolostone					In-situ	no
13_HJP_DST2_7C	~below sample 5	~below sample 5	dolostone					In-situ	no
13_HJP_DST2_F1			dolostone					In-situ	no
13_HJP_DST2_F1B			dolostone					In-situ	no
13_HJP_DST2_F1C			dolostone					In-situ	no
13_HJP_DST2_F2A			dolostone					In-situ	no
13_HJP_DST2_F2B			dolostone					In-situ	no
13_HJP_DST2_F2C			dolostone					In-situ	no
13_HJP_DST2_F4A			dolostone					In-situ	no

Appendix D. $\delta^{13}C_{carb}$ data from the Wangzishi section of the Doushantuo Formation

Sample Number	$\delta^{13}C_{pdb}$	$\delta^{18}O_{pdb}$	Measured Stratigraphic Height (m)	Corrected Stratigraphic Height(m)
11-WZS-DST3-43	4.338	-1.88	43	87
11-WZS-DST3-41	5.064	-2.273	41	85
11-WZS-DST3-40	5.015	-2.129	40	84
11-WZS-DST3-38(2)	2.561	-6.279	38	82
11-WZS-DST3-38(1)	4.803	-9.351	38	82
11-WZS-DST3-36	3.739	-9.571	36	80
11-WZS-DST3-34	4.929	-8.806	34	78
11-WZS-DST3-31.8	6.139	-7.938	31.8	75.8
11-WZS-DST3-31	6.896	-7.307	31	75
11-WZS-DST3-30	6.848	-7.501	30	74
11-WZS-DST3-29	6.315	-9.362	29	73
11-WZS-DST3-28	6.876	-8.803	28	72
11-WZS-DST3-27	6.283	-9.485	27	71
11-WZS-DST3-26	7.13	-8.219	26	70
11-WZS-DST3-25	7.24	-8.609	25	69
11-WZS-DST3-24.4	5.459	-9.164	24.4	68.4
11-WZS-DST3-23	0.123	-10.056	23	67
11-WZS-DST3-22	7.019	-6.268	22	66
11-WZS-DST3-21	6.831	-6.512	21	65
11-WZS-DST3-20	6.071	-4.747	20	64

11-WZS-DST3-19	6.716	-2.667	19	63
11-WZS-DST3-18.3	6.505	-2.722	18.3	62.3
11-WZS-DST3-17	4.765	-3.275	17	61
11-WZS-DST3-16	7.088	-7.907	16	60
11-WZS-DST3-15	7.492	-8.197	15	59
11-WZS-DST3-14	6.678	-7.191	14	58
11-WZS-DST3-13	7.66	-5.927	13	57
11-WZS-DST3-12	7.967	-5.287	12	56
11-WZS-DST3-11	7.844	-5.53	11	55
11-WZS-DST3-10	7.095	-6.376	10	54
11-WZS-DST3-9	6.453	-6.837	9	53
11-WZS-DST3-8	7.082	-7.907	8	52
11-WZS-DST3-7.3	7.758	-6.769	7.3	51.3
11-WZS-DST3-7	7.395	-7.076	7	51
11-WZS-DST3-5.7	7.628	-8.342	5.7	49.7
11-WZS-DST3-5	7.633	-7.73	5	49